

**A NUMERICAL STUDY ON
THE DYNAMIC BEHAVIOUR OF GRAVITY AND CANTILEVER
RETAINING WALLS WITH GRANULAR BACKFILL**

**A THESIS SUBMITTED TO
THE GRADUATE SCHOOL OF NATURAL AND APPLIED SCIENCES
OF
MIDDLE EAST TECHNICAL UNIVERSITY**

BY

ERSAN YILDIZ

**IN PARTIAL FULFILLMENT OF THE REQUIREMENTS
FOR
THE DEGREE OF DOCTOR OF PHILOSOPHY
IN
CIVIL ENGINEERING**

FEBRUARY 2007

Approval of the Graduate School of Natural and Applied Sciences

Prof. Dr. Canan Özgen
Director

I certify that this thesis satisfies all the requirements as a thesis for the degree of Doctor of Philosophy.

Prof. Dr. Güney Özcebe
Head of Department

This is to certify that we have read this thesis and that in our opinion it is fully adequate, in scope and quality, as a thesis for the degree of Doctor of Philosophy.

Prof. Dr. M. Yener Özkan
Supervisor

Examining Committee Members

Prof. Dr. Altay Birand (METU, CE) _____

Prof. Dr. M. Yener Özkan (METU, CE) _____

Prof. Dr. Celal Karpuz (METU, MINE) _____

Prof. Dr. Tekin Gültop (Gazi U., CE) _____

Assoc. Prof. Dr. K. Önder Çetin (METU, CE) _____

I hereby declare that all information in this document has been obtained and presented in accordance with academic rules and ethical conduct. I also declare that, as required by these rules and conduct, I have fully cited and referenced all material and results that are not original to this work.

Name, Last name : ERSAN YILDIZ

Signature :

ABSTRACT

A NUMERICAL STUDY ON THE DYNAMIC BEHAVIOUR OF GRAVITY AND CANTILEVER RETAINING WALLS WITH GRANULAR BACKFILL

Yıldız, Ersan

Ph.D., Department of Civil Engineering

Supervisor : Prof. Dr. M. Yener Özkan

February 2007, 160 pages

Dynamic behaviour of gravity and cantilever retaining walls is investigated by finite element method, incorporating the nonlinear elasto-plastic material properties of soil and separation of the wall and backfill. Two dimensional finite element models are developed employing the finite element software ANSYS. The wall is modelled to rest on a soil layer allowing translational and rotational movements of the wall. Soil-wall systems are subjected to harmonic and real earthquake motions with different magnitude and frequency characteristics at the base. The maximum lateral force and its application point during dynamic loading are determined for each case. It is observed that the frequency content of the base motion has a significant influence on the dynamic lateral soil pressures and the lateral forces considerably increase as the base motion frequency approaches the fundamental frequency of the soil layer. The maximum lateral thrusts calculated by finite element analyses are generally found to be greater than those suggested by Mononobe-Okabe method and experimental findings. Nevertheless, the locations of the application point obtained by finite element method are found to be in good agreement with the results of experimental studies.

Keywords : Seismic earth pressure, Retaining wall, Finite element method

ÖZ

GRANÜLER DOLGULU AĞIRLIK VE ANKASTRE İSTİNAT DUVARLARININ DİNAMİK DAVRANIŞI ÜZERİNE NÜMERİK BİR ÇALIŞMA

Yıldız, Ersan

Doktora, İnşaat Mühendisliği Bölümü

Tez Yöneticisi : Prof. Dr. M. Yener Özkan

Şubat 2007, 160 sayfa

Ağırlık ve ankastre istinat duvarlarının dinamik davranışı sonlu elemanlar metodu kullanılarak incelenmiştir. Analizlerde zemin elasto-plastik malzeme olarak modellenmiş, dinamik hareket sırasında duvar ile zeminin birbirinden ayrılması gözönüne alınmıştır. Analizler ANSYS programı kullanılarak oluşturulan iki boyutlu sonlu elemanlar modelleri ile yapılmıştır. Duvar, bir temel zemini tabakası üzerinde yeralacak şekilde modellenerek, yanal ötelenme ve dönme hareketlerini yapabilmesi sağlanmıştır. Oluşturulan zemin-duvar sistemleri tabanlarına değişik büyüklük ve frekans özelliklerinde harmonik hareketler ve gerçek deprem hareketleri uygulanmıştır. Dinamik yükleme sırasında oluşan maksimum yanal kuvvet ve tatbik noktası incelenen her durum için belirlenmiştir. Taban hareketi frekans içeriğinin yanal toprak basınçları üzerinde önemli etkisinin olduğu gözlenmiştir. Nümerik analizler ile elde edilen maksimum yanal kuvvet sonuçları, genellikle Mononobe-Okabe metodu ve deneysel çalışmalardan elde edilen sonuçlardan yüksek çıkmaktadır. Diğer yandan, tatbik noktası lokasyonlarının, ağırlık ve ankastre duvarlar için yapılan deneysel sonuçlarla uyumlu olduğu görülmüştür.

Anahtar Kelimeler : Sismik toprak basıncı, İstinat duvarı, Sonlu elemanlar metodu

To My Family

ACKNOWLEDGMENTS

The author wishes to express his deepest gratitude to his supervisor Prof. Dr. M. Yener Özkan for his support, trust and encouragement throughout the research. The author would also like to thank Assoc. Prof. Dr. K. Önder Çetin for his valuable support and suggestions.

The author deeply appreciates the support received from Mr. Ali Anıl Yunatçı and Mr. Özgür Lütü Ertuğrul during the study.

TABLE OF CONTENTS

PLAGIARISM	iii
ABSTRACT	iv
ÖZ	v
DEDICATION	vi
ACKNOWLEDGMENTS	vii
TABLE OF CONTENTS	viii

CHAPTER

1. INTRODUCTION	1
2. LITERATURE REVIEW ON DYNAMIC RESPONSE OF RETAINING WALLS	3
2.1 Limit-Equilibrium methods	3
2.1.1 Mononobe-Okabe method	3
2.1.2 Other studies	5
2.2 Analytical or numerical methods based on linear elastic or elasto-plastic theory	8
2.2.1 Wood (1973) solution	8
2.2.2 Steedman and Zeng (1990) solution	10
2.2.3 Other studies	12
2.3 Experimental studies	29
3. REVIEW ON THEORETICAL ASPECTS	41
3.1 Material model	41
3.1.1 Review on plasticity	41
3.1.2 Drucker-Prager material model	47
3.2 Dynamic finite element analysis	52
3.2.1 Review on time history analysis	52
3.2.2 Damping	57

3.2.3 Absorbing boundaries	58
3.2.4 Verification by 1-D wave propagation problem	59
3.2.5 About contact model	61
3.3 Linear quadrilateral plane-strain element.....	65
4. FINITE ELEMENT ANALYSES FOR 8 METER HIGH WALL RESTING ON ELASTIC FOUNDATION SOIL	69
4.1 Gravity wall	69
4.1.1 The model and the parameters	69
4.1.2 The results and comparisons	75
4.2 Cantilever wall	89
4.2.1 The model and the parameters	89
4.2.2 The results and comparisons	93
4.3 Analyses with real earthquake records	104
5. FINITE ELEMENT ANALYSES FOR 5 METER HIGH WALL RESTING ON ELASTO-PLASTIC FOUNDATION SOIL.....	113
5.1 Gravity wall	114
5.1.1 The model and the parameters	114
5.1.2 The results and comparisons	115
5.2 Cantilever wall	123
5.2.1 The model and the parameters	123
5.2.2 The results and comparisons	125
5.3 Analyses with real earthquake records	131
5.4 On the effect of wall mass	139
6. COMPARISON WITH EXPERIMENTAL STUDIES	145
6.1 Gravity wall	145
6.2 Cantilever wall	148
7. CONCLUSIONS	150
REFERENCES	154
CURRICULUM VITAE	160

CHAPTER 1

INTRODUCTION

Many types of earth retaining structures are in seismically active areas which make it necessary to consider the potential earthquake induced forces that will act on these structures in the design.

The objective of this study is to investigate the dynamic behaviour of gravity and cantilever retaining walls which are commonly used in practice.

Many theoretical and experimental studies about the dynamic response of gravity and cantilever walls have been carried out over the years and several methods have been proposed for the calculation of the earthquake-induced earth pressures and deformations. A review on these studies including limit-equilibrium methods, analytical or numerical solutions and experimental researches are presented in Chapter 2.

The dynamic response of a soil-retaining wall system is quite complicated and dependent on many factors such as the geometry and type of the wall, soil conditions and earthquake motions. It is currently not possible to consider all aspects of the dynamic behaviour of retaining walls so that various simplifications about the soil, structure and input motions are made in the design methods (Kramer, 1996).

Finite element method is one of the most commonly used methods for static and dynamic soil mechanics and soil-structure interaction problems in which the soil is represented as a continuum consisting of discrete elements. A two dimensional

finite element model is developed for the analyses of soil-retaining wall systems in this study. Analyses are made by the finite element program ANSYS. The nonlinear stress-strain properties of the soil and the relative deformations (sliding with friction and gap) between the wall and soil are taken into account. The details about the finite element model regarding the dynamic solution technique (time history analysis), material properties, contact between the wall and soil and boundary conditions are given in Chapter 3.

The proposed models for gravity and cantilever retaining walls are subjected to harmonic and real earthquake motions at the base. The effect of magnitude and frequency content of the base motions on the dynamic response of the wall is investigated by using base motions with different characteristics in the analyses. The deformation modes of the wall and the variation of the dynamic lateral pressures on the wall with time are studied in detail.

Maximum total lateral force and its point of application are calculated for each case. The results are compared with the conventional solution methods and experimental findings.

Finite element analyses and the obtained results are presented in Chapters 4 and 5 for walls of different height. The results are compared with the common solution methods in these chapters.

Comparison of the results obtained by finite element analyses with the experimental findings is given in Chapter 6.

CHAPTER 2

LITERATURE REVIEW ON DYNAMIC RESPONSE OF RETAINING WALLS

A review of the solution methods and studies about the seismic lateral pressures acting on rigid and cantilever retaining walls is given in this chapter.

Several approaches have been developed to solve the dynamic earth pressure problems. They can be classified into 3 groups stated below:

- Limit-equilibrium methods
- Analytical and numerical methods based on linear elastic or elasto-plastic theory
- Experimental studies (shake table tests, centrifuge tests and measurements on existing structures)

The most common methods used in design relevant to the present study presented in detail are Mononobe-Okabe, Steedman and Zeng (1990) and Wood (1973) solutions. Other studies are stated briefly.

2.1 Limit-Equilibrium methods

2.1.1 Mononobe-Okabe method

The earliest and one of the most frequently used methods in design for estimating the seismic lateral pressures on retaining walls is that developed by Mononobe (1929) and Okabe (1926) known as Mononobe-Okabe (M-O) method. It is

extension of Coulomb's earth pressure theory considering the dynamic forces as additional static forces acting on the trial Coulomb wedge. The method is applicable to dry cohesionless backfill. The basic assumptions of the analysis method are summarized by Nazarian and Hadjian (1979) as:

- There is sufficient wall displacement producing a state of static equilibrium behind the wall, resulting in minimum active pressure.
- The maximum shear strength of soil is mobilized along the failure plane when the minimum active pressure is attained.
- The wedge acts as a rigid body that the vertical and horizontal accelerations are uniform and have the same magnitudes as the base of the wall.
- The inertial effects of the retaining structure are neglected.
- The lateral force acts at a distance of $H/3$ above the base, H showing the height of the wall.

The forces considered in the analysis, in the presence of pseudo-static accelerations in the horizontal and vertical directions, $a_h = k_h g$ and $a_v = k_v g$ are shown in Figure 2.1.1.1. The total seismic active thrust on the wall is calculated from the force equilibrium of the wedge and can be expressed as:

$$P_{AE} = \frac{1}{2} K_{AE} \gamma H^2 (1 - k_v) \quad (2.1.1.1)$$

where the dynamic active earth pressure coefficient K_{AE} is given as:

$$K_{AE} = \frac{\cos^2(\phi - \theta - \psi)}{\cos(\varphi) \cos^2(\theta) \cos(\delta + \theta + \psi) \left[1 + \sqrt{\frac{\sin(\delta + \phi) \sin(\phi - \beta - \psi)}{\cos(\delta + \theta + \psi) \cos(\beta - \theta)}} \right]^2} \quad (2.1.1.2)$$

where $\psi = \tan^{-1} [k_h / (1 - k_v)]$; ϕ = angle of friction of backfill; δ = angle of friction between the backfill and the wall.

A detailed review of M-O method was made by Seed and Whitman (1970). For vertical walls retaining horizontal dry backfills, they suggested to express the total seismic lateral force as the sum of the initial static pressure and the dynamic pressure increment ΔP_{AE} as:

$$P_{AE} = \text{Static pressure} + \Delta P_{AE} = \frac{1}{2} K_A \gamma H^2 + \Delta P_{AE} \quad (2.1.1.3)$$

It is suggested to assume that the static and incremental dynamic components act $H/3$ and $0.6H$ above the base respectively. Also it is shown that the effect of friction angle between the wall and backfill and the vertical acceleration on seismic lateral pressures are insignificant especially for higher levels of horizontal acceleration.

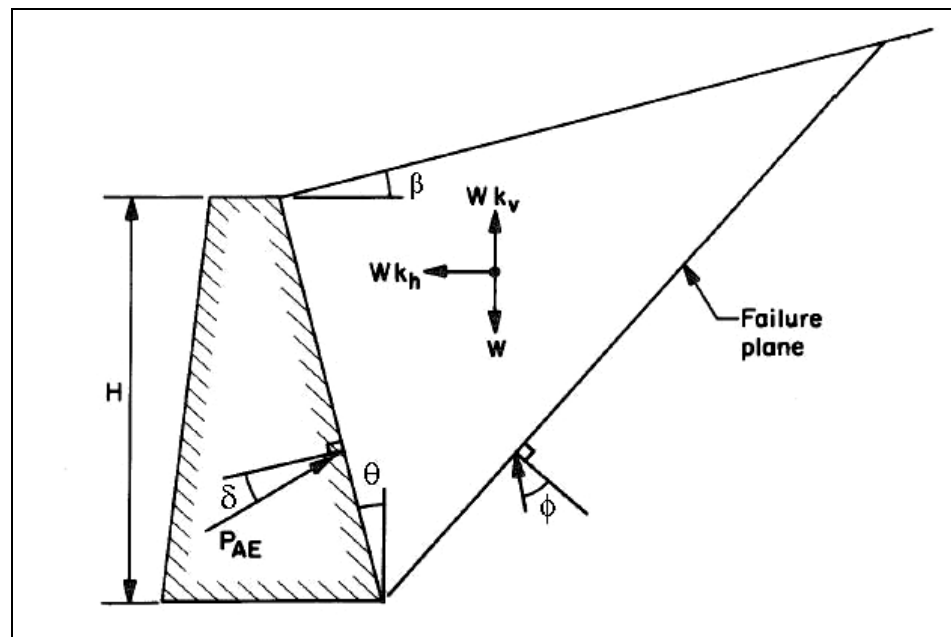


Figure 2.1.1.1 Forces in Mononobe-Okabe Analysis

2.1.2 Other studies

A displacement-based method for gravity walls is developed by Richards and Elms (1979). The mass of the wall is taken into account in the analysis based on M-O

method and Newmark's sliding block analogy. Figure 2.1.2.1 shows the forces acting on the gravity wall by gravitational and pseudo-static accelerations considered in the analysis.

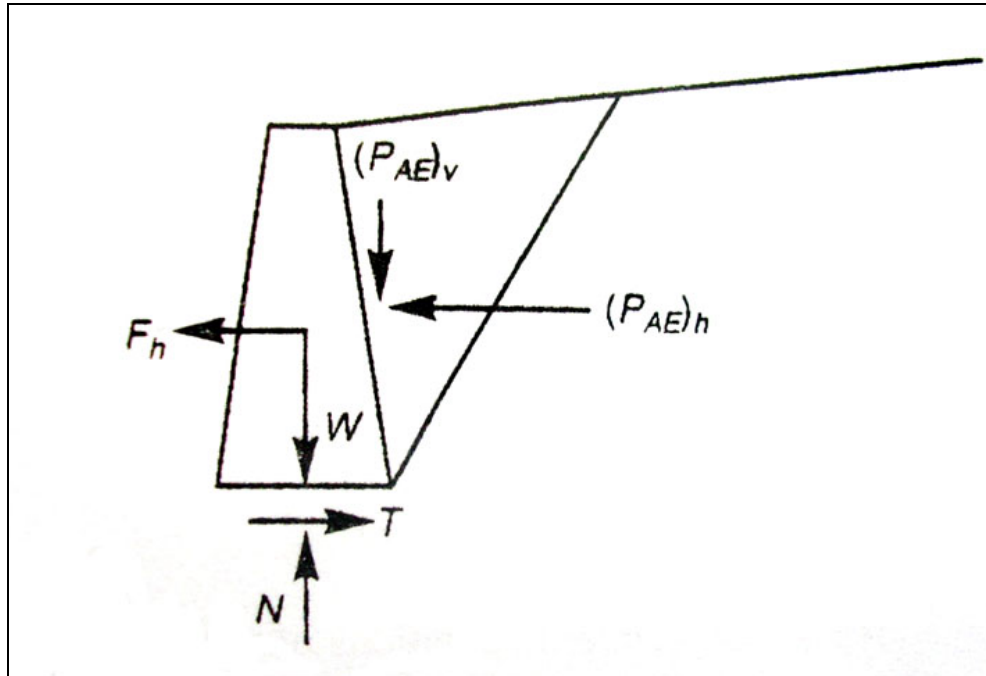


Figure 2.1.2.1 Forces considered in Richards and Elms method

Dimarogona (1983) developed an analytical method for any mode of wall movement. The method is an extension of static earth pressure theory by Dubrova (1960) that considers the rotation of a failing retaining wall about any point. Dimarogona concluded that the distribution of dynamic lateral earth pressures is not hydrostatic as assumed by M-O method but rather parabolic which is in agreement with experimental results.

Nadim and Whitman (1984) proposed a model for determining the seismically induced permanent rotation and translation of gravity walls retaining dry cohesionless backfill. The proposed model and the dynamic forces acting on the wall are shown in Figure 2.1.2.2. An important conclusion of the study is that, for a tilting wall, when the wall starts to rotate, its rotational acceleration is positive and the line of action of the force on the wall drops below the lower third point.

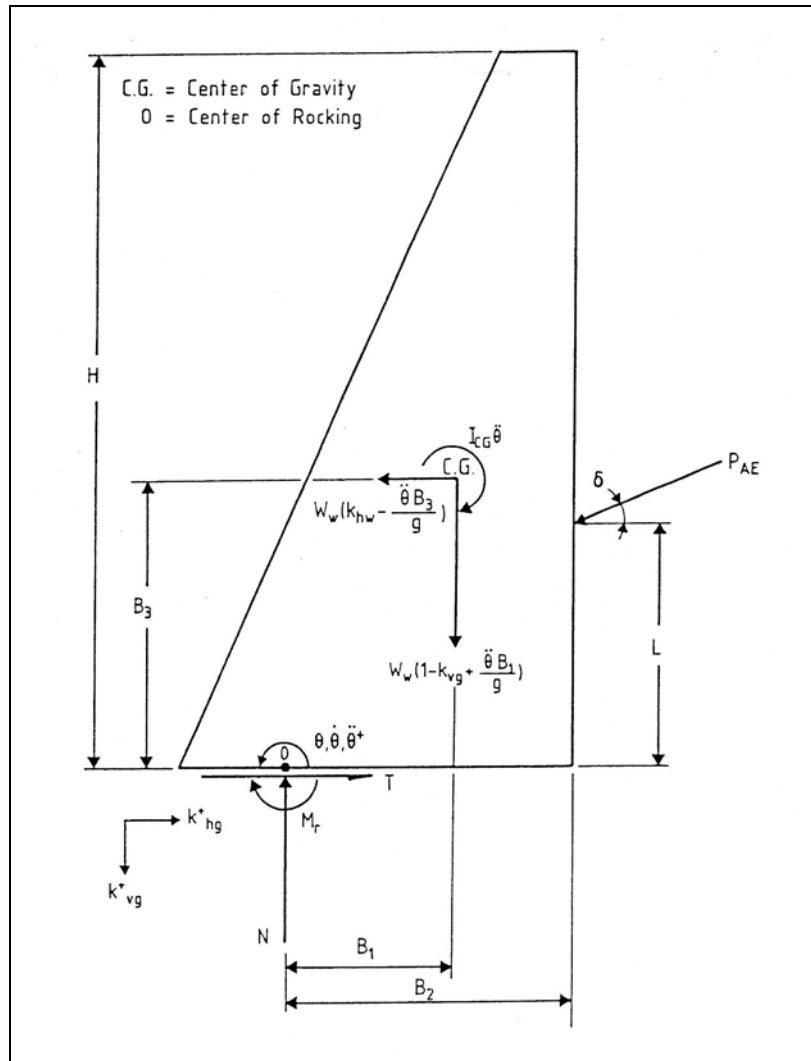


Figure 2.1.2.2 Dynamic forces acting on the wall (Nadim and Whitman, 1984)

Richards-Elms (1979) method is studied in detail and factors affecting the choice of a suitable safety factor are investigated by Whitman and Liao (1984). Uncertainties about modelling the wall as a sliding block, time histories of ground motion and strength parameters are examined and recommendations are made.

Das and Puri (1996) presented an improved pseudo-static method for prediction of the static and dynamic forces on rigid retaining walls. The solution method is based on the wall geometry, inclination of the backfill, surcharge, strength parameters of the backfill and the adhesion between the wall and backfill. It is found that the assumption by Prakash and Saran (1966) that cohesion of the

backfill is equal to the adhesion leads to conservative results for the dynamic force.

A new theory based on intermediate soil wedge concept is developed by Zhang et al (1998) for determining the dynamic lateral pressures on walls under a condition between active and passive status. The dynamic earth pressure is separated into four components as: the weight of the soil wedge, seismic inertial force, surcharge on backfill and soil vibro-densification effect at or near neutral state. New equations are derived for the pressure distribution of each component depending on the level of wall movements as well as the inertial acceleration distribution. Good agreement was found between the results of the proposed method and those obtained from previous model tests.

2.2 Analytical and numerical methods based on linear elastic or elasto-plastic theory

2.2.1 Wood (1973) solution

Wood (1973) developed an elastic solution for seismic pressures on rigid retaining walls. The solution is based on the analysis of a homogenous linear elastic soil layer between two rigid walls underlain by a rigid base (Figure 2.2.1.1). Wood stated that the dynamic amplification can be neglected for base input motions with frequencies less than half of the fundamental frequency of the soil layer. The following equations are suggested for the dynamic thrust and bending moment about the base induced by ground motion (after Kramer, 1996):

$$\Delta P_{EQ} = \gamma H^2 \frac{a_h}{g} F_p \quad (2.2.1.1)$$

$$\Delta M_{EQ} = \gamma H^3 \frac{a_h}{g} F_m \quad (2.2.1.2)$$

where; ΔP_{EQ} = dynamic thrust,

a_h = maximum horizontal acceleration

g = gravitational acceleration

F_p, F_m = dimensionless factors given in Figure 2.2.1.2

Wood's solution results in soil pressures significantly larger than those by M-O method. It is concluded that the solution is conservative to the other methods and can be used satisfactorily as a first approximation for many problems.

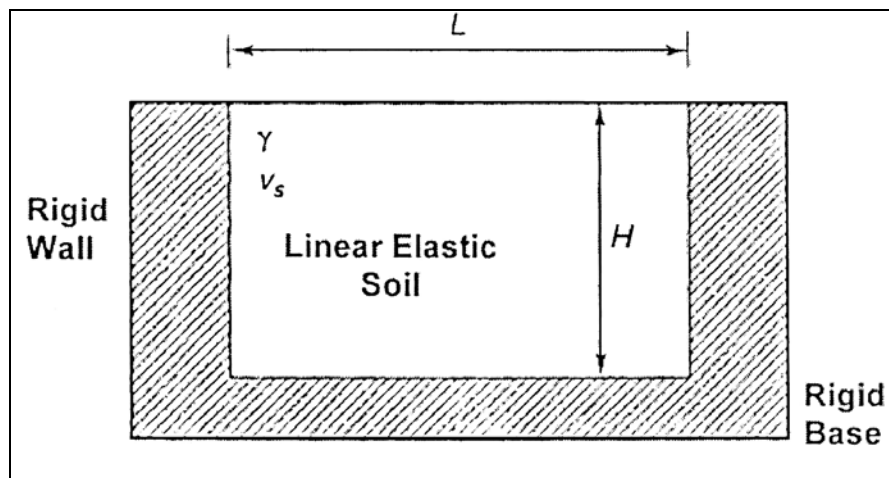


Figure 2.2.1.1 Wood's Model (after Kramer, 1996)

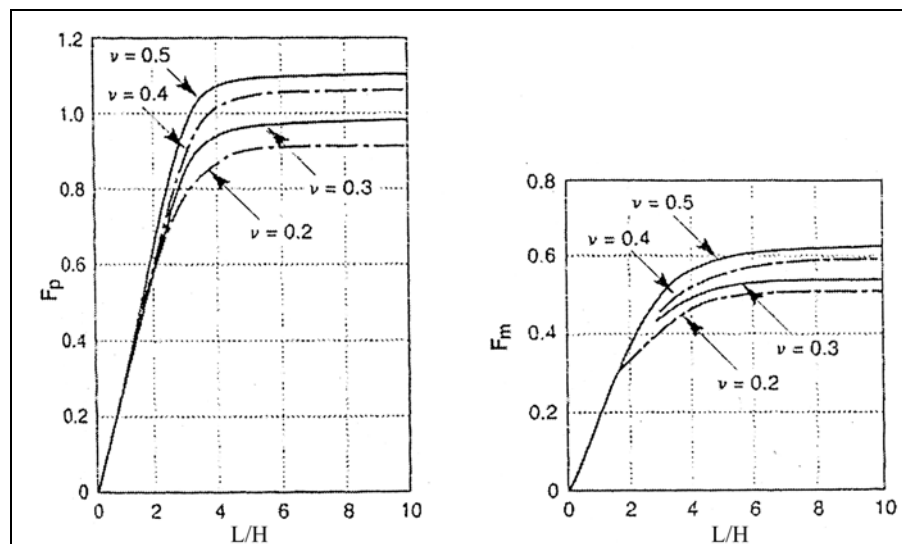


Figure 2.2.1.2 Dimensionless factors for dynamic thrust and moment by Wood(1973) (after Kramer, 1996)

2.2.2 Steedman and Zeng (1990) solution

M-O method assumes uniform acceleration at the soil wedge behind the wall. A pseudo-dynamic approach that accounts for the phase changes and amplification in the backfill is suggested by Steedman and Zeng (1990).

Effect of phase change between base and surface:

A typical fixed base cantilever wall shown in Figure 2.2.2.1 is considered. For harmonic base motion, the acceleration at depth z and time t can be expressed as:

$$A(z, t) = k_h g \sin \omega \left(t - \frac{H - z}{V_s} \right) \quad (2.2.2.1)$$

The weight of the wedge is:

$$W = \frac{1}{2} \frac{\gamma H^2}{\tan \alpha} \quad (2.2.2.2)$$

Considering a horizontal thin element of the wedge at depth z , the total horizontal inertia force Q_h can be obtained by integration along the height of the wall as:

$$Q_h = \int_0^H \rho \left(\frac{H - z}{\tan \alpha} \right) A(z, t) dz \quad (2.2.2.3)$$

Resolving the forces for the equilibrium of the wedge OAB leads to the expression of the total force acting on the wall, P_{AE} and K_{AE} as:

$$P_{AE} = \frac{Q_h \cos(\alpha - \phi) + W \sin(\alpha - \phi)}{\cos(\delta + \phi - \alpha)} \quad (2.2.2.4)$$

$$K_{AE} = \frac{2P_{AE}}{\gamma H^2} \quad (2.2.2.5)$$

K_{AE} is dependent on $H / (TV_s)$ which is the ratio of time for a wave to travel the full height to the period of the base motion. The influence of phase change on earth pressure coefficient is given in Figure 2.2.2.2.

Influence of amplification:

Assuming the lateral acceleration varies linearly from the base of the layer to the ground surface with a constant amplification factor f_a , the acceleration at depth z is modified as:

$$A(z, t) = \left[1 + \frac{H-z}{H} (f_a - 1) \right] k_h g \sin \omega \left(t - \frac{H-z}{V_s} \right) \quad (2.2.2.6)$$

and Q_h is obtained similarly from Equation 2.2.2.3. Figure 2.2.2.3 shows the variation of the earth pressure coefficient with the amplification factor.

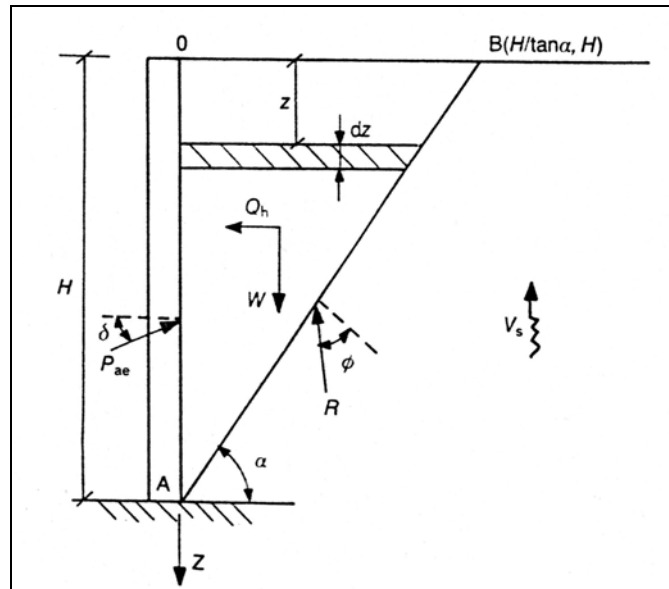


Figure 2.2.2.1 Assumptions, notations and forces for calculation of dynamic earth pressure (Steedman and Zeng, 1990)

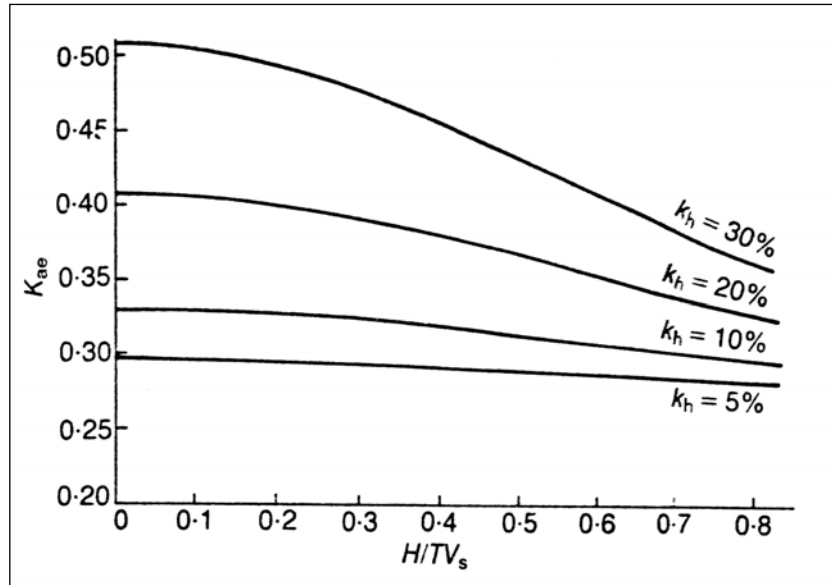


Figure 2.2.2.2 Influence of phase change on earth pressure coefficient (Steedman and Zeng, 1990)

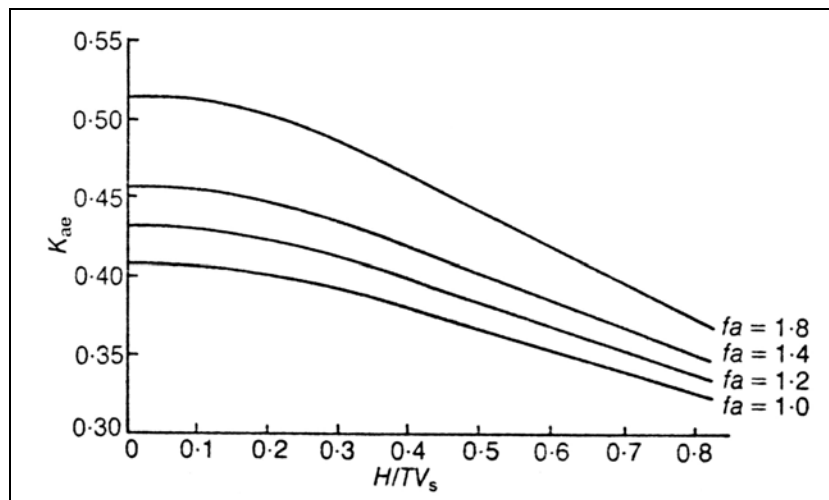


Figure 2.2.2.3 Influence of amplification factor, f_a on earth pressure coefficient (Steedman and Zeng, 1990)

2.2.3 Other studies

Matsuo and Ohara (1960) developed a solution for the dynamic earth pressures on rigid walls making translational motions. The basic equations were derived using elastic wave theory, assuming that the wall is stationary and no vertical displacement occurs in the soil mass, with the waves travelling in the soil and

impinging on the surface of the wall creating the resultant stresses (after Nazarian and Hadjian, 1979). Figure 2.2.3.1 shows the computed earth pressures and point of application of the resultant force.

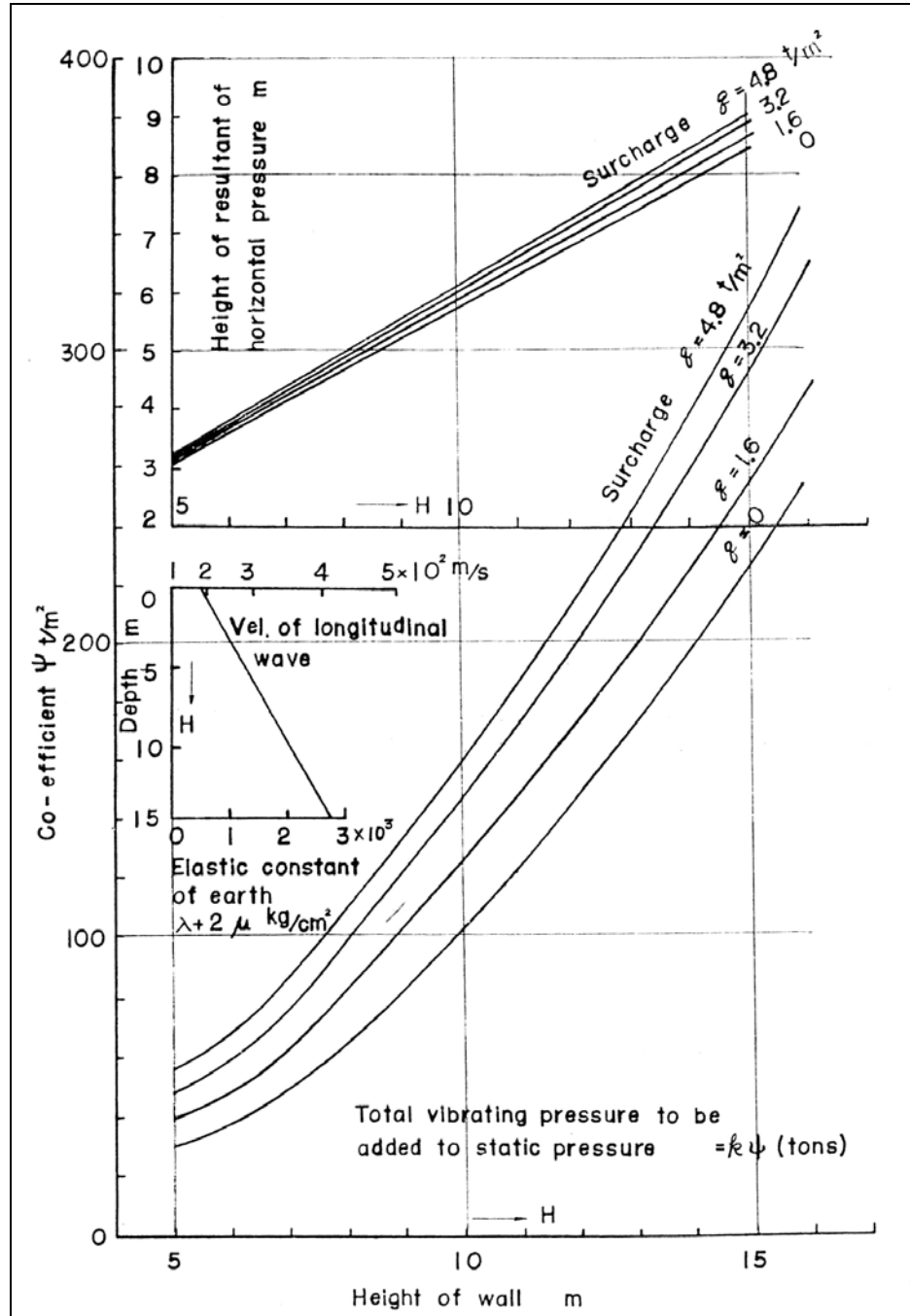


Figure 2.2.3.1 Dynamic earth pressures and point of application of the resultant force (Matsuo and Ohara, 1960)

Scott (1973), (after Nazarian and Hadjian, 1979) has studied the dynamic response of rigid walls using a one-dimensional elastic shear beam connected to the wall by springs (Figure 2.2.3.2). Formulas for dynamic pressures for constant and variable soil properties are given. It is indicated that the results are in accordance with Matsuo and Ohara (1960) but higher than M-O method. The application point is acted at a distance of $0.64H$ from the base (after Çalışan,1999).

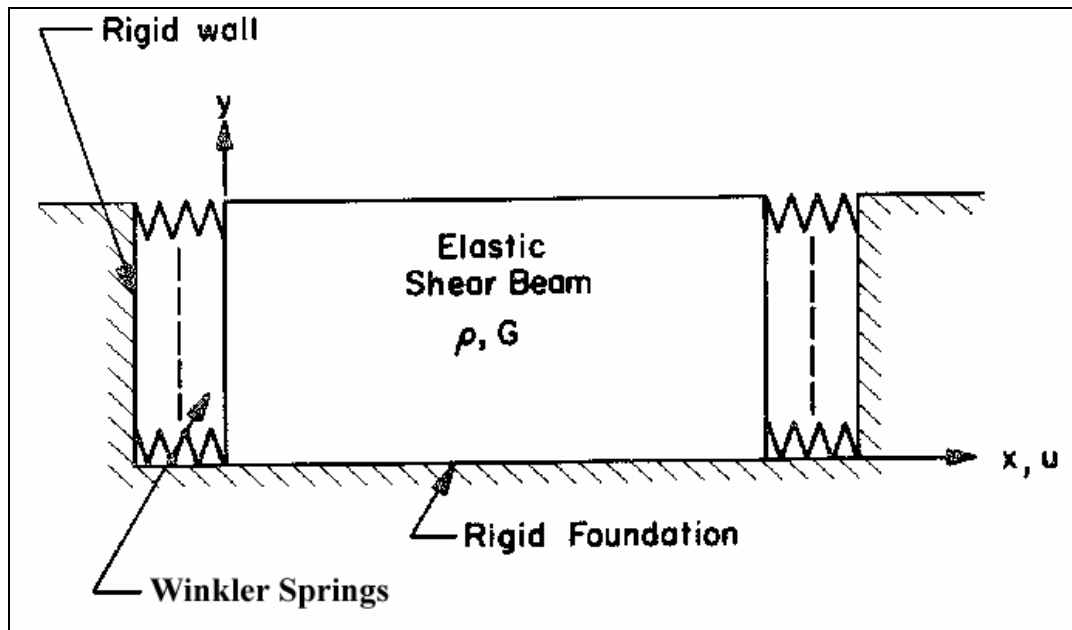


Figure 2.2.3.2 Scott's (1973) Model (after Wood, 1973)

Finite element solution of dynamic response of gravity retaining walls with dry cohesionless backfill was made by Nadim and Whitman (1983). Figure 2.2.3.3 shows the proposed finite element model. Permanent displacements of the wall are investigated. It is concluded that the amplification of motion in backfill has a significant effect on the permanent displacements as shown in Figure 2.2.3.4.

Seismic response of a flexible wall is studied by Siddharthan and Maragakis (1989) using finite element method. The results led to the conclusion that bending moments given by current design procedures are nonconservative for stiffer walls.

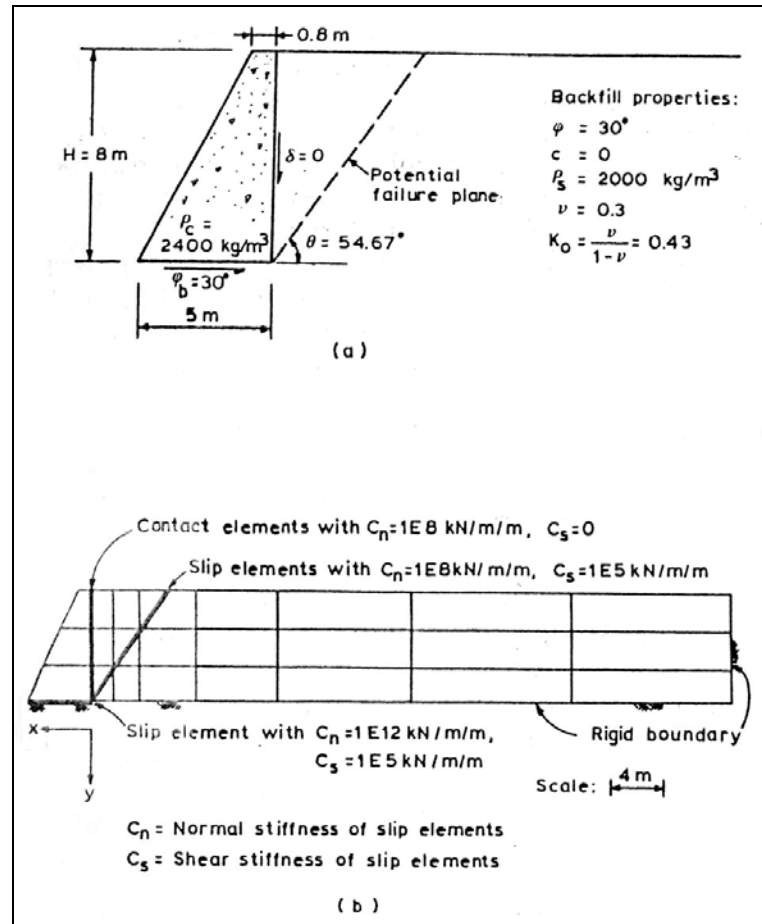


Figure 2.2.3.3 Gravity wall considered and its finite element idealisation (Nadim and Whitman, 1983)

Bakeer et al (1990) conducted finite element analyses considering different modes of wall movement, and compared the results with experimental findings of the tests conducted at University of Washington (Ishibashi and Fang, 1987).

The finite element program ANSYS is used for the analyses. The model examined is shown in Figure 2.2.3.5. The wall elements are connected to surrounding soil elements by horizontal and vertical interface elements. A sinusoidal acceleration time history is applied along the line a-b in Figure 2.2.3.5. Different modes of wall displacement examined are: active rocking of free wall (ARC), active horizontal translation (AT), active rotation about top (ART) and active rotation about base (ARB).

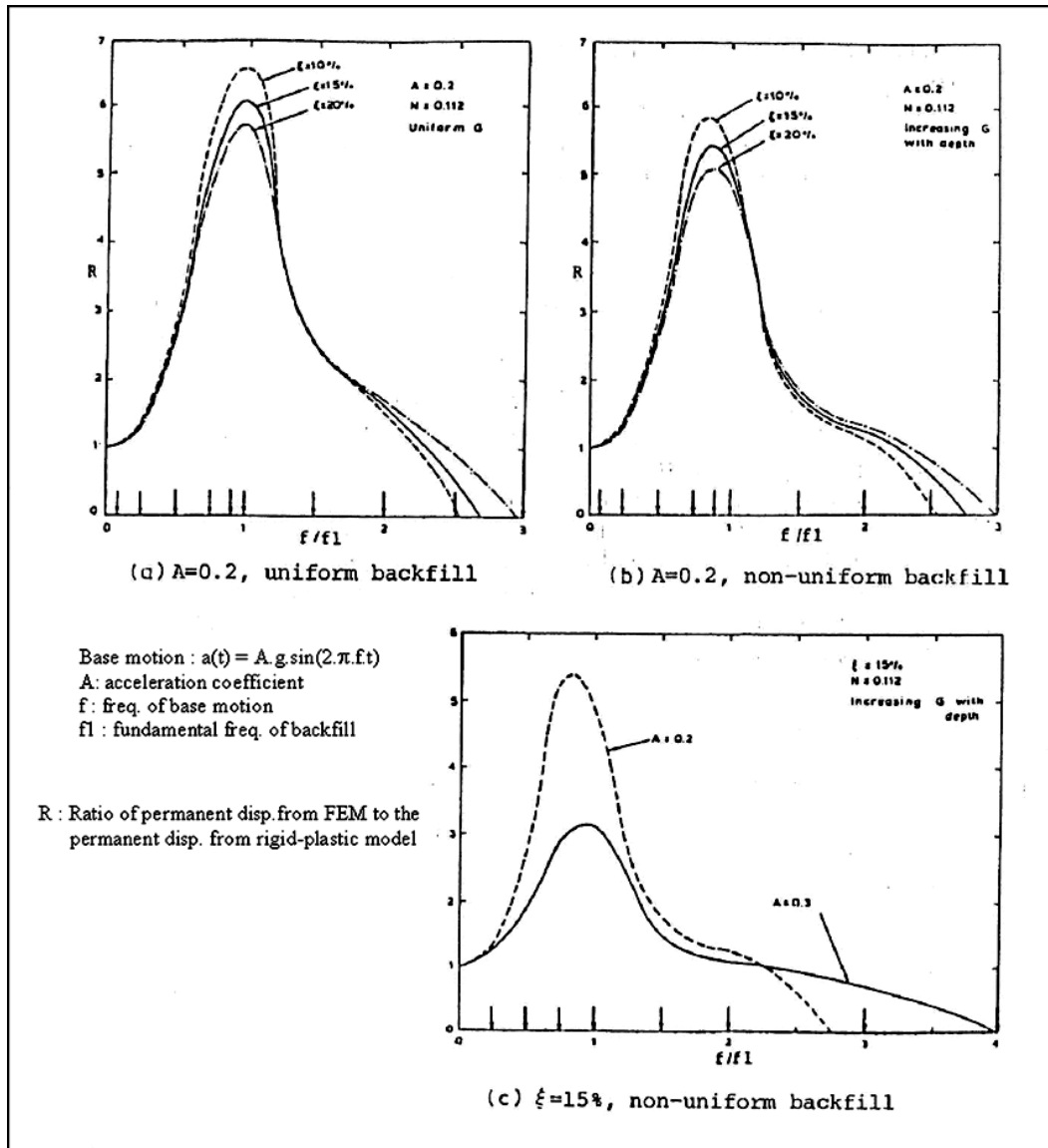


Figure 2.2.3.4 Effects of ground motion amplification on permanent wall displacement (Nadim and Whitman, 1983)

Figure 2.2.3.6 shows the analytical and experimental results of dynamic earth pressure distribution. Location of the resultant force values of analytical solution and experimental studies are plotted on Figure 2.2.3.7. Based on the finite element analyses and experimental research, the following conclusions are made by Bakeer et al (1990):

- The magnitude and distribution of the dynamic earth pressure depends on the mode of movement.

- The earth pressure distribution is always non-hydrostatic during all modes of deformation.
- Mononabe-Okabe solution may underestimate the magnitude of the dynamic earth pressures.

Dynamic pressures on rigid vertical walls retaining uniform elastic soil layer of constant thickness are studied by Veletsos and Younan (1994). An analytical solution assuming the presence of no vertical stress and complete bonding between the wall and soil is developed. The investigated system is shown in Figure 2.2.3.8. Both harmonic base motions and actual earthquake records are considered. Two alternative models (frequency dependent and frequency independent) to Scoot's (1973) model are proposed to consider the effect of soil in the vicinity of the wall on the dynamic response of the system. Figure 2.2.3.9 shows the response curves for base wall-shears obtained by analytical solution and frequency independent model. The significant effect of the frequency ratio (the ratio of the base motion frequency to the fundamental frequency of the soil) on the shear force at the base of the wall thus the lateral soil forces acting on the wall can be seen in this figure.

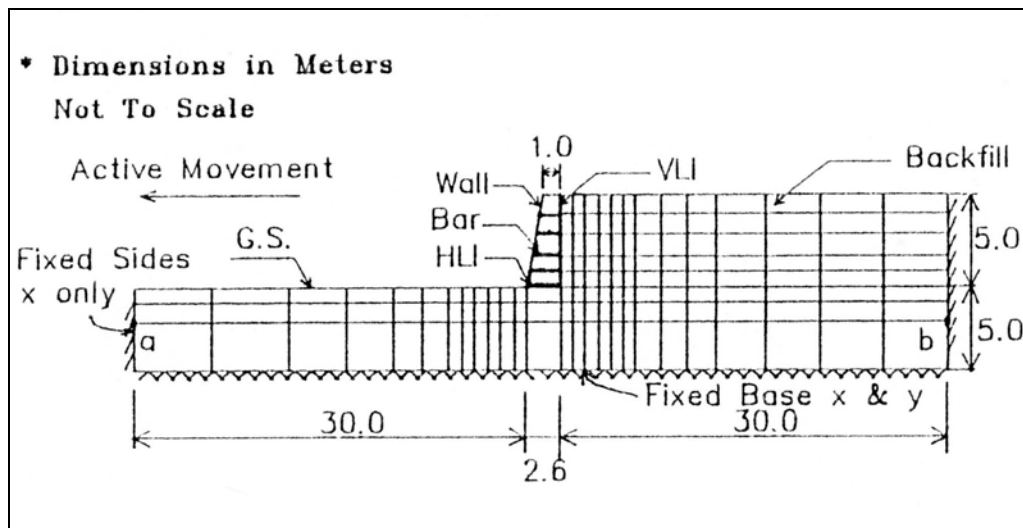


Figure 2.2.3.5 Analytical retaining wall model (Bakeer et al, 1990)

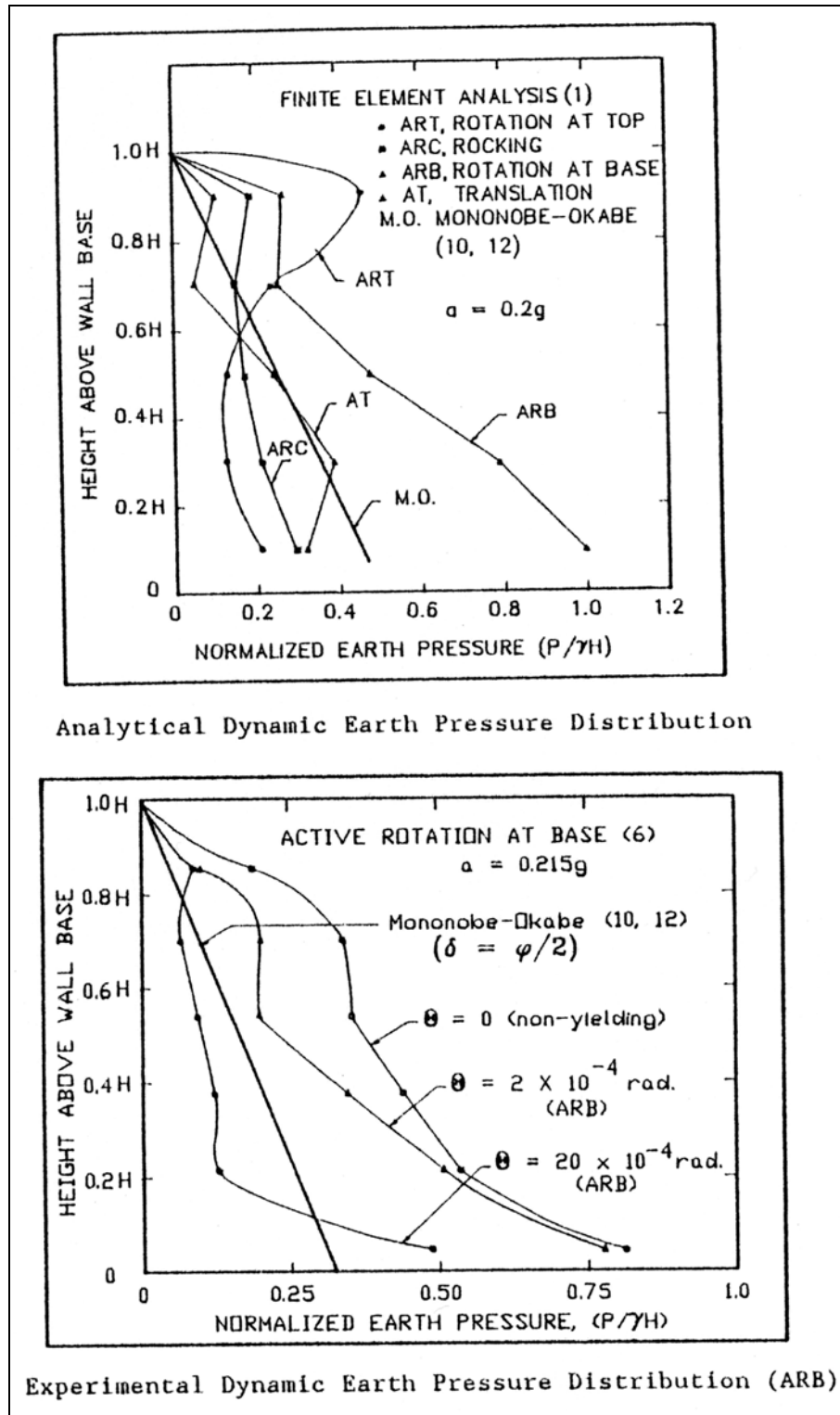
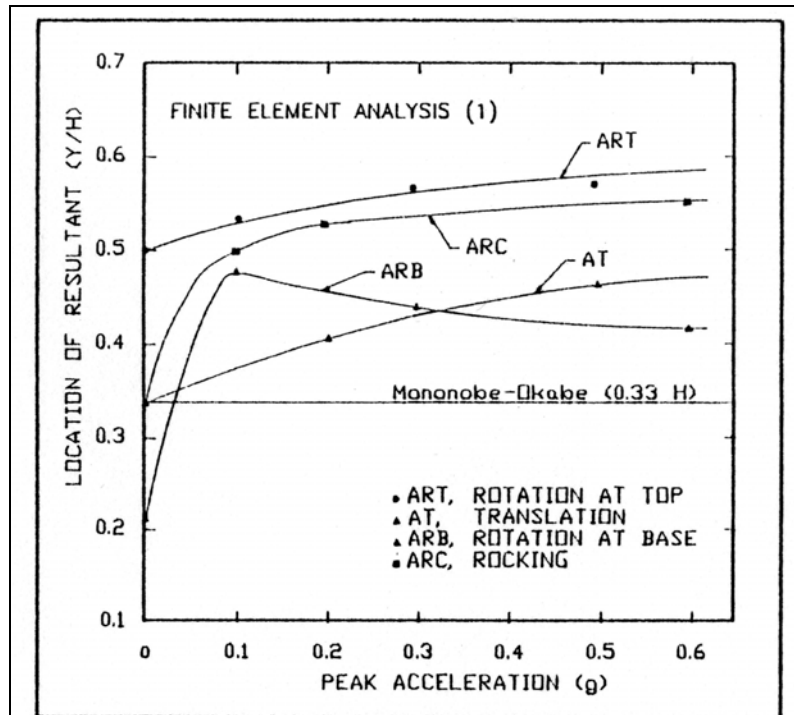
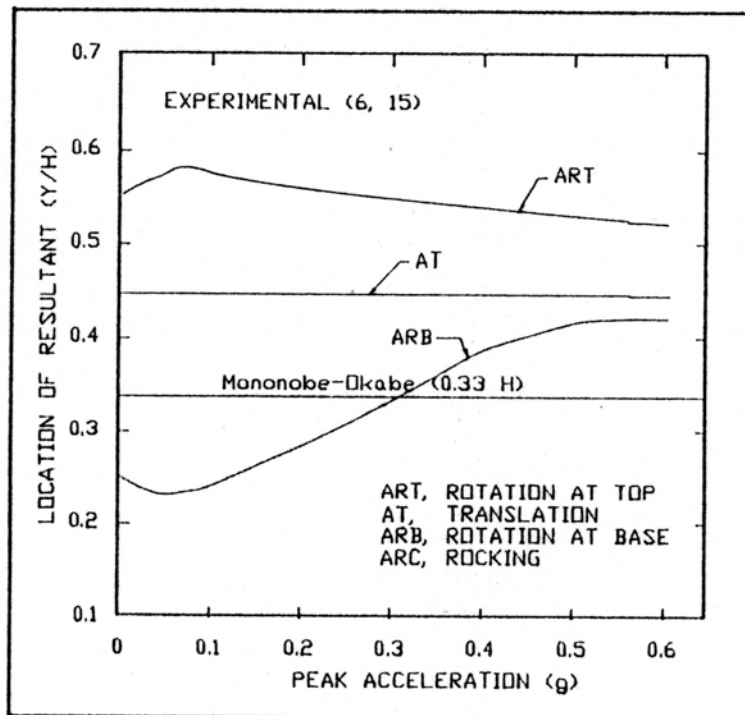


Figure 2.2.3.6 Analytical and experimental dynamic earth pressure distributions for active rotation at base (ARB) (Baker et al, 1990)



Analytical Location of the Resultant



Experimental Location of the Resultant

Figure 2.2.3.7 Analytical and experimental location of the resultant force (Bakeer et al, 1990)

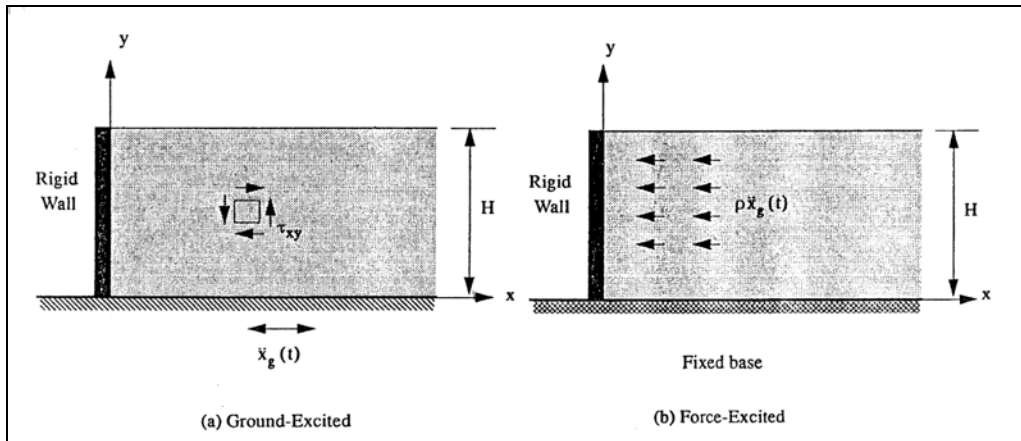


Figure 2.2.3.8 System considered by Veletsos and Younan (1994)

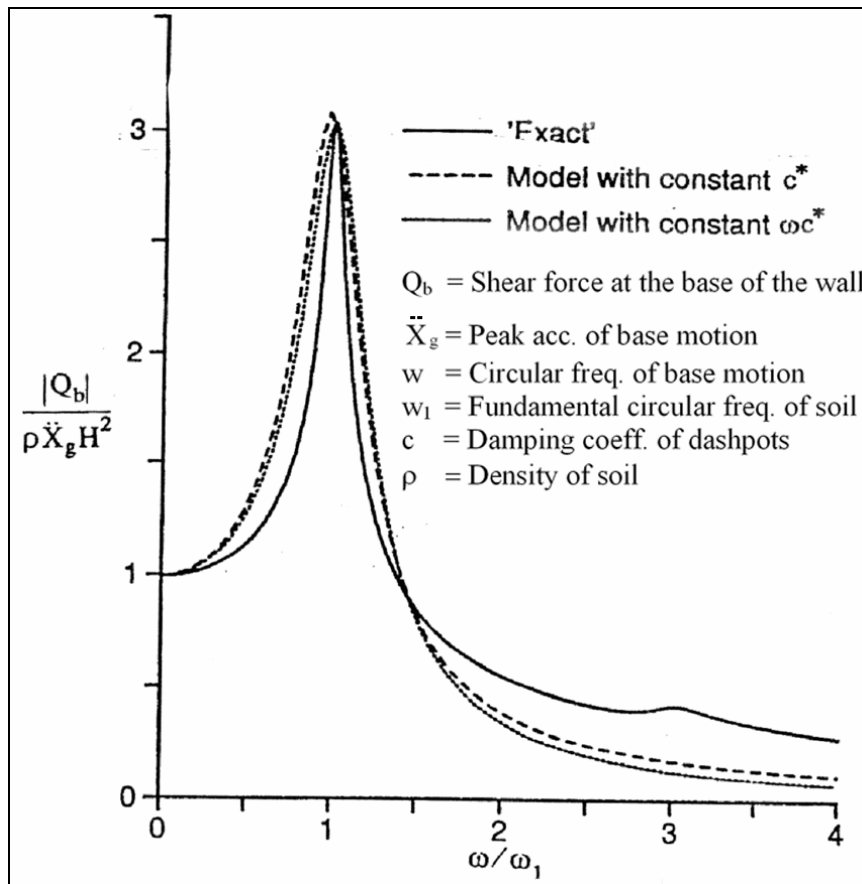


Figure 2.2.3.9 Comparison of frequency response curves for base shear computed from analytical solution and model with frequency-independent parameters (Veletsos and Younan, 1994)

A comparison of pseudo-static and non-linear dynamic behaviour of gravity retaining walls is made by Woodward and Griffiths (1996). Finite element method

is used for both pseudo-static and dynamic analyses. Only the relative sliding is simulated and no gap is allowed between the wall and backfill. The interface between the wall and foundation soil is assumed as either smooth (relative sliding is allowed with no friction) and rough (completely bonded). It is concluded that the pseudo-static finite element approach gives results in good agreement with analytical methods. The results of the dynamic analyses showed that the earth pressure coefficient and point of application can vary considerably during earthquake.

Veletsos and Younan (1997) examined the dynamic response of flexible walls constrained against rotation at their base, by using an analytical method of analysis. It was assumed that no vertical stresses are present and there is complete bonding between the soil and the wall. The soil-wall system studied is shown in Figure 2.2.3.10. Both harmonic base motions and actual earthquake record are considered. It is observed that the wall displacements and pressures induced by ground shaking are highly dependent on the flexibility of the wall and the rotational stiffness of the base. It is concluded that the total force obtained is in reasonable agreement with that computed by Mononobe-Okabe method for realistic wall flexibilities when the dynamic amplification effects are neglected. The amplification factors at the base shear of wall for different wall and base stiffness values and frequency ratios are plotted in Figure 2.2.3.11.

A 2-D finite element solution is used to investigate the seismic response of rigid bridge abutments retaining and founded on dry sand by Al-Homoud and Whitman (1999). The proposed finite element model is shown in Figure 2.2.3.12. The wall is modelled as a rigid substructure and interface elements are used between the wall and soil at the backface of the wall and under its base to allow for relative sliding and gap. The non-linear stress-strain behaviour of soil is modelled by a failure surface and hardening cap together with an associated flow rule. The cap surface is activated only for the foundation soil to simulate the compaction during rocking displacement of the wall. A bridge abutment of 8m high and 3m wide is studied for different sinusoidal and earthquake motions. The results showed that the

dominant response of the gravity walls is the outward tilting during dynamic shaking and permanent tilt is present at the end of the shaking.

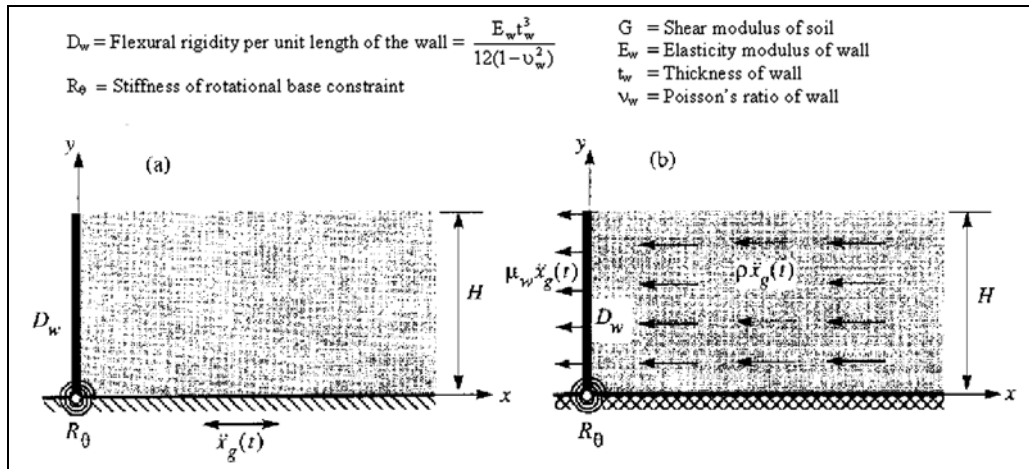


Figure 2.2.3.10 Soil-wall systems investigated by Veletsos and Younan (1997):
 a) Base excited system, b) Force excited system

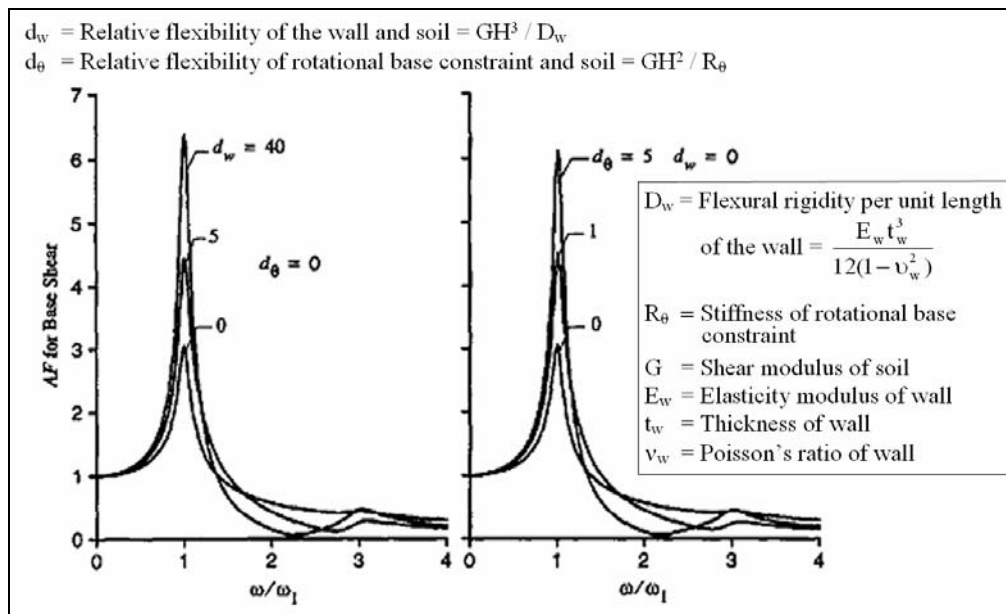


Figure 2.2.3.11 Amplification factors for base shear for different wall and base flexibilities (Veletsos and Younan, 1997)

Richards et al (1999) suggested a simplified kinematic method base on free-field solution to predict the seismic earth pressure distribution on retaining structures for different modes of deformation (rotation about top, rotation about bottom and

lateral translation). The soil is assumed as an elastic-perfectly plastic material with Mohr-Coulomb yield criterion and modelled by a series of springs as shown in Figure 2.2.3.13 that shows the considered model. Results of the method are compared with test results by Ishibashi and Fang (1987) and reasonably good agreement was obtained.

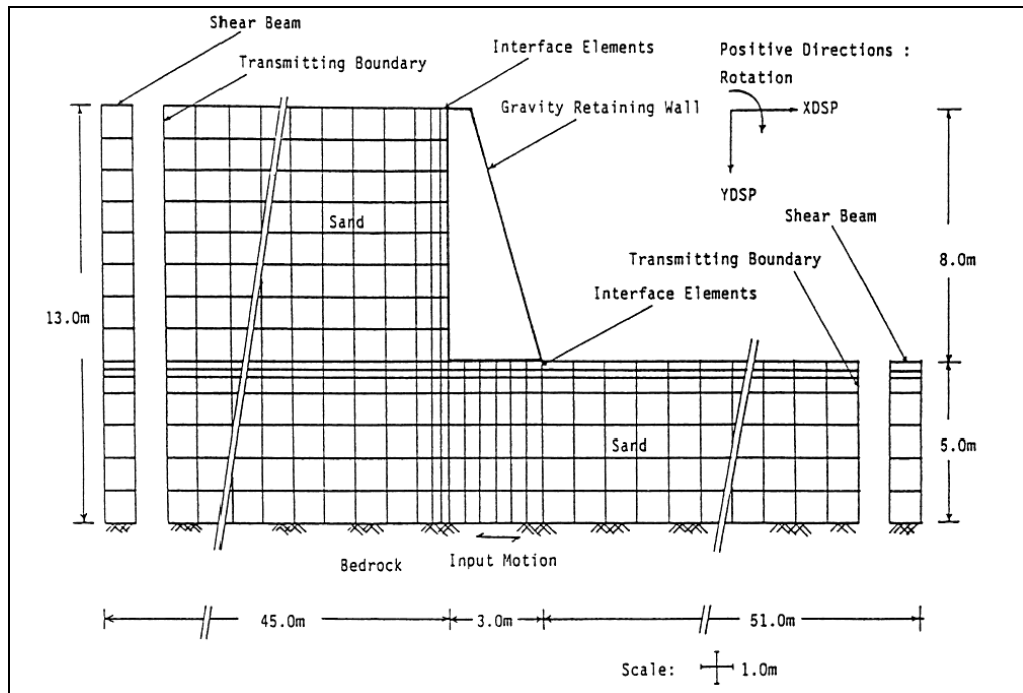


Figure 2.2.3.12 Finite element model for gravity wall problem (Al-Homoud and Whitman, 1999)

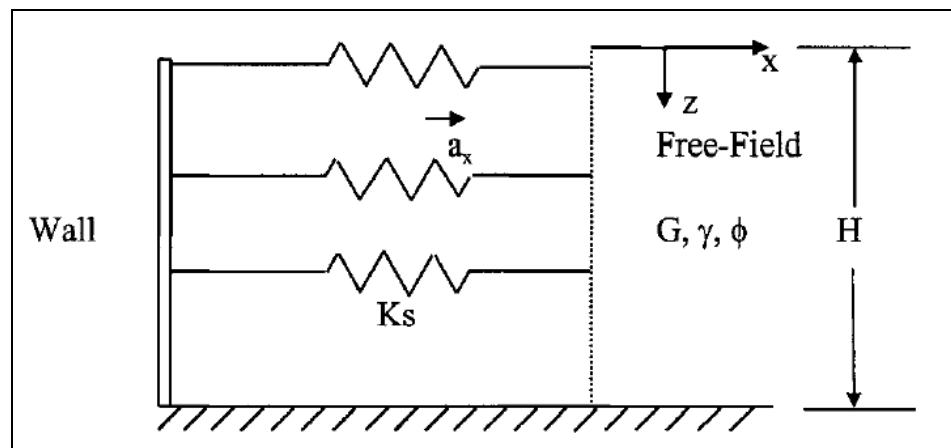


Figure 2.2.3.13 Model for dynamic pressure increment (Richards et al, 1999)

Wu and Finn (1999) presented design charts for seismic pressures acting on rigid retaining walls. An analytical solution is developed for homogenous backfill and finite element analyses are conducted for non-homogenous backfills. Charts for peak seismic thrusts vs. ratios of the frequency of ground motion to the natural vibration frequency of the system are obtained considering three different soil profiles and 250 combinations of base motions for each profile. It is concluded that, Wood (1973) solution, often used in practice underestimates the thrusts for the vicinity of resonance case, and overestimates for high frequency ratios. Figure 2.2.3.14 shows one of the proposed charts of peak seismic thrust vs. frequency ratio.

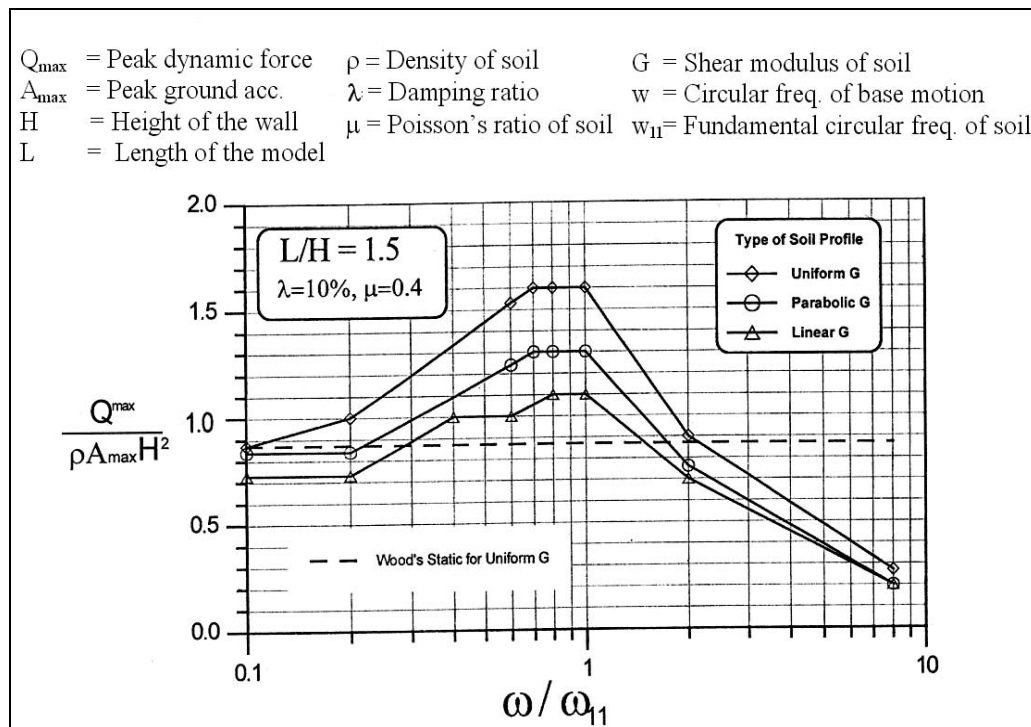


Figure 2.2.3.14 Peak seismic thrust curves for $L/H = 1.5$ (Wu and Finn, 1999)

Younan and Veletsos (2000) studied the dynamic response of flexible walls retaining a uniform, linear-elastic soil layer. An analytical method is proposed to predict the response of cantilever and top-supported retaining walls and the effect of flexibility is investigated. It is assumed that no vertical stresses develop in the medium and there is complete bonding between the wall and soil. The wall is fixed

against deflection and rotation at the base to which the ground motion is applied. Both harmonic and earthquake motions are examined and the effects of long-period excitations are considered. It is concluded that the total lateral thrust for cantilever walls may be less than one-half of that obtained for fixed-based rigid walls with a larger reduction in the bending moment at the base.

Wu (1999) developed a displacement model for rigid walls considering the non-linear soil properties and any water condition behind the wall (after Wu and Prakash, 2001). Springs and dashpots are used to simulate the stiffness and damping behaviour in sliding and rocking in the model. The predicted displacement was in reasonable agreement with centrifuge test by Zeng (1998).

The performance of L-shaped reinforced concrete walls during earthquakes is examined by Gazetas et al (2004). The base excitations with either high or low dominant frequencies of peak ground acceleration (PGA) of 0.40g and relatively short-duration are considered. Soil is modelled as both linear elastic and elastoplastic (using Mohr-Coulomb yield criterion) materials. Figure 2.2.3.15 shows the system examined and the lateral pressure distributions induced by base motion. It is concluded that L-shaped retaining walls are subjected to dynamic forces smaller than those predicted by M-O method in many cases, especially for high frequency excitation. Exceptions to this rule exist when there is significant amplification of the ground motion in the soil. However, it is noted that, even higher pressures than M-O are present, the retaining systems possess sufficient ductility capacity, in the form of unhindered slippage at their base, that they can survive even a strong event with minor damage.

Analytical results by Veletsos and Younan (1997) are verified by Psarrapoulos et al (2005) by conducting finite element analyses. The effects of the wall flexibility and base rocking stiffness are also investigated. Both homogenous and inhomogenous soil layers resting on rigid base are considered. Additionally, a two-layered system is examined that accounts for the lateral movement of the wall. Figure 2.2.3.16 shows the systems and assumptions used in the study.

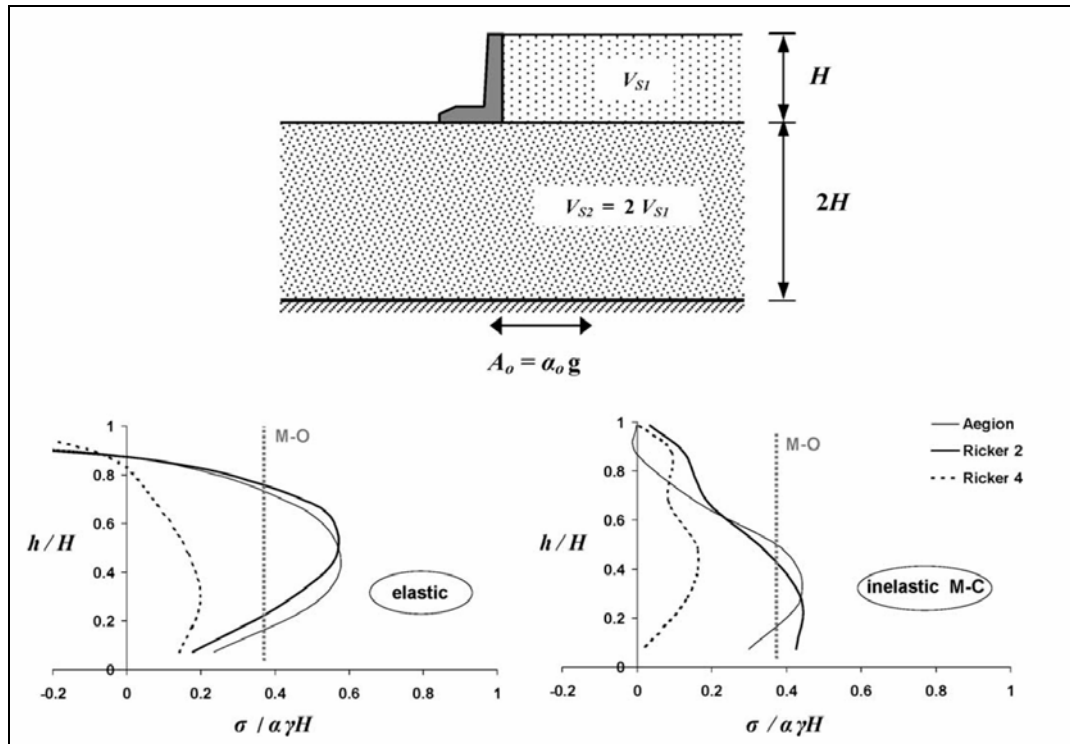


Figure 2.2.3.15 Two-layered model and distribution of dynamic earth pressures (Gazetas et al, 2004)

The wall is modelled by beam elements and the rotational stiffness of the foundation is simulated by a rotational spring at the base that is fixed in both horizontal and vertical directions for one-layer systems. For the two-layer system, both the wall and soil are modelled by plane-strain elements.

The influence of the wall flexibility and base rocking stiffness is illustrated in Figure 2.2.3.17. It is observed that the shape of the lateral seismic pressure distribution is dependent on the wall stiffness.

A comparison of the results of one-layer and two-layer models is shown in Figure 2.2.3.18. The influence of the base rocking stiffness on the shape of the pressure distribution can clearly be seen in the figure.

The models examined by Psarropoulos et al (2005) assume full bonding between the wall and soil leading to unrealistic tensile stresses at the wall-soil interface that

can affect the overall response of the wall. There is insufficient information about the pressure values used in the pressure distributions if they are the values corresponding to the maximum lateral thrust at an instance or the maximum values obtained at each point during the analysis.

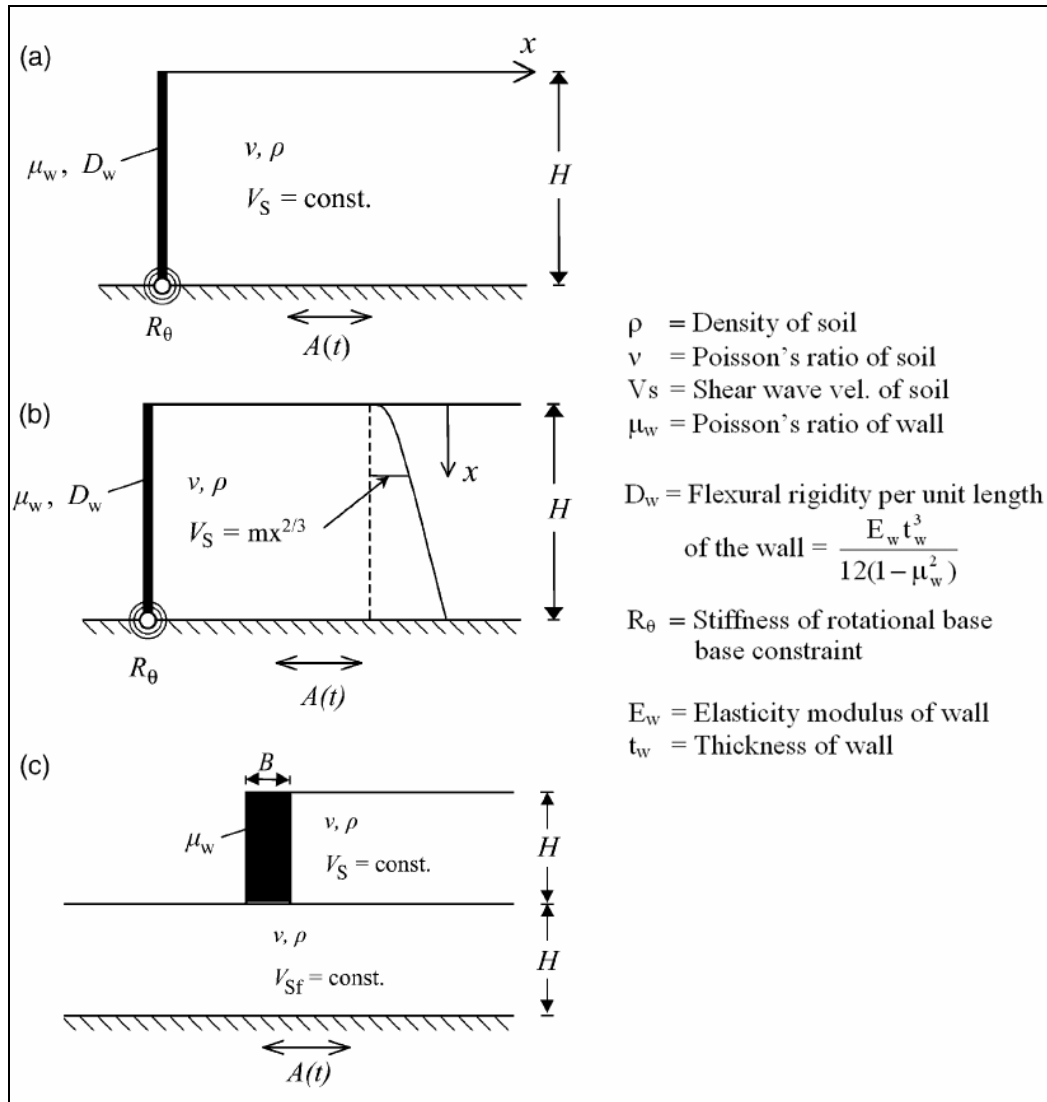


Figure 2.2.3.16 Systems examined by Psarropoulos et al (2005)

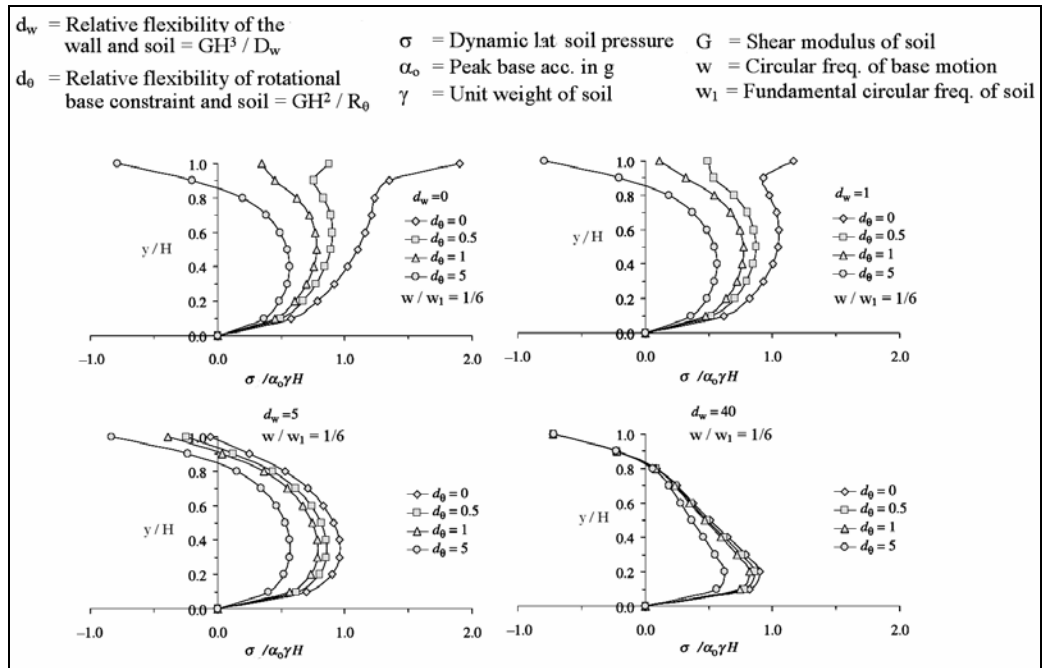


Figure 2.2.3.17 Dynamic earth pressure distributions for varying base rotational spring stiffness and wall flexibility (Psarropoulos et al, 2005)

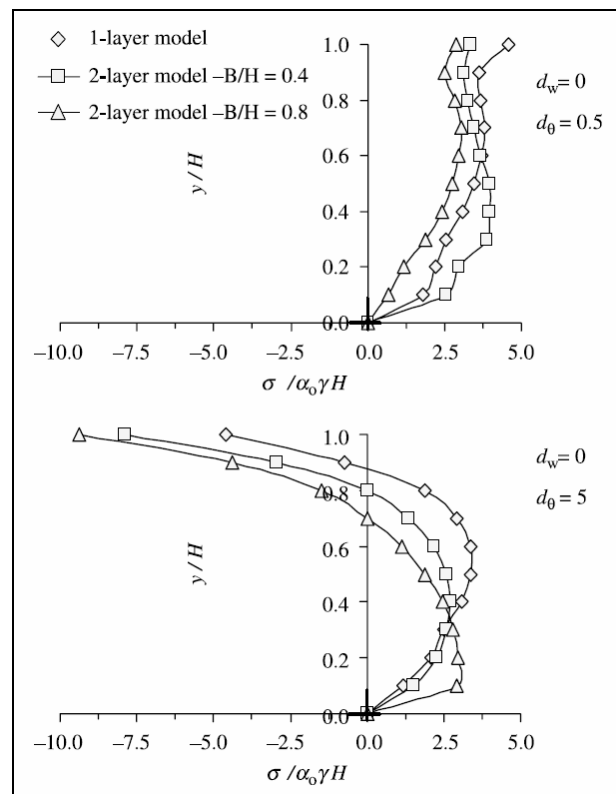


Figure 2.2.3.18 Dynamic earth pressure distributions in the case of resonance for different base stiffness and wall flexibility values (Psarropoulos et al, 2005)

Ostadan (2005) suggested a simplified method for the calculation of maximum seismic soil pressures for building walls resting on firm foundation soil. The method is based on conventional 1-D soil column analysis and considers the dynamic soil properties and the frequency content of the ground motion.

2.3 Experimental studies

Sherif et al (1982) conducted shaking table experiments to determine the dynamic stress distributions on rigid walls with granular backfill material. The model wall was designed so that it could rotate about top or bottom and translate.

Dynamic neutral increment thrust results for non-yielding retaining walls are compared to elastic solutions proposed by Matsuo and Ohara (1960) and Wood (1973) in Figure 2.3.1. It is seen that the dynamic neutral incremental thrust varies nonlinearly contrary to the elastic methods stated above. Variation of the application point of the total dynamic neutral force is given in Figure 2.3.2. An average value of $h/H=0.4$ is suggested for design purposes where h is the distance of the application point to the base and H is the height of the wall.

For a rigid translating wall, variation of the coefficient of total dynamic active earth pressure and point of application of the total dynamic active thrust are shown in Figures 2.3.3 and 2.3.4 respectively. It can be seen that the results are about 30% higher than the values computed by M-O. An average value of $h/H=0.45$ is proposed for the application point of the total active thrust.

Seismic behaviour of cantilever retaining walls were investigated by centrifuge model tests by Ortiz (1982). The prototype walls designed according to M-O method are subjected to lateral earthquake motions. The walls were instrumented with pressure and displacement transducers, acceleration and strain gauges (See Figure 2.3.5). Moment, pressure, shear and displacement distributions were obtained from the tests. Figure 2.3.6 shows the pressure distribution for one of the tests. The study has led to the following conclusions:

- The static earth pressure distributions obtained are not triangular as assumed by Coulomb's or Rankine's theory. However the resultant forces and points of application are in reasonable agreement indicating that Coulomb's theory estimates an average pressure distribution that is assumed as triangular.
- The dynamic response of the system is not only dependent on lateral accelerations, but also on the energy content of the earthquake indicated by the velocities. Maximum pressures are found to be closely associated with the velocities, maximum moments with the area under the acceleration spikes (changes in velocity).
- The dynamic pressure distributions are not triangular as for the static cases, although the centroids are about 1/3 of the height above the base.
- The M-O solution is in reasonable agreement with the experimental results (after Ortiz et al, 1983).

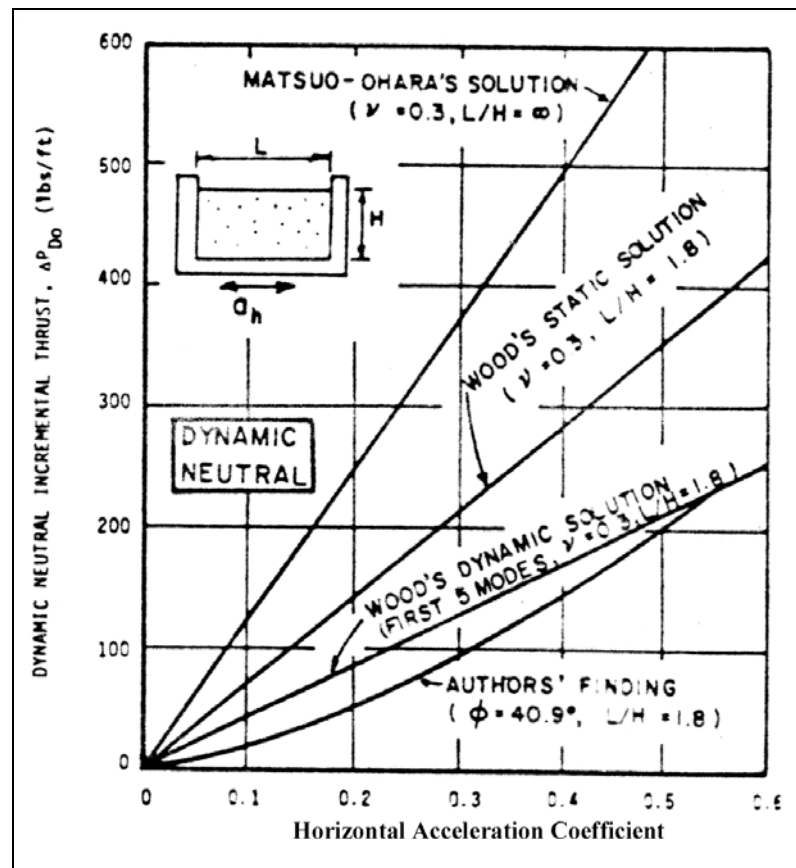


Figure 2.3.1 Dynamic neutral incremental thrust for a 1m high nonyielding wall (Sherif et al, 1982)

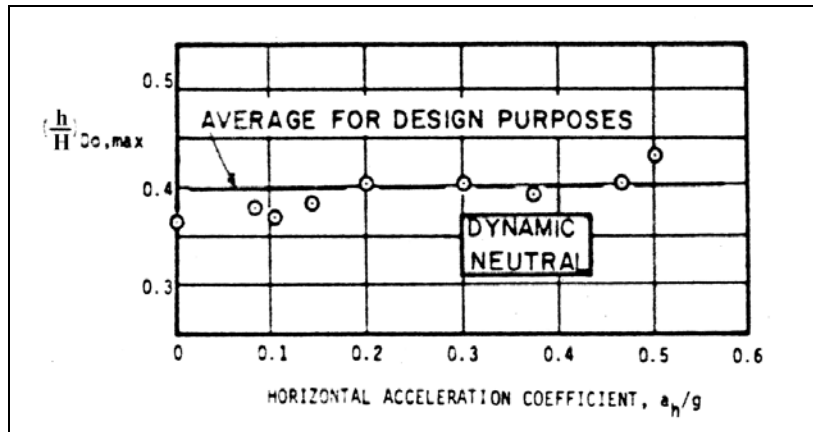


Figure 2.3.2 Variation of application point of total dynamic thrust for nonyielding wall (Sherif et al, 1982)

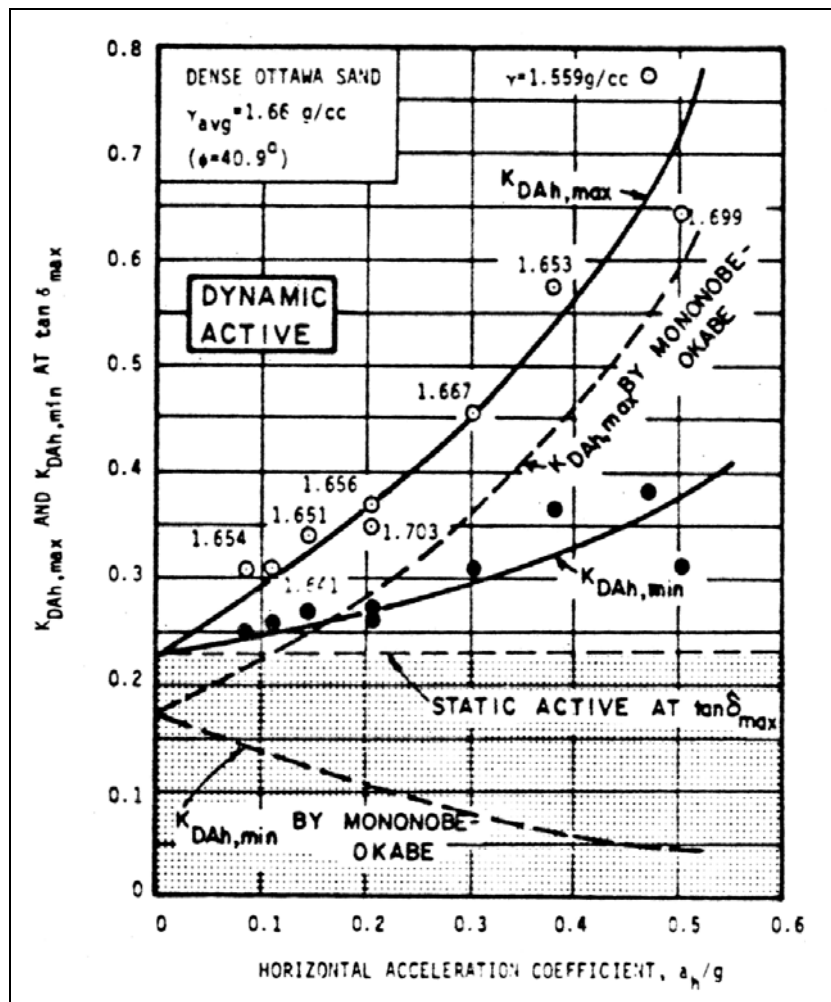


Figure 2.3.3 Variation of the coefficient of total dynamic active earth pressure (Sherif et al, 1982)

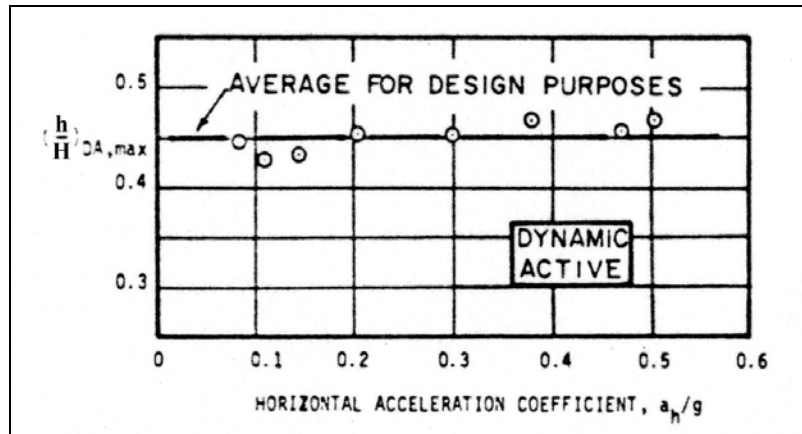


Figure 2.3.4 Variation of the application point of total dynamic active thrust (Sherif et al, 1982)

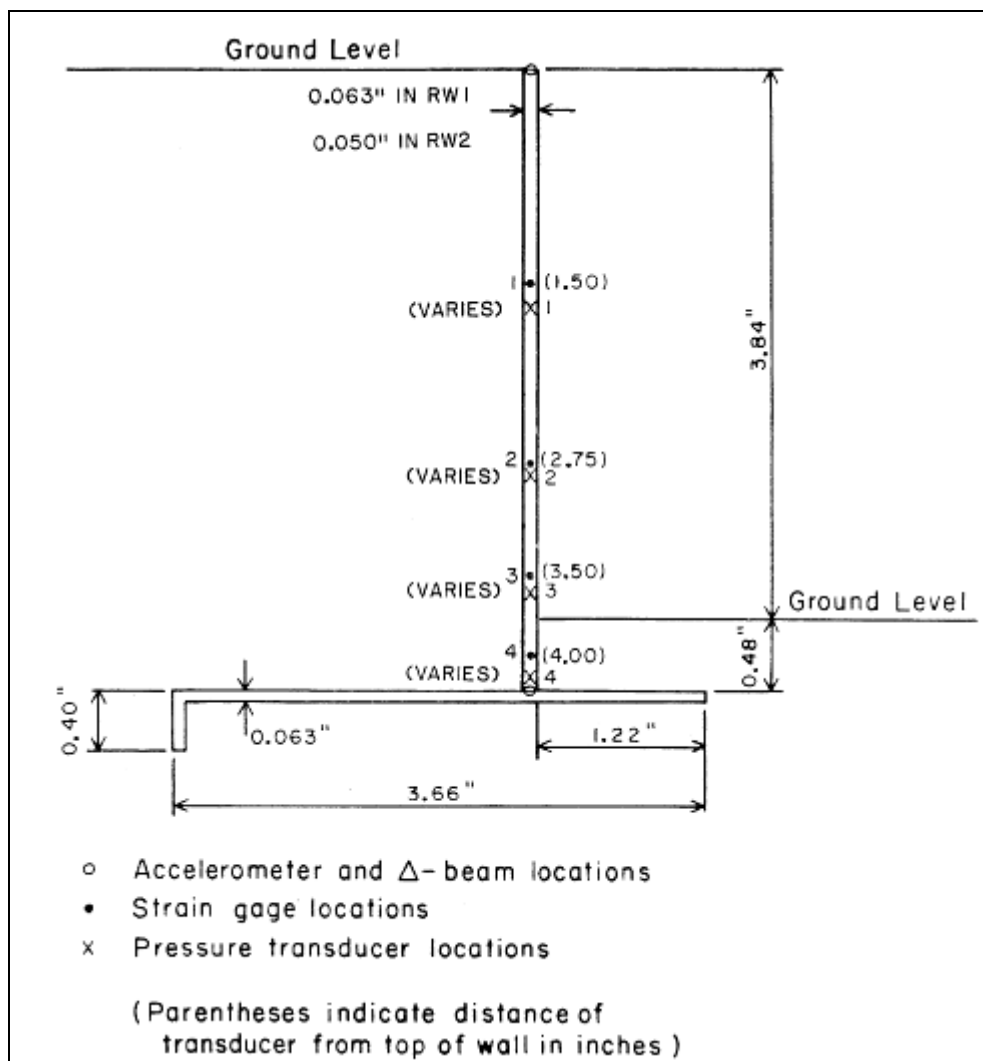


Figure 2.3.5 Model wall cross-section (Ortiz, 1982)

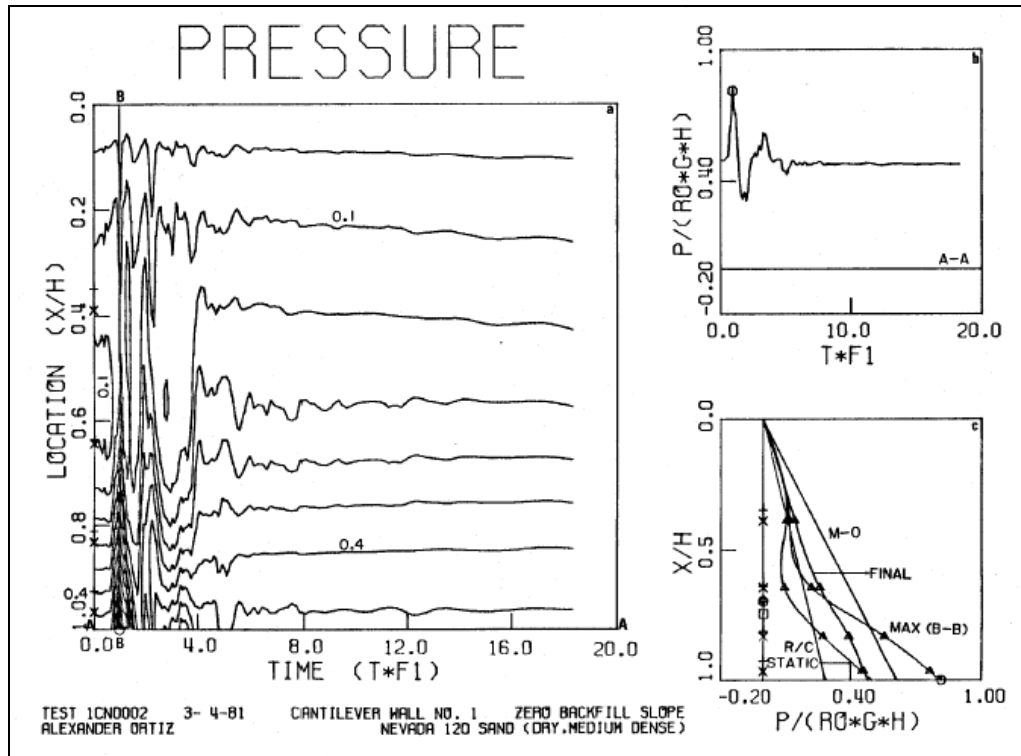


Figure 2.3.6 Record of wall pressure (Ortiz, 1982)

Sommers and Wolfe (1984) presented the results of shaking table tests. The effects of input motion on the displacement of model walls is investigated. The wall accelerations are found to be dependent on the amplitude and frequency of the input motion. On the other hand, the displacements are found to be dependent on the type of input motion.

Fukuoka and Imamura (1984) examined the seismic behaviour of retaining walls conducting model tests and using real earthquake measurements. An important conclusion indicated is that the earth pressure magnitude is determined by the total energy put into the retaining wall-soil system in one or two seconds rather than the acceleration acting at that moment.

Shaking table experiments with different modes of wall movement are used to investigate the dynamic active earth pressures on rigid retaining walls with dry cohesionless backfill by Ishibashi and Fang (1987). They made experiments using the University of Washington shaking table and retaining wall assembly for wall

movement modes : rotation about the base (RB) and rotation about the top (RT). The results are combined with those by Sherif et al (1982) and Ichihara and Matsuzawa (1973), who considered pure translation (T) and translation together with rotation about the base (RB+T) respectively.

Normalized maximum dynamic lateral earth pressures obtained from the pressure cells (shown in Figure 2.3.7) as a function of wall rotation is shown in Figure 2.3.8. The plotted values are the maximum of the measurements during vibration. It can be seen that the maximum pressures decrease rapidly with initial wall rotation and reach constant values.

The maximum lateral earth pressure distributions with different wall rotations for rotation about base are shown in Figure 2.3.9. It is stated that a very high residual stress zone near the wall base is observed since there is little soil movement at that region.

The coefficient of maximum dynamic active horizontal thrust values for RB and RT walls are plotted on Figure 2.3.10. All the points for RB mode fall within 123% and 143% of M-O values with an average of 128%. This is considered to result due to the extra high residual stress near the wall base. Figure 2.3.11 summarizes the point of application variation for different modes of wall movement.

It is indicated that at low acceleration levels, the movement and geometry of the wall is the controlling factor. Meanwhile at high acceleration levels, the vibrating portion of the thrust becomes dominant in determining the application point. Therefore the normalized height of the application point, h/H value converges to around 0.4 to 0.55 for horizontal acceleration coefficient, $k_h > 0.5$ regardless of the wall movement.

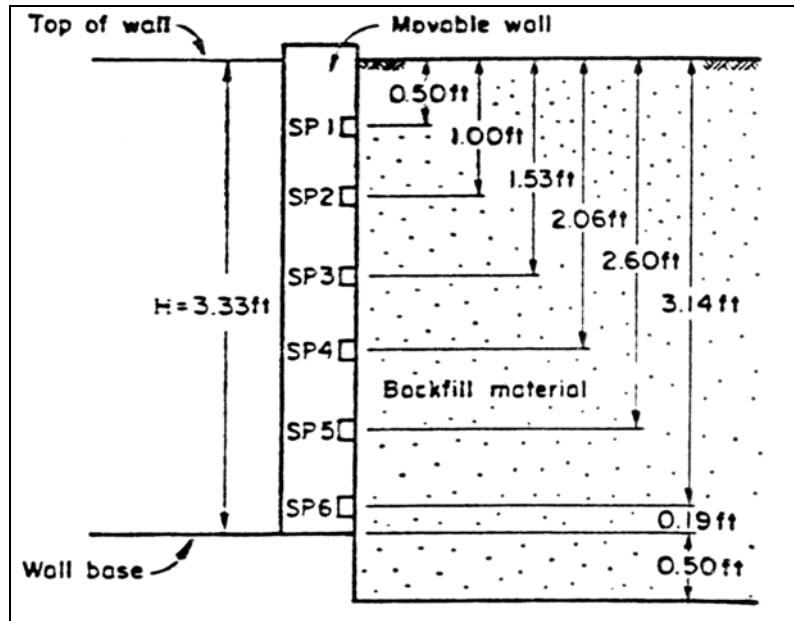


Figure 2.3.7 Locations of soil pressure transducers behind model wall (Ishibashi and Fang, 1987)

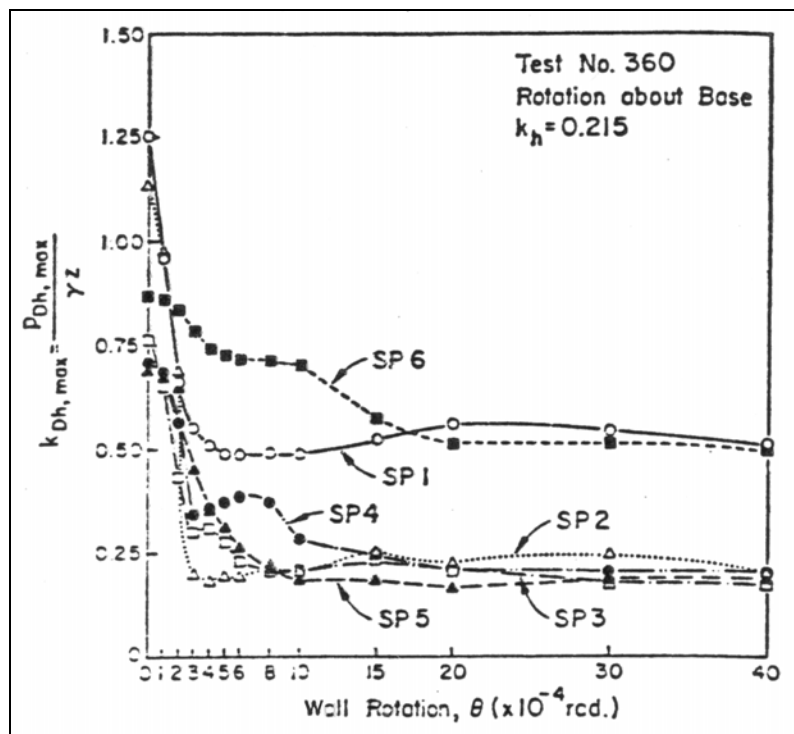


Figure 2.3.8 Change in lateral pressure with wall rotation for RB mode (Ishibashi and Fang, 1987)

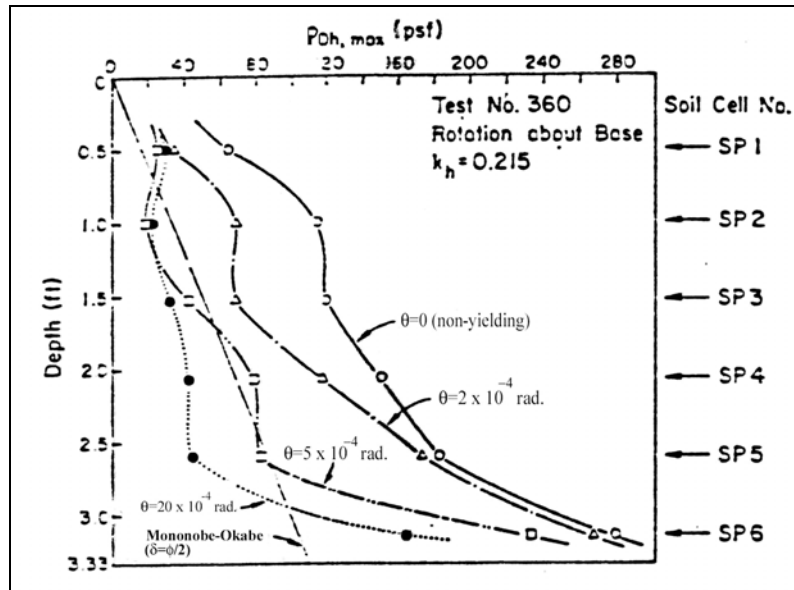


Figure 2.3.9 Distribution of maximum lateral earth pressure at different wall rotations for RB mode (Ishibashi and Fang, 1987)

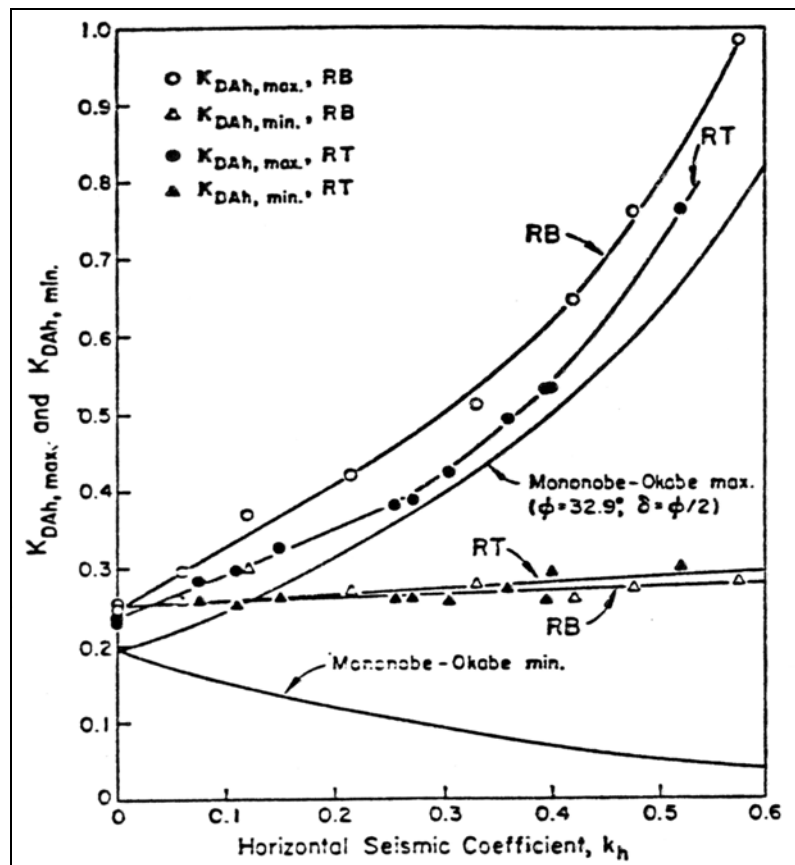


Figure 2.3.10 Coefficient of maximum dynamic active horizontal thrust (Ishibashi and Fang, 1987)

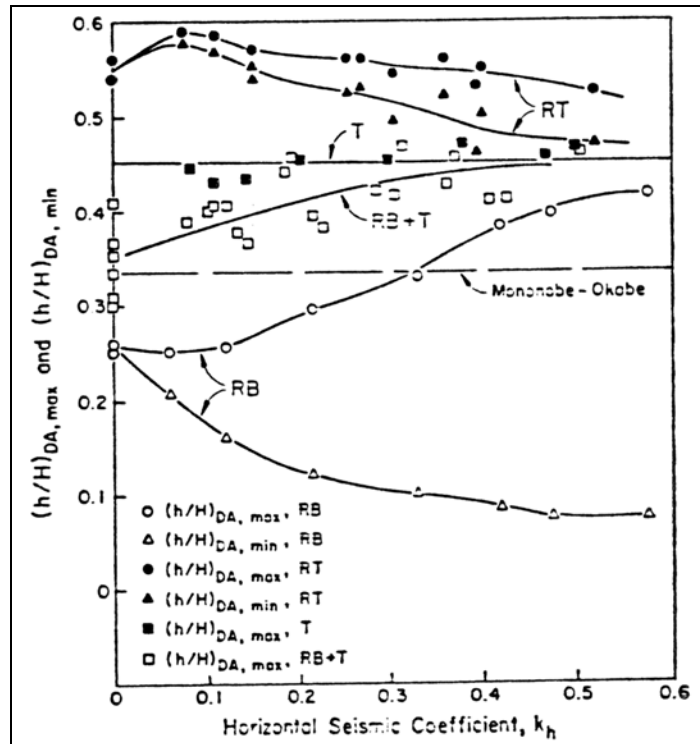


Figure 2.3.11 Point of application of dynamic thrust (Ishibashi and Fang, 1987)

Centrifuge model tests are conducted to study the seismic behaviour of gravity quay walls by Zeng (1998). A gravity wall of 8m high and 4m wide in prototype scale with both dry and saturated backfill is considered. A series of model earthquakes is applied with a gradual increase in the peak acceleration until failure is observed in the tests. Major damage included the lateral displacement, vertical settlement and tilting of the gravity wall and ground settlement in the backfill. It is concluded that for a gravity wall retaining dry backfill, the current design procedures give satisfactory results.

Madabhashi and Zeng (1998) made a numerical simulation of the centrifuge experiments by using finite element method and compared the results. An elasto-plastic material model is used for soil and interface elements are used between the wall and backfill allowing for relative displacement. It is stated that the results for the cases of both dry and saturated backfill are in good agreement with experimental data. The profile of the model wall before and after the test and deformed mesh after the analysis are shown in Figure 2.3.12.

- The measured values of the incremental seismic thrust are considerably higher than those calculated by M-O method (See Figure 2.3.15).
- The distance of the point of application to the base varies between 0.35H and 0.45H for the tests in which failure did not occur. On the other hand, the point of application shifts below 0.33H for the tests in which considerable rotation and translation was observed (See Figure 2.3.16).

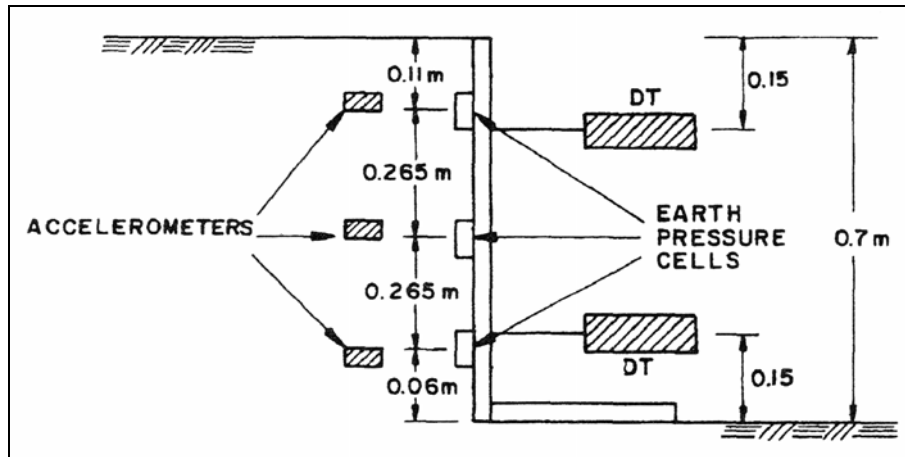


Figure 2.3.13 Model wall dimensions and instrumentation (Çalışan, 1999)

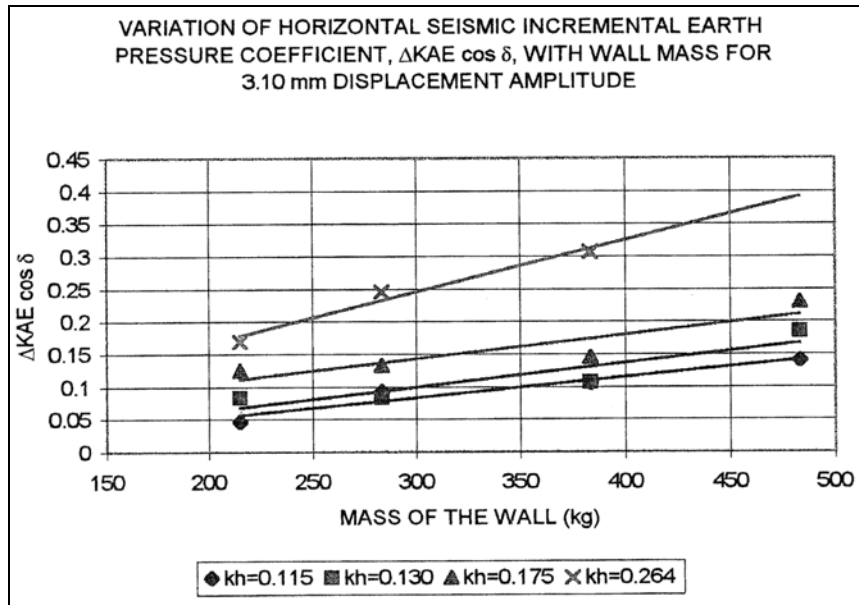


Figure 2.3.14 Variation of horizontal seismic incremental earth pressure coefficient with wall mass (Çalışan, 1999)

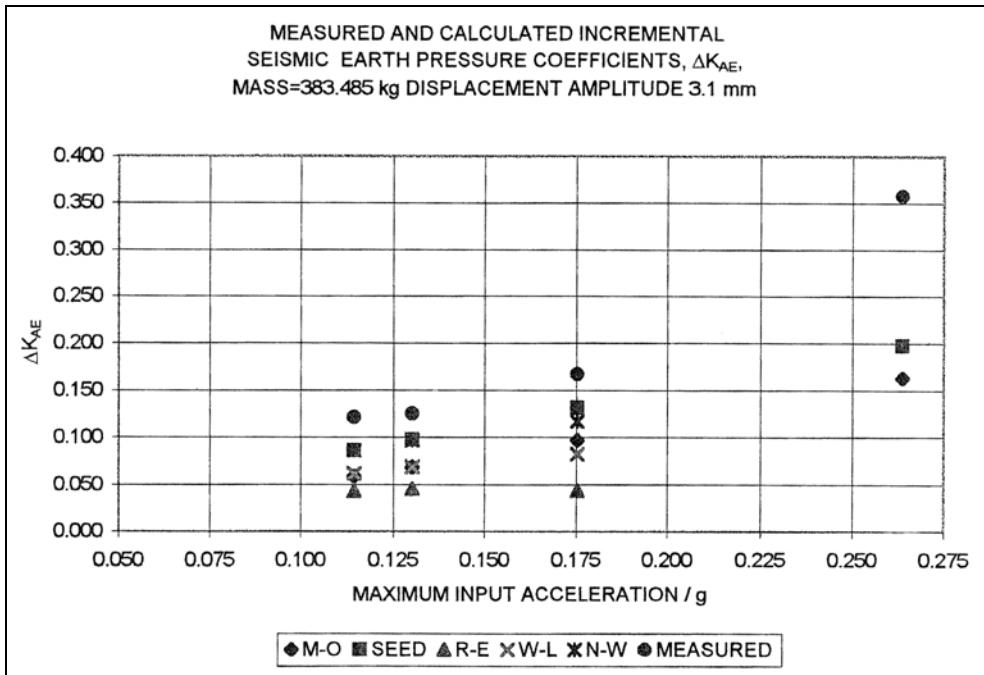


Figure 2.3.15 Incremental seismic earth pressure coefficient (Çalışan, 1999)

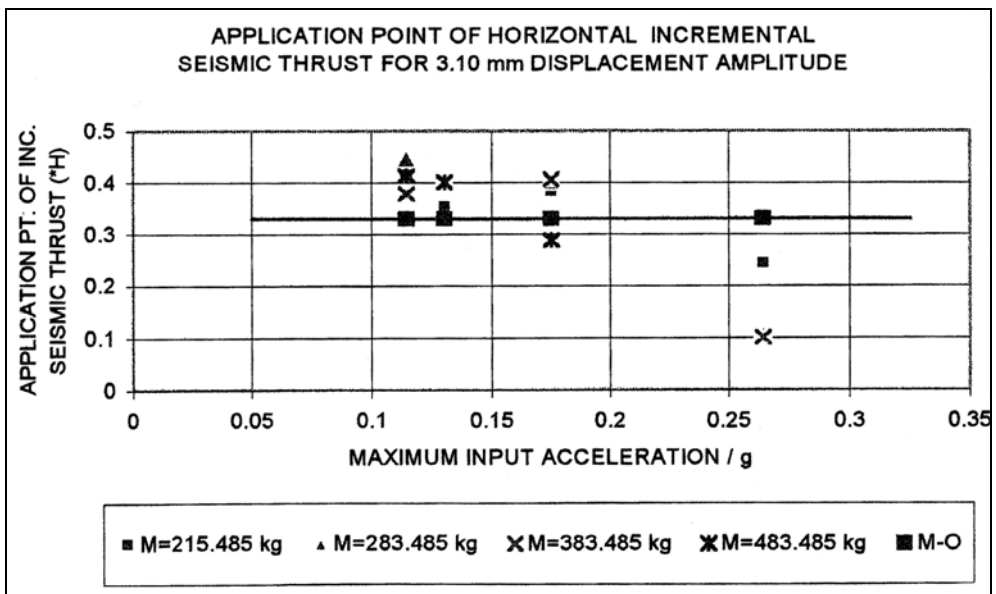


Figure 2.3.16 Application point of horizontal seismic incremental thrust (Çalışan, 1999)

CHAPTER 3

REVIEW ON THEORETICAL ASPECTS

Analyses to investigate the dynamic behaviour of retaining wall-soil systems are done by using finite element method. The finite element program ANSYS is used for this purpose. In this section, information about the material models representing the wall and soil, dynamic finite element procedures, the contact algorithm used to simulate the relative motion of the backfill and the wall are given. In addition, the verification of the program is presented by comparing the results of finite element analysis and analytical solution for one-dimensional wave propagation problem.

3.1 Material model

The retaining wall and the soil (backfill and foundation soil) are modelled by using 4-node plane-strain elements. The wall is assumed as a linear-elastic material with appropriate stiffness and mass parameters for concrete, since the stresses and the strength of the retaining wall is beyond the scope of this study. On the other hand, the soil is modelled as either linear elastic or elasto-plastic so that the non-linear stress-strain behaviour of soil may be taken into account.

3.1.1 Review on plasticity

For many materials, the stress-strain relationship is not unique (as in the linear elastic model) and many states of strain can correspond to one state of stress and vice versa. The stress-strain curve obtained from a tension test on a metal bar is shown in Fig. 3.1.1.1. The relation between stress and strain is linear for the initial

portion OA. The stress-strain relation is reversible in any unloading case from any point on OA. If the bar is loaded beyond A, subsequent unloading is also reversible but non-linear. However, there is a point B beyond which unloading is not reversible. This point is called as the yield point of the material. The points A and B can often be regarded as coincident for practical purposes. If the bar is loaded to point C and unloaded, the path CD is followed, resulting in a permanent strain represented by OD. This permanent strain is called as the plastic strain. When the material is loaded to point C, the total strain is the sum of the plastic strain, OD, and elastic strain, DE. Further loading beyond C continues until the bar fails (at point F). The stress at the point F is often called as the ultimate strength (Britto and Gunn, 1987).

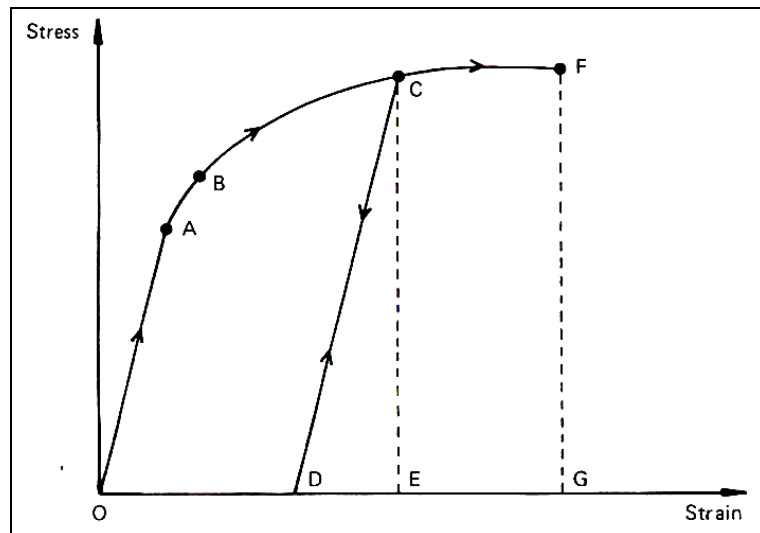


Figure 3.1.1.1 Typical stress-strain curve (after Britto and Gunn, 1987)

To model the materials having plastic behaviour, some idealisations have to be made. In such idealisations, the main features of the behaviour are identified but aspects of secondary importance are ignored.

Fig. 3.1.1.2 shows some widely used idealisations of plastic behaviour. In elastic-perfectly plastic model, the material shows linear elastic behaviour until it yields. After yielding, the material continues to deform at constant yield stress. In elastic, strain-hardening plastic model, the stress-strain curve remains linear at a reduced

slope after yielding. When only collapse loads are to be considered in a calculation, it is convenient to use rigid-plastic models in which no elastic strain exists.

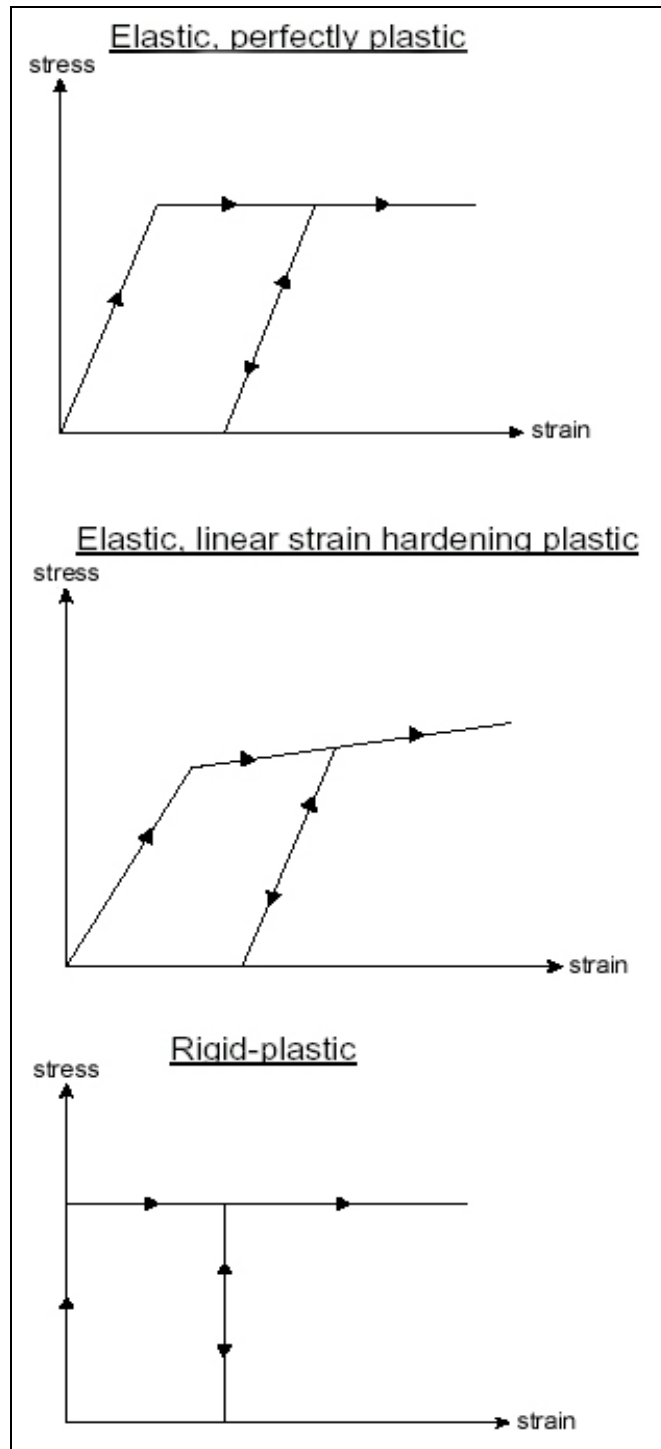


Figure 3.1.1.2 Idealisations of plastic behaviour (after Britto and Gunn, 1987)

To completely describe the stress-strain relations for an elasto-plastic material, four different criteria are required (Britto and Gunn, 1987):

- 1- A yield function : This generalises the concept of yield stress for one-dimensional loading to two or three dimensional stress states.
- 2- A relationship between the directions of the principal plastic strain increments and the principal stresses.
- 3- A hardening rule : This is the relationship between the amount of hardening and plastic strain when the material is yielding. Thus the hardening rule determines the changes in the yield surface.
- 4- A flow rule : This specifies the relative magnitudes of the incremental plastic strains when the material is yielding.

Yield function

If a material is subjected to two or three dimensional states of stress, the state of the material (elastic or plastic) depend on all the stress components (six in the fully three dimensional case). If the material is isotropic, then it's sufficient to consider only the principal stresses (σ_a , σ_b and σ_c), and generally the yield functions are expressed in terms of them (Britto and Gunn, 1987).

In general a yield function is written as:

$$f(\sigma_a, \sigma_b, \sigma_c) = 0,$$

this equation representing a surface in three-dimensional stress space. Generally yield function is written in such a way that, the negative value of the function for the current stress state indicates that the behaviour is elastic (inside the yield surface). A zero value of the function indicates that yielding takes place and

positive values which represent stress states outside the yield surface are not allowed.

Hardening rule

The hardening rule is used to define the motion (changes in size, shape and location) of the yield surface during plastic loading. Hardening rules are classified as isotropic hardening, kinematic hardening and mixed hardening. The yield surface expands uniformly in isotropic hardening, while it moves as a rigid body in stress space in kinematic hardening (See Fig. 3.1.1.3). Mixed hardening combines both of these types of hardening and permits the yield surface to expand or contract uniformly and to translate in stress space.

If the loading is monotonic, then the isotropic hardening rule is adequate to describe the material behaviour. The kinematic hardening rule is suitable for materials under cyclic and reversed type of loadings (Chen and Mizuno, 1990).

Flow rule

The flow rule defines the ratios of plastic strain increments for a yielding material at a particular stress state. It defines only the relative sizes of individual strain increments, not their absolute sizes. The following expression is used to define the flow rule :

$$\delta\epsilon^p = \delta\lambda \frac{\partial g}{\partial \sigma} \quad (3.1.1.1)$$

where $\delta\epsilon^p$ is the plastic strain increment, $\delta\lambda$ is the proportionality factor and g is the plastic potential function.

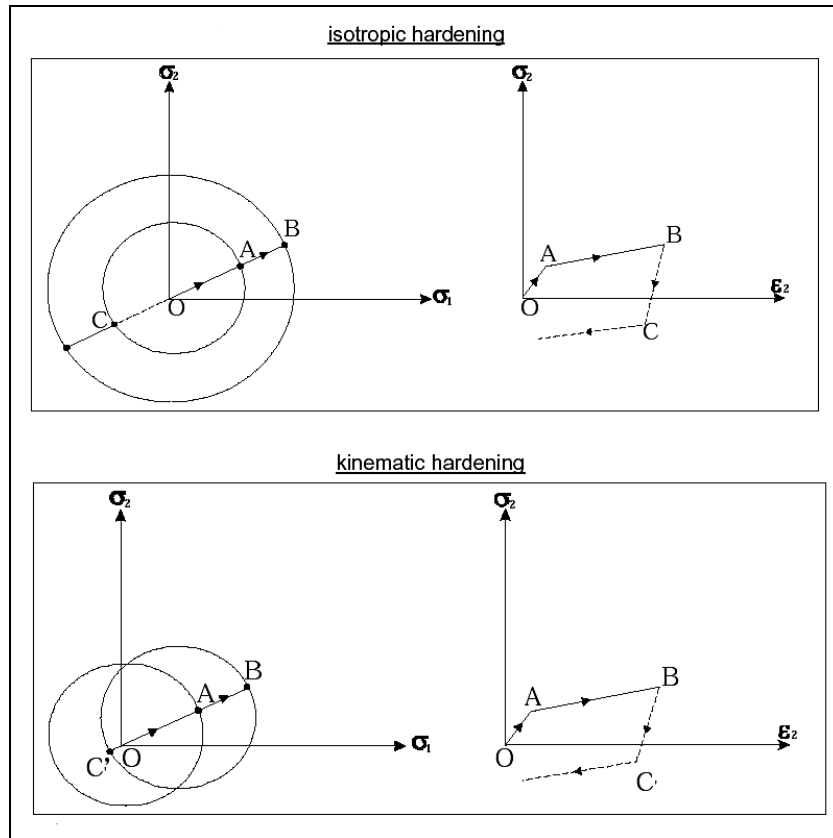


Figure 3.1.1.3 Isotropic and kinematic hardening (after Britto and Gunn, 1987)

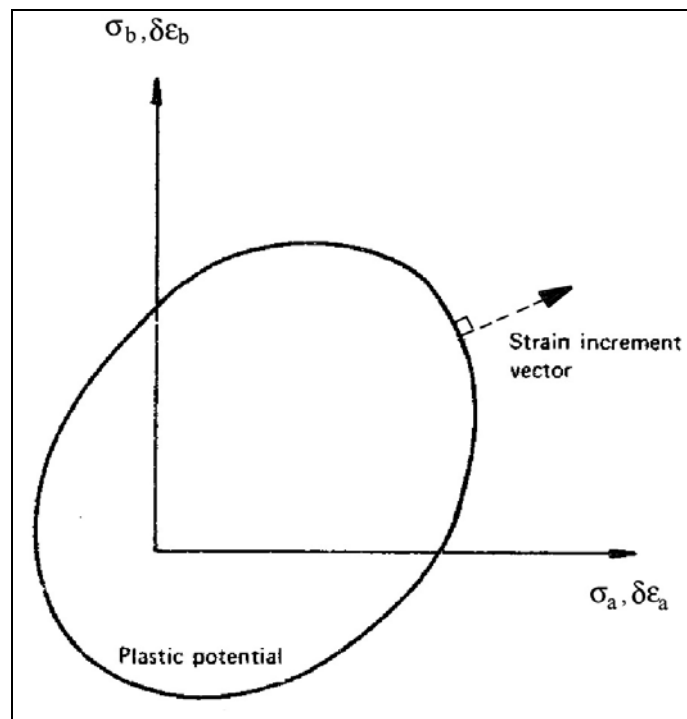


Figure 3.1.1.4 The plastic potential (after Britto and Gunn, 1987)

The plastic potential function, $g(\sigma_a, \sigma_b, \sigma_c) = 0$ defines such a surface in principal stress space that, the plastic strain increment vectors are normal to this surface (See Fig. 3.1.1.4). The yield function can be used as a potential function for many materials. This is called as the normality condition or associated flow rule. If a potential function different than the yield function is used, then it is called as non-associated flow.

3.1.2 Drucker-Prager material model

An elastic-perfectly plastic material model using Drucker-Prager yield criterion with either associated or nonassociated flow rule is used to represent soil in the elasto-plastic analyses. A brief information on the implementation of the model is given in this section based on ANSYS Theory Reference. The notations used in this section are given in Table 3.1.

The yield criterion (yield function) is expressed as:

$$F = \sigma_e - \sigma_y = 0 \quad (3.1.2.1)$$

The equivalent stress and material yield parameters σ_e and σ_y are expressed as:

$$\sigma_e = 3\beta\sigma_m + \left[\frac{1}{2} \{S\}^T [M] \{S\} \right]^{\frac{1}{2}} \quad (3.1.2.2)$$

$$\sigma_y = \frac{6c \cos \phi}{\sqrt{3}(3 - \sin \phi)} \quad (3.1.2.3)$$

Table 3.1 Notations used in material model theory

Variable	Definition
$\{\varepsilon^{el}\}$	elastic strain vector
$\{\varepsilon^{pl}\}$	plastic strain vector
$\{\varepsilon^{tr}\}$	trial strain vector
$\{\sigma\}$	Stress vector
σ_e	equivalent stress
σ_y	material yield parameter
σ_m	mean or hydrostatic stress
λ	plastic multiplier
[D]	stress-strain matrix
E_T	tangent modulus
F	yield criterion (yield function)
Q	plastic potential function
$\{S\}$	deviatoric stress vector
c	cohesion of material
ϕ	angle of friction for material

The variables in Equation 3.1.2.2 are defined below:

$$\beta = \frac{2 \sin \phi}{\sqrt{3}(3 - \sin \phi)} \quad (3.1.2.4)$$

$$\sigma_m = \frac{(\sigma_x + \sigma_y + \sigma_z)}{3} \quad (3.1.2.5)$$

$$\{S\} = \{\sigma\} - \sigma_m [1 \ 1 \ 1 \ 0 \ 0 \ 0]^T \quad (3.1.2.6)$$

$$[M] = \begin{bmatrix} 1 & 0 & 0 & 0 & 0 & 0 \\ 0 & 1 & 0 & 0 & 0 & 0 \\ 0 & 0 & 1 & 0 & 0 & 0 \\ 0 & 0 & 0 & 2 & 0 & 0 \\ 0 & 0 & 0 & 0 & 2 & 0 \\ 0 & 0 & 0 & 0 & 0 & 2 \end{bmatrix} \quad (3.1.2.7)$$

This yield surface (given by Equation 3.1.2.1) is a circular cone chosen such that it corresponds to the outer aspices of the hexagonal Mohr-Coulomb yield surface as shown in Figure 3.1.2.1.

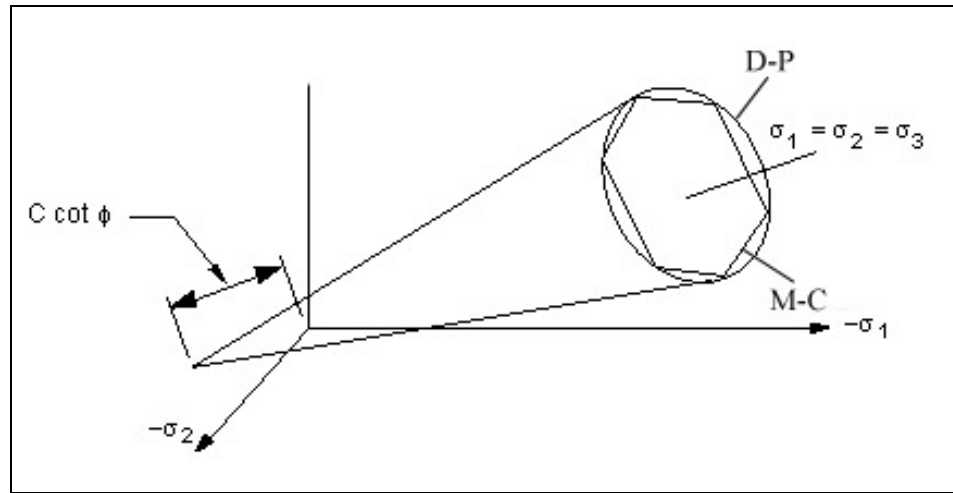


Figure 3.1.2.1 Yield surfaces of Mohr-Coulomb and Drucker-Prager yield criteria in 3-D principal stress space (after ANSYS Theory Reference)

The flow rule determines the direction of plastic straining and is given as:

$$\{d\varepsilon^{pl}\} = \lambda \left\{ \frac{\partial Q}{\partial \sigma} \right\} \quad (3.1.2.8)$$

Equation 3.1.2.1 can be differentiated so that the consistency condition is:

$$dF = \left\{ \frac{\partial F}{\partial \sigma} \right\}^T [M] \{d\sigma\} = 0 \quad (3.1.2.9)$$

The stress increment can be computed by the elastic stress-strain relation:

$$\{\mathbf{d}\boldsymbol{\sigma}\} = [\mathbf{D}]\{\mathbf{d}\boldsymbol{\varepsilon}^{\text{el}}\} \quad (3.1.2.10)$$

and

$$\{\mathbf{d}\boldsymbol{\varepsilon}^{\text{el}}\} = \{\mathbf{d}\boldsymbol{\varepsilon}\} - \{\mathbf{d}\boldsymbol{\varepsilon}^{\text{pl}}\} \quad (3.1.2.11)$$

since the total strain increment is composed of an elastic and plastic part. Substituting Equations 3.1.2.10, 3.1.2.11 and 3.1.2.8 into Equation 3.1.2.9 in order, one can obtain the plastic multiplier as:

$$\lambda = \frac{\left\{ \frac{\partial \mathbf{F}}{\partial \boldsymbol{\sigma}} \right\}^{\text{T}} [\mathbf{M}][\mathbf{D}]\{\mathbf{d}\boldsymbol{\varepsilon}\}}{-\left\{ \frac{\partial \mathbf{F}}{\partial \boldsymbol{\sigma}} \right\}^{\text{T}} [\mathbf{M}][\mathbf{D}]\left\{ \frac{\partial \mathbf{Q}}{\partial \boldsymbol{\sigma}} \right\}} \quad (3.1.2.12)$$

so that the size of the plastic increment is related to the total strain increment, the current stress state and the forms of yield and potential surfaces. The plastic strain increment is then computed by using Equation 3.1.2.8.

$\left\{ \frac{\partial \mathbf{F}}{\partial \boldsymbol{\sigma}} \right\}$ can be computed as:

$$\left\{ \frac{\partial \mathbf{F}}{\partial \boldsymbol{\sigma}} \right\} = \beta [1 \ 1 \ 1 \ 0 \ 0 \ 0]^{\text{T}} + \frac{1}{\left[\frac{1}{2} \{\mathbf{S}\}^{\text{T}} [\mathbf{M}] \{\mathbf{S}\} \right]^{\frac{1}{2}}} \{\mathbf{S}\} \quad (3.1.2.13)$$

$\left\{ \frac{\partial Q}{\partial \sigma} \right\}$ can similarly be computed, however β is calculated using the dilatancy angle, ψ instead of friction angle, ϕ . There will be volumetric expansion with plastic straining when $\psi > 0$. No volumetric expansion of the material occurs when $\psi = 0$.

An Euler backward scheme is used to enforce the consistency condition given by Equation 3.1.2.9 which ensures the updated stresses and strains are on the yield surface. The implementation algorithm is summarized below:

1- The material parameter σ_y is calculated for the current time step.

2- The stresses are computed based on the trial strain $\{\varepsilon^{tr}\}$, that is the total strain minus the plastic strain of the previous time step:

$$\{\varepsilon_n^{tr}\} = \{\varepsilon_n\} - \{\varepsilon_{n-1}^{pl}\} \quad (3.1.2.14)$$

$$\{\sigma^{tr}\} = [D]\{\varepsilon^{tr}\} \quad (3.1.2.15)$$

3- The equivalent stress σ_e is calculated by Equation 3.1.2.2. If σ_e is less than σ_y , the material is in elastic state and no plastic strain increment is computed.

4- If $\sigma_e > \sigma_y$, the plastic multiplier, λ is calculated from Equation 3.1.2.12 by using a Newton-Raphson iteration procedure.

5- $\{d\varepsilon^{pl}\}$ is calculated by Equation 3.1.2.8.

6- The current plastic strain is updated:

$$\{\varepsilon_n^{pl}\} = \{\varepsilon_{n-1}^{pl}\} + \{d\varepsilon^{pl}\} \quad (3.1.2.16)$$

The elastic strain is computed:

$$\{\varepsilon^{el}\} = \{\varepsilon^{tr}\} - \{d\varepsilon^{pl}\} \quad (3.1.2.17)$$

and the stress vector is:

$$\{\sigma\} = [D]\{\varepsilon^{el}\} \quad (3.1.2.18)$$

3.2 Dynamic finite element analysis

3.2.1 Review on time history analysis

The equation of motion for a single degree of freedom system can be written as :

$$m\ddot{u} + c\dot{u} + ku = P(t) \quad (3.2.1.1)$$

where; m = mass

c = viscous damping constant

k = spring constant

P = applied external load at time t

u = displacement at time t

$\dot{u} = \frac{du}{dt}$ = velocity at time t

$\ddot{u} = \frac{d^2u}{dt^2}$ = acceleration at time t

Similarly the equations of equilibrium governing the dynamic response of a system of finite elements can be written in matrix form as (Bathe, 1996):

$$[M]\{\ddot{u}\} + [C]\{\dot{u}\} + [K]\{u\} = \{P\} \quad (3.2.1.2)$$

where; $[M]$ = mass matrix of the system

$[C]$ = damping matrix of the system

$[K]$ = stiffness matrix of the system

$\{\ddot{u}\}$ = nodal acc. vector

$\{\dot{u}\}$ = nodal velocity vector

$\{u\}$ = nodal displacement vector

$\{P\}$ = applied load vector

which represent a system of linear differential equations of second order.

Step by step methods are generally used for the solution of 3.2.1.2 in finite element method. Newmark Beta method is one of the most commonly used step by step methods which is employed in the finite element program ANSYS.

There are many different step by step methods (eg. central difference method, the Houbolt method, the Wilson method, the Newmark method as stated in Bathe, 1996) in all of which the loading and the response history of the system are divided into small time intervals (steps). The response of the system at each interval is calculated from the initial conditions at the beginning of the step and the loading during that step. Therefore, each step is assumed to be an independent analysis in which the acceleration, velocity and displacement vectors are obtained at the end of the time interval.

Step by step methods may be classified into two categories as:

1- Explicit methods :

In explicit methods, the unknown response values at the end of a step are totally dependent on and are calculated from the quantities obtained in the previous step or steps, so the analysis proceeds directly from one step to the next.

2- Implicit methods :

In implicit methods, the equations giving the unknown values of a given step include one or more values corresponding to the same step; thus an iterative procedure should be carried out to solve the equations and find the response values at the end of the step. It is often desirable to convert an implicit method to an explicit form to make the solutions faster.

Newmark Beta Methods

In the Newmark formulation, the final velocity and displacement values are expressed as follows :

$$\dot{u}_1 = \dot{u}_0 + (1 - \delta)h\ddot{u}_0 + \delta h\ddot{u}_1 \quad (3.2.1.3)$$

$$u_1 = u_0 + h\dot{u}_0 + \left(\frac{1}{2} - \alpha\right)h^2\ddot{u}_0 + \alpha h^2\ddot{u}_1 \quad (3.2.1.4)$$

where h is the size of the time step. The factor δ provides a linearly varying weighting of the influence of the initial and the final accelerations on the change of the velocity; and the factor α provides for weighting of the influence of these initial and final accelerations to the change of the displacement.

Taking $\delta = 1/2$ and $\alpha = 1/4$ in Equations 3.2.1.3 and 3.2.1.4 is referred as the constant average acceleration method in which the acceleration is assumed to be constant during the time step as the average of the initial and final accelerations. The constant acceleration method is depicted in Figure 3.2.1.1.

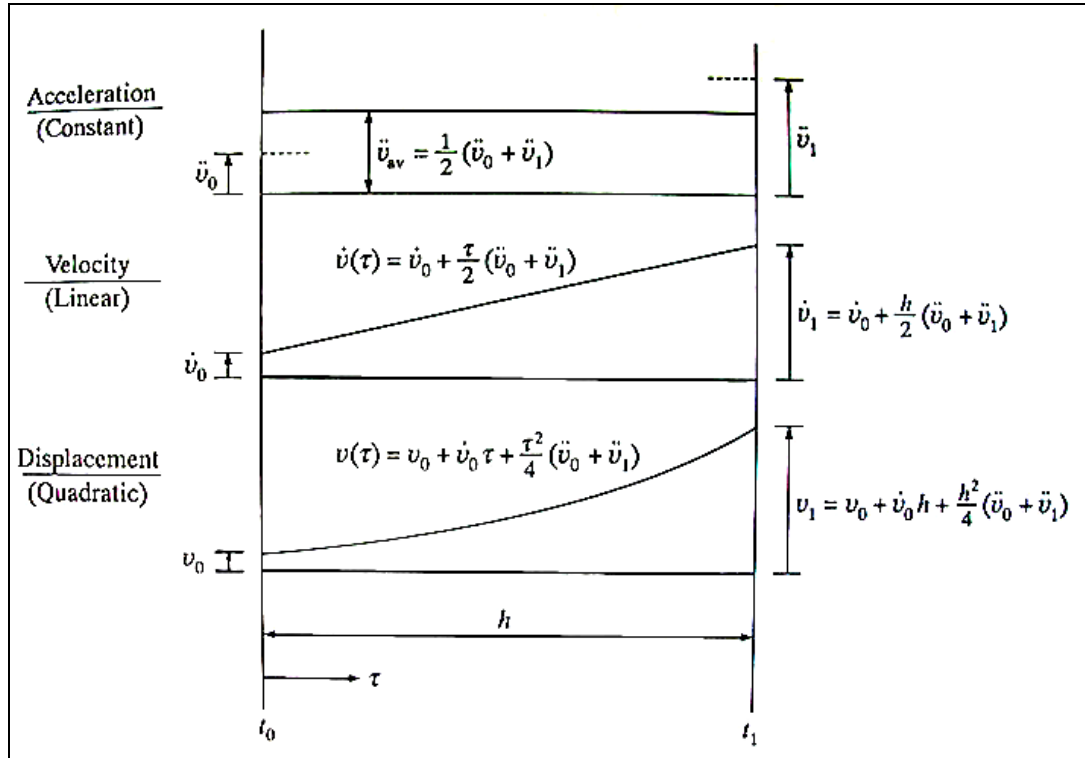


Figure 3.2.1.1 Constant acceleration method
(Newmark, 1959 (after Clough and Penzien, 1993))

Implementation in ANSYS

The implementation of the Newmark method in the program is summarized briefly below based on ANSYS Theory Reference.

Equations 3.2.1.3 and 3.2.1.4 can be rearranged such that:

$$\{\ddot{u}_{n+1}\} = a_0 (\{u_{n+1}\} - \{u_n\}) - a_2 \{\dot{u}_n\} - a_3 \{\ddot{u}_n\} \quad (3.2.1.5)$$

$$\{\ddot{u}_{n+1}\} = \{\dot{u}_n\} + a_6 \{\ddot{u}_n\} + a_7 \{\ddot{u}_{n+1}\} \quad (3.2.1.6)$$

where; $a_0 = \frac{1}{\alpha h^2}$ $a_1 = \frac{\delta}{\alpha h}$ $a_2 = \frac{1}{\alpha h}$ $a_3 = \frac{1}{2\alpha} - 1$

$$a_4 = \frac{\delta}{\alpha} - 1 \quad a_5 = \frac{h}{2} \left(\frac{\delta}{\alpha} - 2 \right) \quad a_6 = h(1 - \delta) \quad a_7 = \delta h$$

The equations of $\{\ddot{u}_{n+1}\}$ and $\{\dot{u}_{n+1}\}$ can be expressed only in terms of the unknown displacement vector $\{u_{n+1}\}$ by substituting Equation 3.2.1.5 into 3.2.1.6. The equations formed are then combined with Equation 3.2.1.2 to form:

$$\begin{pmatrix} a_0[M] + \\ a_1[C] + \\ [K] \end{pmatrix} \{u_{n+1}\} = \begin{pmatrix} \{P_{n+1}\} + \\ [M](a_0\{u_n\} + a_2\{\dot{u}_n\} + a_3\{\ddot{u}_n\}) + \\ [C](a_1\{u_n\} + a_4\{\dot{u}\} + a_5\{\ddot{u}_n\}) \end{pmatrix} \quad (3.2.1.7)$$

so that the solution for displacements at time t_{n+1} , $\{u_{n+1}\}$ can be obtained. The velocity and acceleration values at t_{n+1} can then be obtained by Equations 3.2.1.5 and 3.2.1.6.

It is stated by Zienkiewicz (1977) that the numerical solution of Equation 3.2.1.2 by Equations 3.2.1.5 and 3.2.1.6 is unconditionally stable for:

$$\alpha \geq \frac{1}{4}(1 + \gamma)^2, \delta \geq \frac{1}{2}, \frac{1}{2} + \delta + \alpha > 0.$$

In ANSYS, the Newmark parameters are related to an amplitude decay factor, γ as:

$$\alpha = \frac{1}{4}(1 + \gamma)^2, \delta = \frac{1}{2} + \gamma \quad (3.2.1.8)$$

When $\gamma \geq 0$, the solution will be unconditionally stable. Assuming $\gamma=0$ the Newmark method becomes the constant average acceleration method. Results from the constant average acceleration method do not show any numerical damping in terms of displacement errors. If other sources of damping are not present, the lack of numerical damping can be undesirable in that the higher frequencies of the system can produce unacceptable levels of numerical noise (Zienkiewicz, 1977). So usually a certain level of numerical damping is desired and γ is given a small value. In this study, γ is assumed as 0.005 which is the default value suggested in the program.

About integration time step

The accuracy of the solution depends on the time step size. The accuracy gets higher as the time step size decreases. A time step that is too large leads to error that affects the response of the higher modes of the system. A time step too small will lead to time-consuming analyses and large output data. Therefore an optimum time step should be chosen considering the following statements:

1- The time step should be small enough to resolve the response (motion) of the system. It has been found that reasonably accurate results are obtained using approximately twenty points for cycle of the highest frequency, f_{\max} . Hence the integration time step (ITS) is: $ITS=1/(20f_{\max})$.

2- The time step should be small enough to resolve the loading function so that the changes in loads can be followed sufficiently.

3- For wave-propagation problems, the time step should be small enough to capture the wave as it travels through the elements.

ANSYS has the option of automatic time stepping so that the time step is adjusted during the solution based on the response frequency and the nonlinearity effects. Automatic time stepping or time step optimization is used in this study such that the time step variation is bounded between the 1/20 and 1/2000 of the ground motion period (the time step can be reduced to 1/2000 if necessary but can not exceed 1/20 of the period of the ground motion) for greater accuracy.

3.2.2 Damping

Rayleigh damping is one of the most commonly used methods in transient finite element analyses. According to Rayleigh damping, the damping matrix, [C] in Equation 3.2.1.2 is assumed as a combination of the mass and stiffness matrices as:

$$[C] = \alpha[M] + \beta[K] \quad (3.2.2.1)$$

Rayleigh damping leads to the following relation between damping ratio and frequency (Clough and Penzien, 1993):

$$\xi_n = \frac{\alpha}{2\omega_n} + \frac{\beta\omega_n}{2} \quad (3.2.2.2)$$

where ξ_n is the damping ratio for a particular mode of vibration, n and ω_n is the natural circular frequency of mode n . The damping factors α and β can be obtained by a pair of simultaneous equations using two damping ratios ξ_m and ξ_n with corresponding frequencies ω_m and ω_n . It is commonly assumed that the sum of the α and β terms is nearly constant over a range of frequencies as shown in Figure 3.2.2.1.

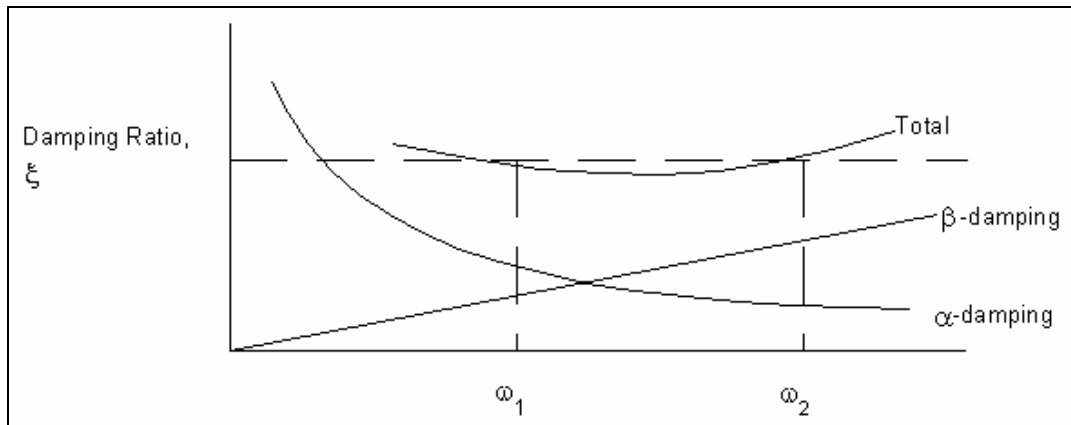


Figure 3.2.2.1 Damping ratio for Rayleigh damping
(after ANSYS Theory Reference)

3.2.3 Absorbing boundaries

In static analyses, either displacements or tractions are applied to the boundaries of the finite element model at some distance from the region of interest. However, such boundary conditions lead to the reflection of the waves propagating outward.

The viscous boundaries suggested by Lysmer and Kuhlemeyer (1969) are generally used in time-domain finite element analyses to absorb the energy of the outward propagating waves. The method suggests the use of dashpot elements in normal and shear directions at the boundaries. The dashpot constants in the normal and shear directions are taken such that the tractions provided by the dashpots are:

$$t_n = -\rho C_p V_n, \quad t_s = -\rho C_s V_s \quad (3.2.3.1)$$

where ρ is the density of the material, C_p and C_s are compression and shear wave velocities respectively, V_n and V_s are the velocities in the normal and shear directions at the boundary.

An alternative to this approach (as stated in FLAC user manual by Itasca Inc.) is to connect the boundaries to a shear beam (that simulates the free-field motion) by the dashpots, hence to satisfy the free-field conditions at the boundaries of the model. The left and right boundaries are connected to shear beams by vertical and horizontal dashpots with appropriate parameters based on Equations 3.2.3.1 in this study.

3.2.4 Verification by 1-D wave propagation problem

The finite element analysis results are verified for one-dimensional wave propagation. For this purpose, a model is established and analysed by ANSYS and SHAKE91 which is a computer program for site response analysis based on 1-D wave propagation theory (Idriss and Sun, 1992) and the results are compared.

The considered model is summarized below:

- 5m deep soil deposit underlain by a rigid base, $H=5\text{m}$.
- The soil parameters are:
 Elasticity modulus (E) = 100 Mpa
 Poisson's ratio (ν) = 0.33
 Damping ratio (ξ) = 0.1

Unit weight (γ) = 20 kN/m³

- A sinusoidal acceleration time history with the following properties is applied to the base:

Duration (t) = 4 sec.

Peak acceleration (acc_{max}) = 0.2 g

Period of the motion (T_m) = 0.2 sec.

ANSYS model and analysis

The finite element model used in the analysis is shown in Figure 3.2.4.1. 4-node plane strain elements of 0.5m edge size are used to represent soil. The width of the model is taken as 5 times the height. Dashpots are used to connect the left and right side boundaries to shear beams to satisfy free-field conditions.

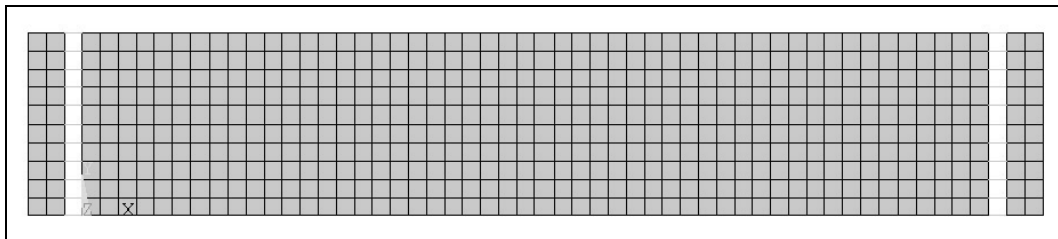


Figure 3.2.4.1 Finite element model for verification

Comparison of the results

Figure 3.2.4.2 shows the results obtained from ANSYS and SHAKE91 analyses. It can be seen that the results are in very good agreement and the finite element solution is successful for the wave propagation problem.

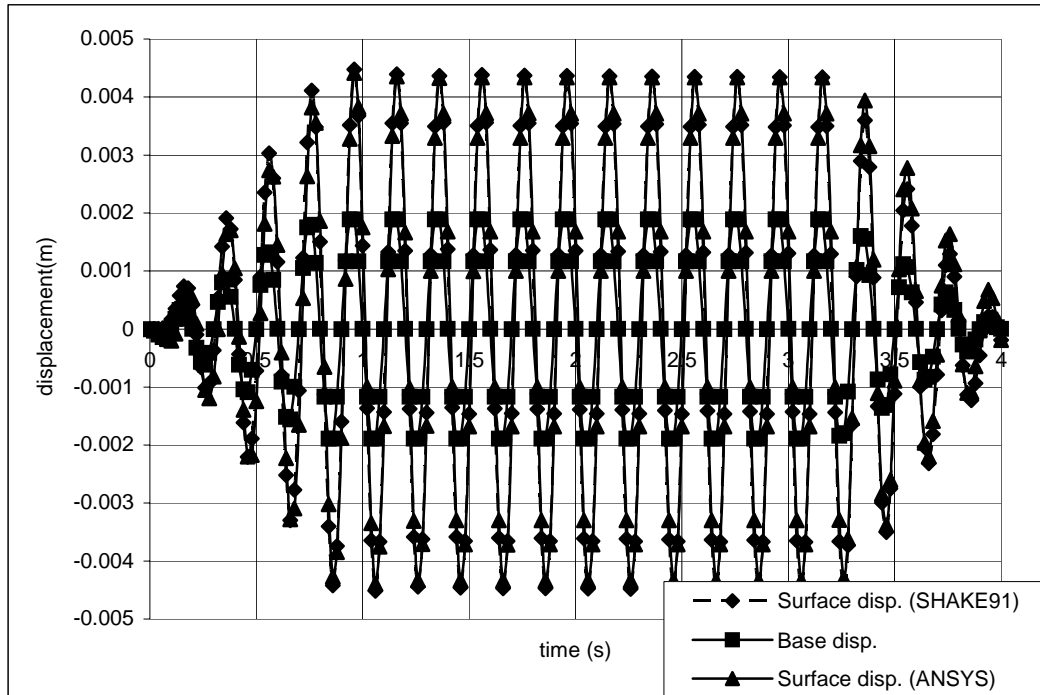


Figure 3.2.4.2 Comparison of the result of ANSYS and SHAKE91

3.2.5 About contact model

The interface between the structure and soil is of major concern in numerical computations including soil-structure interaction due to the very different stiffness and strength properties of the soil and structure. Simulating the relative motion (sliding+gap) of the soil to the structure in a correct way by considering the interaction (e.g. friction) between is essential for a realistic analysis.

There are two conventional approaches to soil-structure interaction problems:

- Using interface elements between soil and structure: Interface elements with either elastic or elasto-plastic behaviour are modelled between the associated nodes of the structure and soil to simulate the relative sliding and/or gap. This approximation can be referred as node-to-node contact.

- Assigning same degree of freedom in one direction only, hence allowing the relative displacements in the other directions. This approximation assumes smooth surfaces between the wall and structure.

The use of node-to-node contact models is reasonable for problems involving small relative sliding and deflections (rotations) of the surfaces (ANSYS Theory Reference).

A rather new approximation, surface-to-surface contact model is used in this study. In this model, the behaviour of the contact surfaces (which are two separate bodies) is determined by a specified contact algorithm. Unlike the node-to-node contact models, the contacting components need not have a compatible mesh and large deformation and large relative sliding are allowed. A brief summary about the contact model used in the study is given below based on ANSYS Theory Reference.

The contact model and algorithm

In studying the contact between two bodies, the surface of one body is taken as a contact surface and the surface of the other body as a target surface. The contact and target surfaces constitute a contact pair.

Shear stress between the surfaces are calculated according to Coulomb's law of friction. The two contacting surfaces can carry shear stresses up to a certain magnitude across their interface before they start sliding relative to each other. This state is referred as sticking. The Coulomb friction model is defined as:

$$\tau_{lim} = \mu P + c \quad (3.2.5.1)$$

$$|\tau| \leq \tau_{lim} \quad (3.2.5.2)$$

where; τ_{lim} = limit shear stress

τ = shear stress on contact

μ = coefficient of friction

P = contact normal pressure

c = contact cohesion

Once the shear stress exceed τ_{lim} , the contact and target surfaces slide relative to each other. This state is referred as sliding. The sticking/sliding calculations determine when a point transitions from sticking to sliding or vice versa. Figure 3.2.5.1 illustrates the friction model.

In pure-penalty contact algorithm, the contact pressure is given as:

$$P = \begin{cases} 0 & \text{if } u_n > 0 \\ K_n u_n & \text{if } u_n \leq 0 \end{cases} \quad (3.2.5.3)$$

where; K_n = contact normal stiffness

u_n = contact gap size

The main drawback of this algorithm is that the amount of penetration between the surfaces depends on the normal stiffness. Higher stiffness values decrease the amount of penetration, but can lead to ill-conditioning of the global stiffness matrix and to convergence difficulties.

The augmented Lagrangian method is an alternative to pure-penalty method. It is an iteration series of penalty updates to find the Lagrange multipliers (contact pressures). This method usually leads to better conditioning and is less sensitive to the magnitude of the contact stiffness value. In this method, the contact pressure is defined by:

$$P = \begin{cases} 0 & \text{if } u_n > 0 \\ K_n u_n + \lambda_{i+1} & \text{if } u_n \leq 0 \end{cases} \quad (3.2.5.4)$$

where,

$$\lambda_{i+1} = \begin{cases} \lambda_i + K_n u_n & \text{if } |u_n| > \varepsilon \\ \lambda_i & \text{if } |u_n| < \varepsilon \end{cases} \quad (3.2.5.5)$$

where; λ_i = Lagrange multiplier component at iteration i
 ε = tolerance of compatibility

The tangential contact stress is obtained by Coulomb's law:

$$\tau_t = \begin{cases} K_t u_t & \text{if } \tau_t - \mu P < 0 \text{ (sticking)} \\ \mu K_n u_n & \text{if } \tau_t - \mu P = 0 \text{ (sliding)} \end{cases} \quad (3.2.5.6)$$

where; K_t = tangential contact stiffness
 u_t = contact slip distance in tangential direction

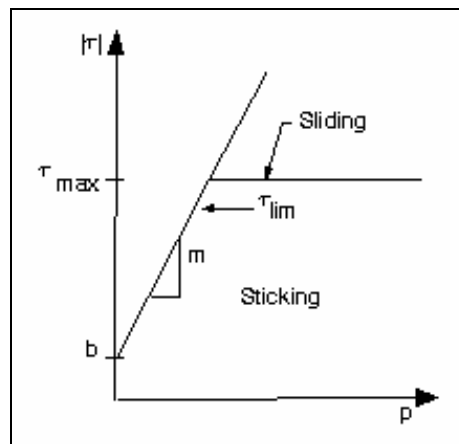


Figure 3.2.5.1 Contact friction model
(after ANSYS Theory Reference)

3.3 Linear quadrilateral plane-strain element

The soil and the wall are represented by 4-node quadrilateral plane-strain elements. Isoparametric formulation in which the displacements are expressed in terms of natural coordinates is used in the generation of the element matrices.

Figure 3.3.1 shows a 4-node quadrilateral element that is transformed into a square element in natural coordinates for the formulations. The element has 2 degrees of freedom at each node: in the directions of the x and y axes of the global coordinate system.

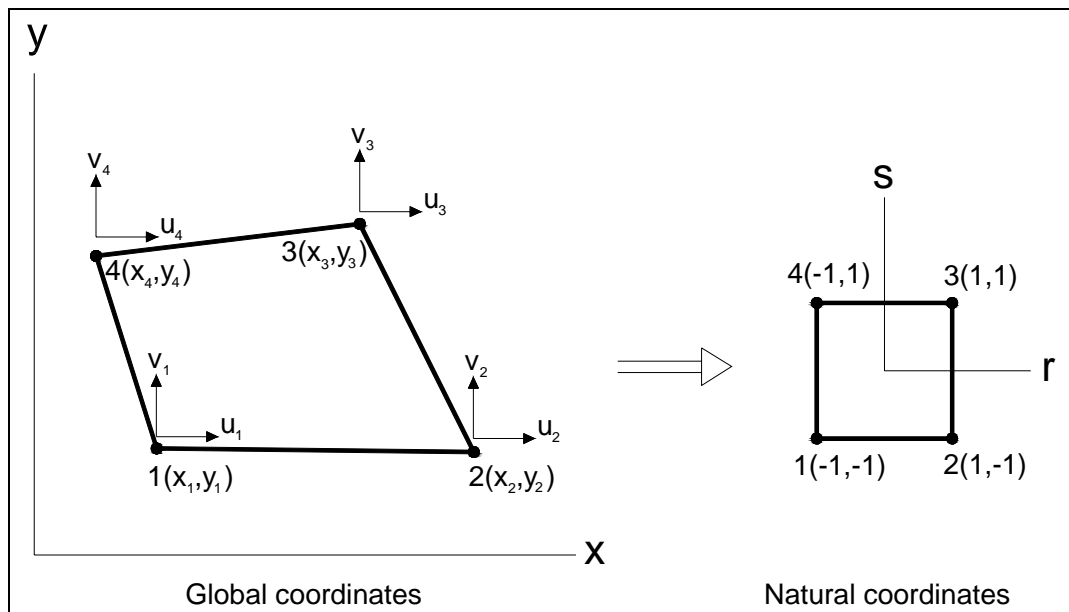


Figure 3.3.1 4-node quadrilateral plane element

Although the displacements are expressed in terms of natural coordinates, they must be differentiated with respect to global coordinates x and y, hence a transformation matrix called [J] must be used. In addition, the integrations must be done numerically rather than analytical when the elements are nonrectangular (Cook et al, 1989).

The coordinates and the displacements are interpolated from the values at the nodes by using the same shape functions, hence the term “isoparametric” is used for the formulation.

The coordinates x and y are calculated from the nodal coordinates as:

$$x = \sum_{i=1}^4 N_i x_i \quad \text{and} \quad y = \sum_{i=1}^4 N_i y_i \quad (3.3.1)$$

where the shape functions N_i are:

$$\begin{aligned} N_1 &= \frac{1}{4}(1-r)(1-s) & N_2 &= \frac{1}{4}(1+r)(1-s) \\ N_3 &= \frac{1}{4}(1+r)(1+s) & N_4 &= \frac{1}{4}(1-r)(1+s) \end{aligned} \quad (3.3.2)$$

The stiffness matrix

The unknowns which are the displacement in the x direction, u and the displacement in the y direction, v are expressed by using the shape functions given by Eq. 3.3.2 as:

$$u = \sum_{i=1}^4 N_i u_i \quad \text{and} \quad v = \sum_{i=1}^4 N_i v_i \quad (3.3.3)$$

The strains are related to the displacements by the strain displacement matrix $[B]$ by the equation:

$$\{\varepsilon\} = [B]\{d\} \quad (3.3.4)$$

where $\{d\} = [u_1, v_1, u_2, v_2, u_3, v_3, u_4, v_4]^T$. $[B]$ is the product of the rectangular matrices in the following three equations (Cook et al, 1989):

$$\{\boldsymbol{\varepsilon}\} = \begin{Bmatrix} \varepsilon_x \\ \varepsilon_y \\ \gamma_{xy} \end{Bmatrix} = \begin{bmatrix} 1 & 0 & 0 & 0 \\ 0 & 0 & 0 & 1 \\ 0 & 1 & 1 & 0 \end{bmatrix} \begin{Bmatrix} \mathbf{u}_{,x} \\ \mathbf{u}_{,y} \\ \mathbf{v}_{,x} \\ \mathbf{v}_{,y} \end{Bmatrix} \quad (3.3.5)$$

$$\begin{Bmatrix} \mathbf{u}_{,x} \\ \mathbf{u}_{,y} \\ \mathbf{v}_{,x} \\ \mathbf{v}_{,y} \end{Bmatrix} = \begin{bmatrix} \Gamma_{11} & \Gamma_{12} & 0 & 0 \\ \Gamma_{21} & \Gamma_{22} & 0 & 0 \\ 0 & 0 & \Gamma_{11} & \Gamma_{12} \\ 0 & 0 & \Gamma_{21} & \Gamma_{22} \end{bmatrix} \begin{Bmatrix} \mathbf{u}_{,r} \\ \mathbf{u}_{,s} \\ \mathbf{v}_{,r} \\ \mathbf{v}_{,s} \end{Bmatrix} \quad (3.3.6)$$

$$\begin{Bmatrix} \mathbf{u}_{,r} \\ \mathbf{u}_{,s} \\ \mathbf{v}_{,r} \\ \mathbf{v}_{,s} \end{Bmatrix} = \begin{bmatrix} N_{1,r} & 0 & N_{2,r} & 0 & N_{3,r} & 0 & N_{4,r} & 0 \\ N_{1,s} & 0 & N_{2,s} & 0 & N_{3,s} & 0 & N_{4,s} & 0 \\ 0 & N_{1,r} & 0 & N_{2,r} & 0 & N_{3,r} & 0 & N_{4,r} \\ 0 & N_{1,s} & 0 & N_{2,s} & 0 & N_{3,s} & 0 & N_{4,s} \end{bmatrix} \begin{Bmatrix} \mathbf{d} \\ \mathbf{d} \\ \mathbf{d} \\ \mathbf{d} \end{Bmatrix}_{8 \times 1} \quad (3.3.7)$$

$\mathbf{u}_{,x}$ denotes the partial derivative of u with respect to x ($\partial u / \partial x$). Γ_{ij} can be obtained by the following equation:

$$[\boldsymbol{\Gamma}] = [\mathbf{J}]^{-1} = \frac{1}{\det[\mathbf{J}]} \begin{bmatrix} J_{22} & -J_{12} \\ -J_{21} & J_{11} \end{bmatrix} \quad (3.3.8)$$

where $[\mathbf{J}]$ is the jacobian matrix expressed as:

$$[\mathbf{J}] = \begin{bmatrix} x_{,r} & y_{,r} \\ x_{,s} & y_{,s} \end{bmatrix} = \begin{bmatrix} \sum N_{i,r} x_i & \sum N_{i,r} y_i \\ \sum N_{i,s} x_i & \sum N_{i,s} y_i \end{bmatrix} \quad (3.3.9)$$

The element stiffness matrix $[\mathbf{k}]$ is obtained by the following integration over the area of the element :

$$[\mathbf{k}] = \int \int_{-1}^1 \int_{-1}^1 [\mathbf{B}]^T [\mathbf{E}][\mathbf{B}] dx dy = \int \int_{-1}^1 [\mathbf{B}]^T [\mathbf{E}][\mathbf{B}] \det[\mathbf{J}] dr ds \quad (3.3.10)$$

where the constitutive matrix [E] that relates the strains to stresses by the equation $\{\sigma\} = [E]\{\varepsilon\}$ is given below for isotropic linear elastic material and plane-strain condition.

$$\begin{Bmatrix} \sigma_x \\ \sigma_y \\ \tau_{xy} \end{Bmatrix} = \frac{E}{(1+\nu)(1-2\nu)} \begin{bmatrix} 1-\nu & \nu & 0 \\ \nu & 1-\nu & 0 \\ 0 & 0 & \frac{1-2\nu}{2} \end{bmatrix} \begin{Bmatrix} \varepsilon_x \\ \varepsilon_y \\ \gamma_{xy} \end{Bmatrix} \quad (3.3.11)$$

CHAPTER 4

FINITE ELEMENT ANALYSES FOR 8 METER HIGH WALL RESTING ON ELASTIC FOUNDATION SOIL

In this section, the dynamic behaviour of gravity and cantilever walls, and the effect of the frequency characteristics of base motions on the lateral pressures acting on the walls are investigated. For this purpose, a gravity and a cantilever retaining wall of 8m high with identical soil and loading conditions are considered. The soil-wall systems are subjected to base motions with constant peak acceleration but different frequencies.

4.1 Gravity wall

The dynamic response of a typical gravity retaining wall is presented in this section. Both sliding and rocking deformations of the wall are taken into account as the wall is modelled to rest on a soil layer.

4.1.1 The model and the parameters

The typical model used in the analyses is shown in Figure 4.1.1.1. The wall is resting on a foundation soil layer that is underlain by a rigid base which is fixed in the vertical direction and subjected to the base motion in the horizontal direction. Appropriate dashpots are utilized at the side boundaries to satisfy the free-field conditions (See Section 3.2.3 for details). The wall and the backfill soil are separated from each other and the contact is defined between the adjacent surfaces.

The typical finite element mesh is shown in Figure 4.1.1.2. The mesh is formed of 4 node quadrilateral plane-strain elements to represent the soil and the wall. In addition, contact elements between the wall and backfill, and dashpots between shear beams and the soil boundaries are provided. The dimensions and the material parameters are summarized in Table 4.1.1.1.

The base motion applied to the base is a sinusoidal acceleration time-history given by :

$$a(t) = \alpha \cdot g \cdot \sin(\omega_g \cdot t) \quad (4.1)$$

where g is the gravitational acceleration, α is the acceleration coefficient, ω_g is the circular frequency of the ground motion that can be expressed as:

$$\omega_g = 2 \cdot \pi \cdot f_g \quad (4.2)$$

where f_g denotes the frequency of the base motion.

The frequency ratio, R_f is defined as:

$$R_f = f_g / f_n \quad (4.3)$$

where f_n is the natural vibration frequency of the soil layer which can be determined by the following formula:

$$f_n = V_s / (4H_t) \quad (4.4)$$

where H_t is the height of the soil layer above the base at which the base motion is applied.

6 different base motions with varying frequency ratios of: $R_f = 0.2, 0.5, 0.75, 1$ (resonance case), 2, 3 and 5 are considered for the examination of the effect of R_f

on the lateral pressure distributions. The acceleration amplitude (or the peak acceleration) of the base motion is assumed as 0.3g.

The system is solved statically and the initial stress conditions are calculated prior to the dynamic loading. In the calculations, the weight of the wall and soil is taken into account. For all cases, the time interval for the static loading is taken as 0-1 seconds, so as to reach the static stresses and deformations at $t=1$ seconds. Thus, the base motion, hence the dynamic loading starts at $t=1$ seconds.

The acceleration time-history of the ground motion for the resonance case is given in Figure 4.1.1.3 as a sample of the ground motions. In the preliminary analyses, it is observed that the response of the system may be too large when the maximum accelerations are applied suddenly to the system (e.g. in the first cycle of the loading). Therefore, the acceleration is increased gradually to the peak value in the first 3 cycles. The peak acceleration value is remained in the following 6 cycles and diminished to zero in the last 3 cycles in a similar manner as in the first 3 ones.

The foundation layer and the retaining wall are assumed to be linear elastic while both linear elastic and elasto-plastic material models are used for the backfill so that the influence of yielding of backfill material on the lateral pressures can also be examined.

The damping ratio of the system is assumed to be 5% and Rayleigh damping is utilized with appropriate damping parameters as explained in Section 3.2.2 for each loading case.

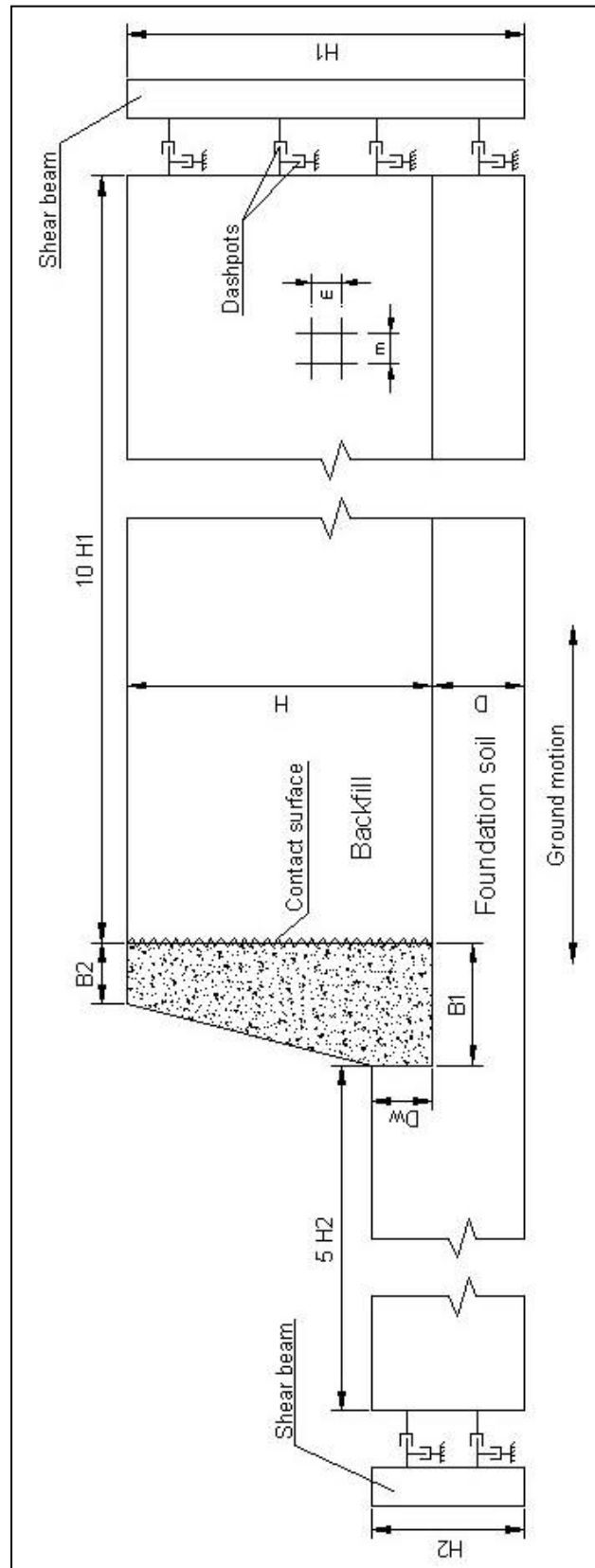


Figure 4.1.1.1 Typical model for the gravity wall analyses

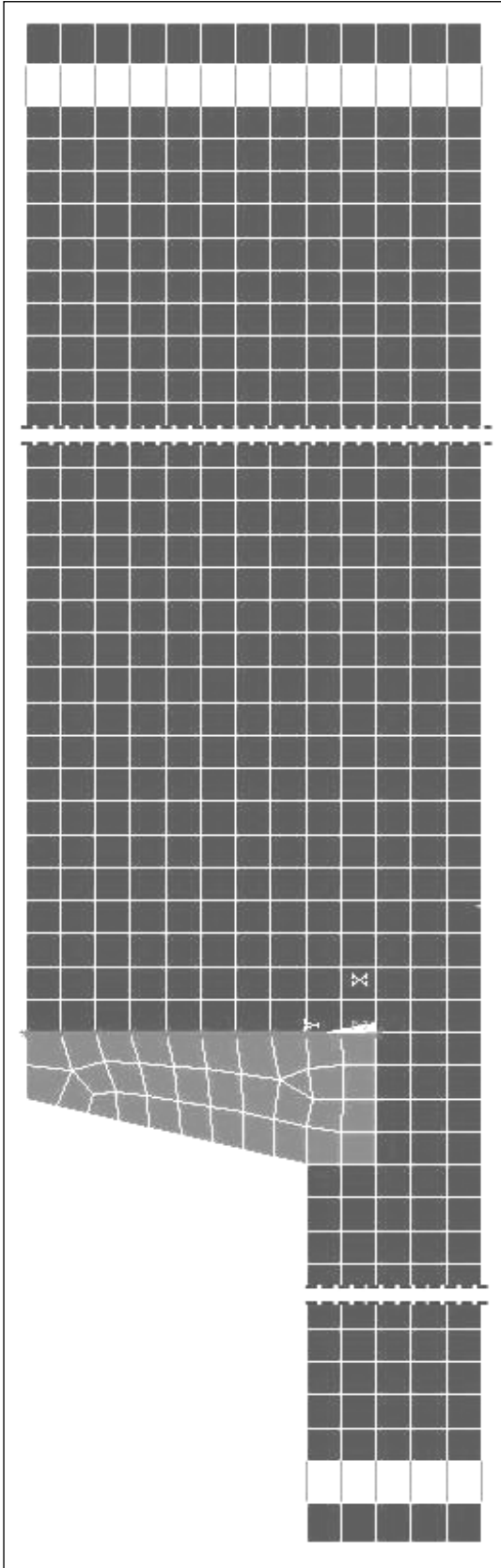


Figure 4.1.1.2 Typical finite element mesh for the gravity wall analyses

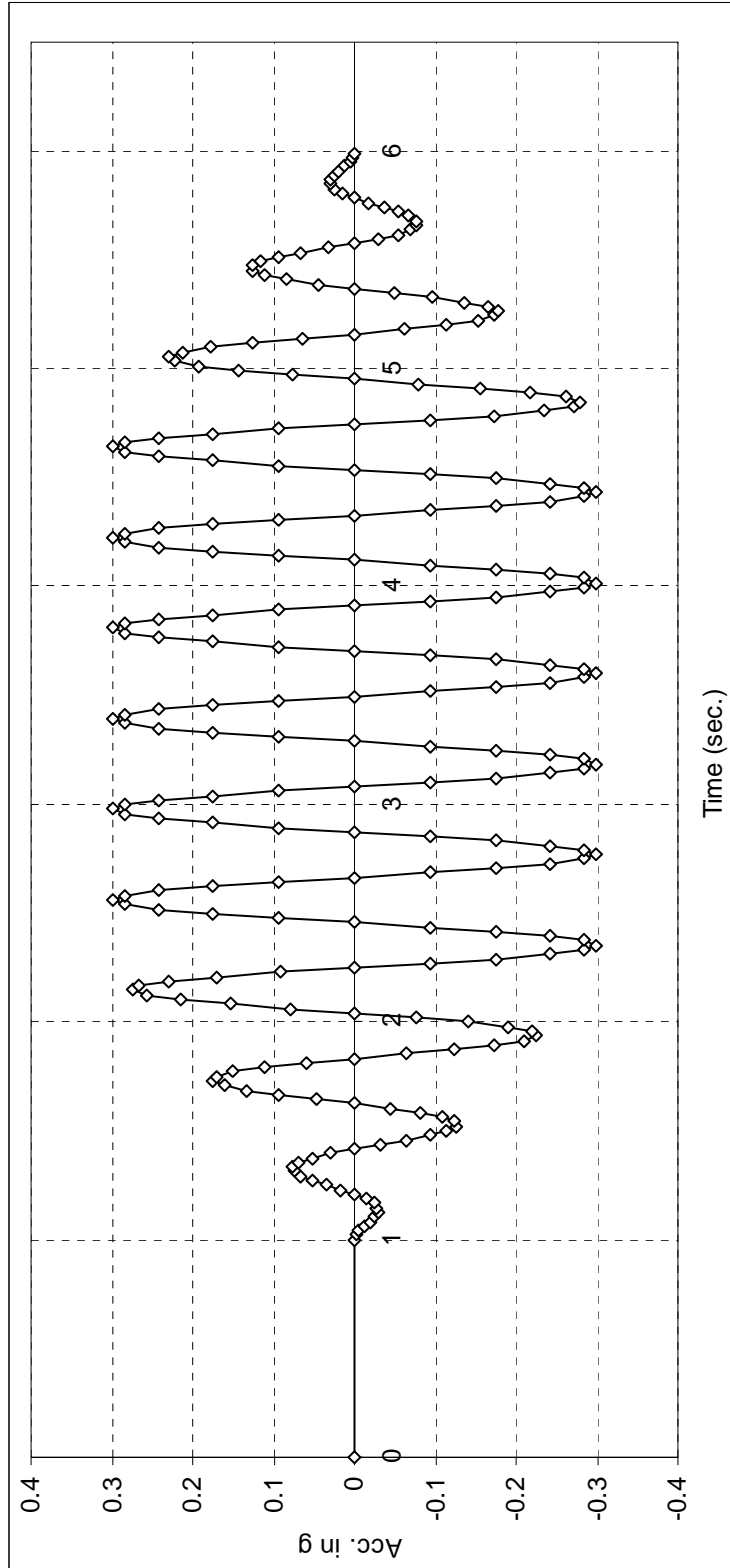


Figure 4.1.1.1.3 Sample acceleration time history of base motion ($\alpha=0.3$, $R_f=1$)

Table 4.1.1.1 Dimensions and material parameters considered in the gravity wall analyses

Symbol	Description	Unit	Value
H	Height of the wall	m	8
D	Foundation layer thickness	m	2.4
D _w	Wall foundation depth	m	1.6
B1	Wall dimensions	m	1.6
B2		m	3.2
ρ_s	Density of soil	t/m ³	1.8
E _s	Elasticity mod. of soil	kPa	47 880
ν_s	Poisson's ratio of soil	-	0.33
V _s	Shear wave velocity of soil	m/s	100
c	Drucker-Prager parameters (For E-P analysis)	kPa	0
ϕ		degree	33
ρ_w	Density of the wall	t/m ³	2.4
E _w	Elasticity mod. of the wall	kPa	25 x 10 ⁶
ν_w	Poisson's ratio of the wall	-	0.2

4.1.2 The results and comparisons

Analyses are carried out for the base motions with different frequency ratios of $R_f = 0.2, 0.5, 1, 2, 3$ and 5 as stated in Section 4.1.1 by using the finite element software ANSYS. For each time step, the total lateral thrust and base moment values are calculated by integrating the lateral soil stresses on the wall. In this way, the maximum total (static+dynamic) lateral thrust and its point of application are determined for each loading. Tensile stresses are omitted in the integration since the wall and backfill are separated at this stage and no force is exerted on the wall. The variation of the total lateral thrust with time is given in Figure 4.1.2.1 for the case of linear elastic backfill and a frequency ratio of $f_g/f_n=2$ as an example of the results.

There is a linear increase of the lateral pressures in the interval between $t=0$ and $t=1$ seconds wherein the static loading is applied. After $t=1$ seconds, as it is to be expected, the total lateral thrust varies with a pattern of the harmonic base motion.

The dynamic behaviour of the gravity retaining wall is illustrated on the Figures 4.1.2.2 to 4.1.2.6 where the deformed mesh at various instants are shown. The deformations are magnified by 50 times in the figures. It can be seen that even the wall is quite stiff, it undergoes a considerable rotation which may lead to a decrease of the lateral soil pressures.

The Drucker-Prager parameters are assumed to be $c=0$ and $\phi=33$ as given in Table 4.1.1.1. However, in the elasto-plastic analyses that frequency ratios are chosen to be 1 and 0.75, due to the large amplification of the accelerations and complex contact behaviour, convergence difficulties are encountered and the cohesion value is increased up to 20 kPa for some of the backfill elements at the near-bottom of the wall as indicated in Figure 4.1.2.2 by “x” marks on the elements to achieve convergence. Yielding of the backfill has taken place in all of the cases considered herein. The uniform plastic strain vectors for two cases are shown in Figures 4.1.2.7 and 4.1.2.8.

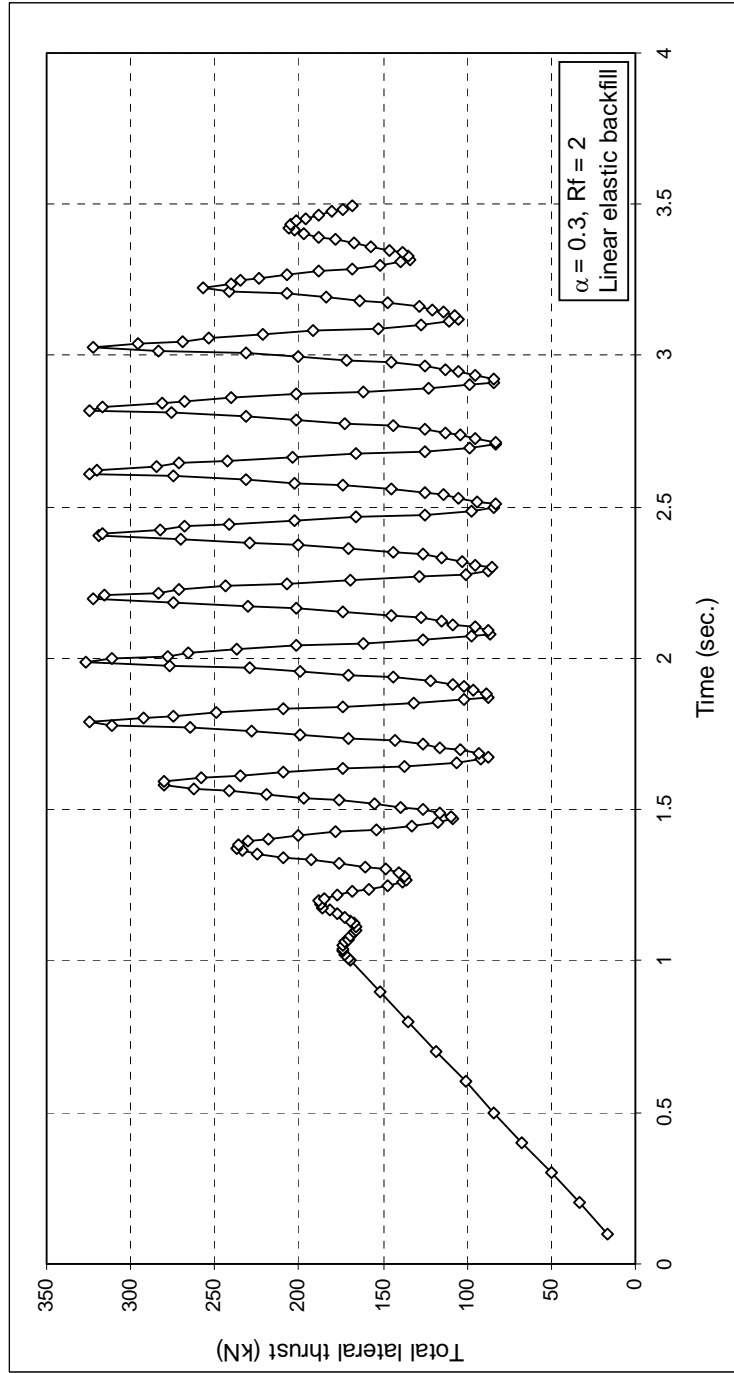


Figure 4.1.2.1 Sample variation of the total lateral force with time for gravity wall

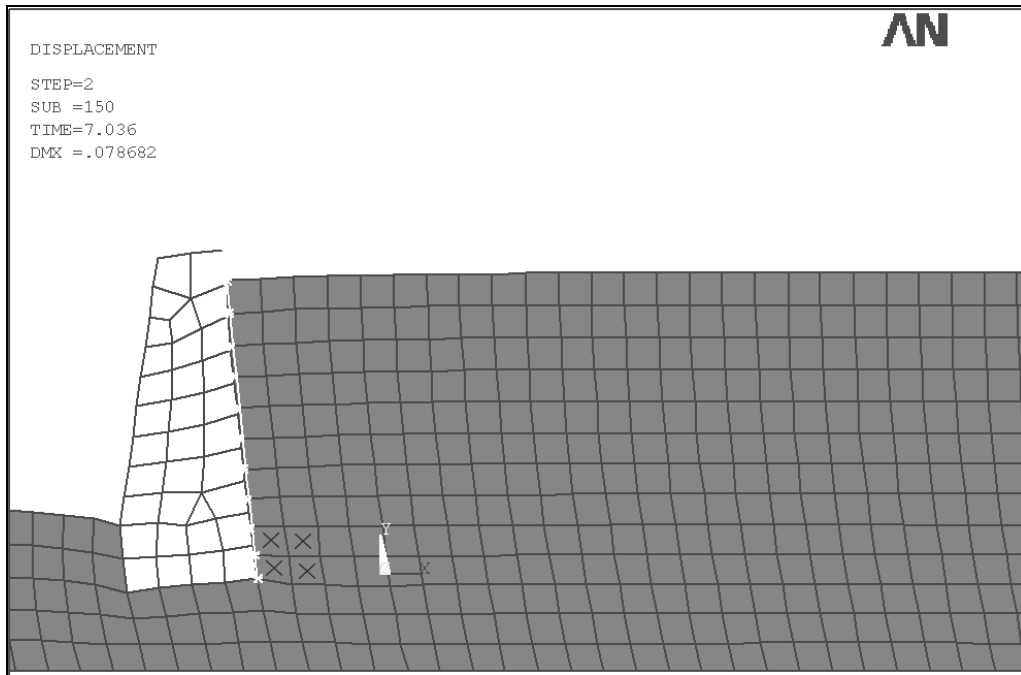


Figure 4.1.2.2 Deformed mesh for the gravity wall
(H=8m, L.E backfill, $\alpha=0.3$, $R_f=0.5$, $t=7.036$ s.)

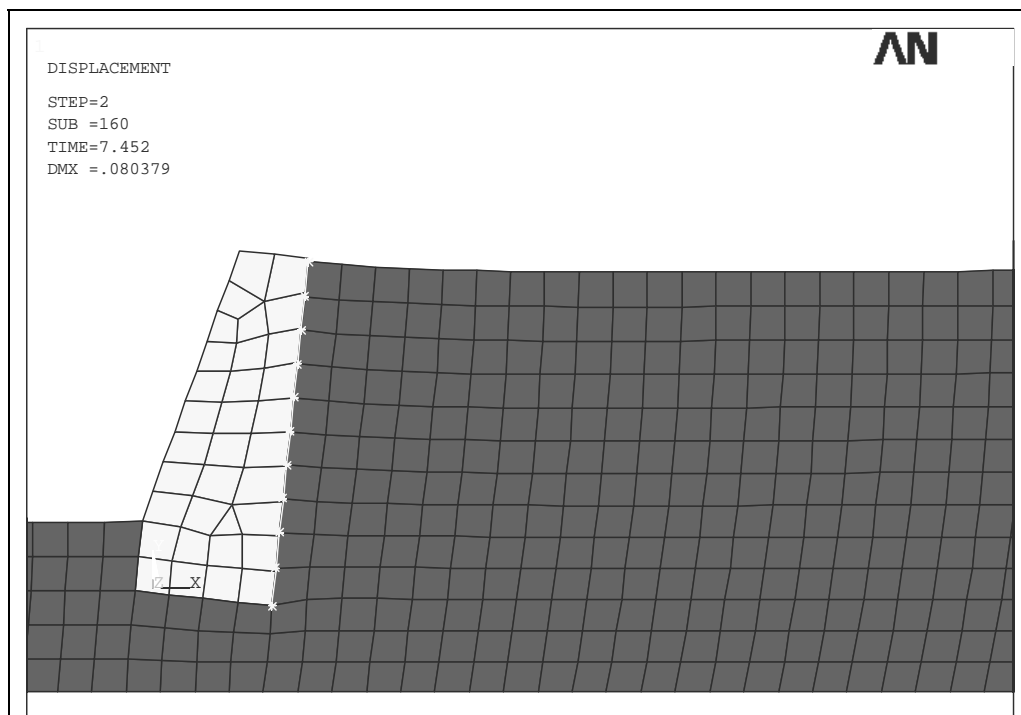


Figure 4.1.2.3 Deformed mesh for the gravity wall
(H=8m, L.E backfill, $\alpha=0.3$, $R_f=0.5$, $t=7.452$ s.)

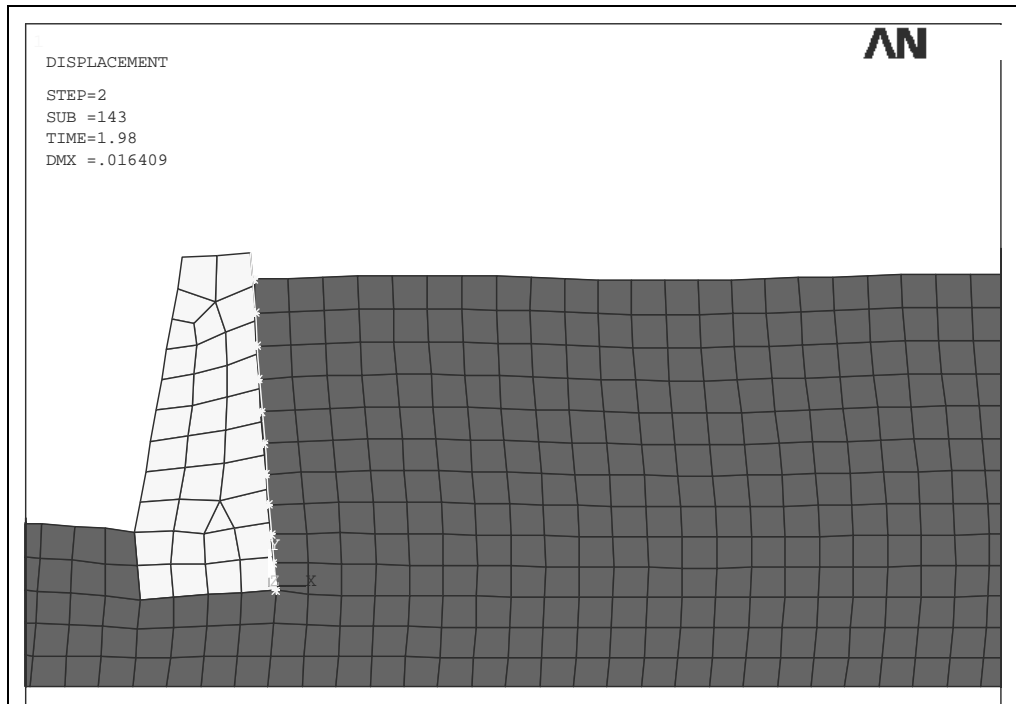


Figure 4.1.2.4 Deformed mesh for the gravity wall
 (H=8m, L.E backfill, $\alpha=0.3$, $R_f=3$, $t=1.98$ s.)

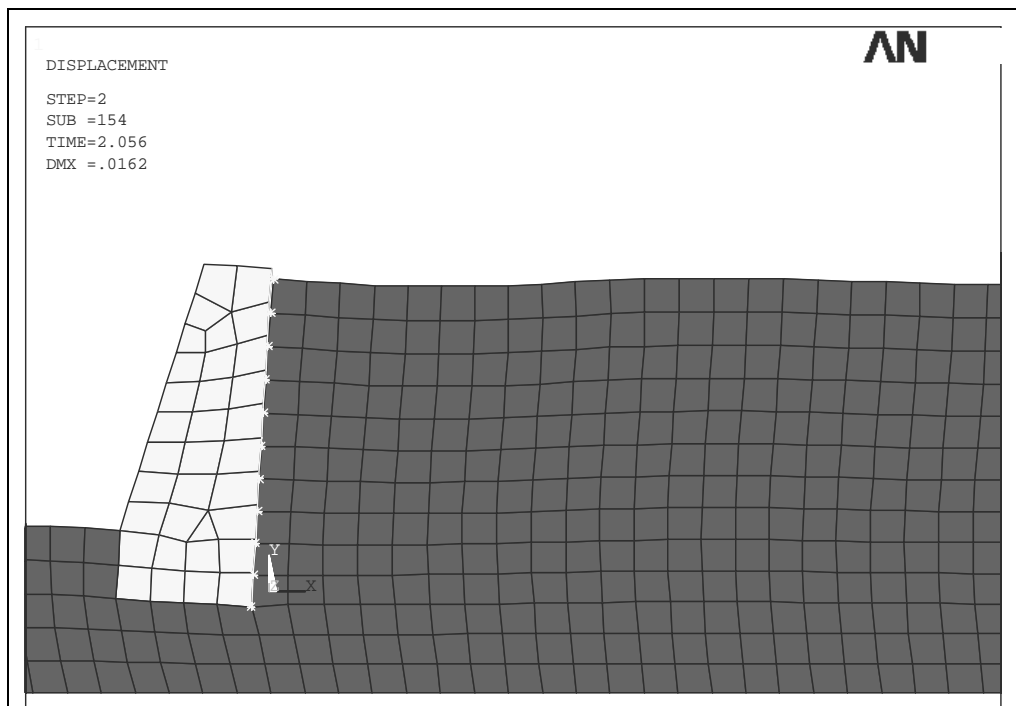


Figure 4.1.2.5 Deformed mesh for the gravity wall
 (H=8m, L.E backfill, $\alpha=0.3$, $R_f=3$, $t=2.056$ s.)

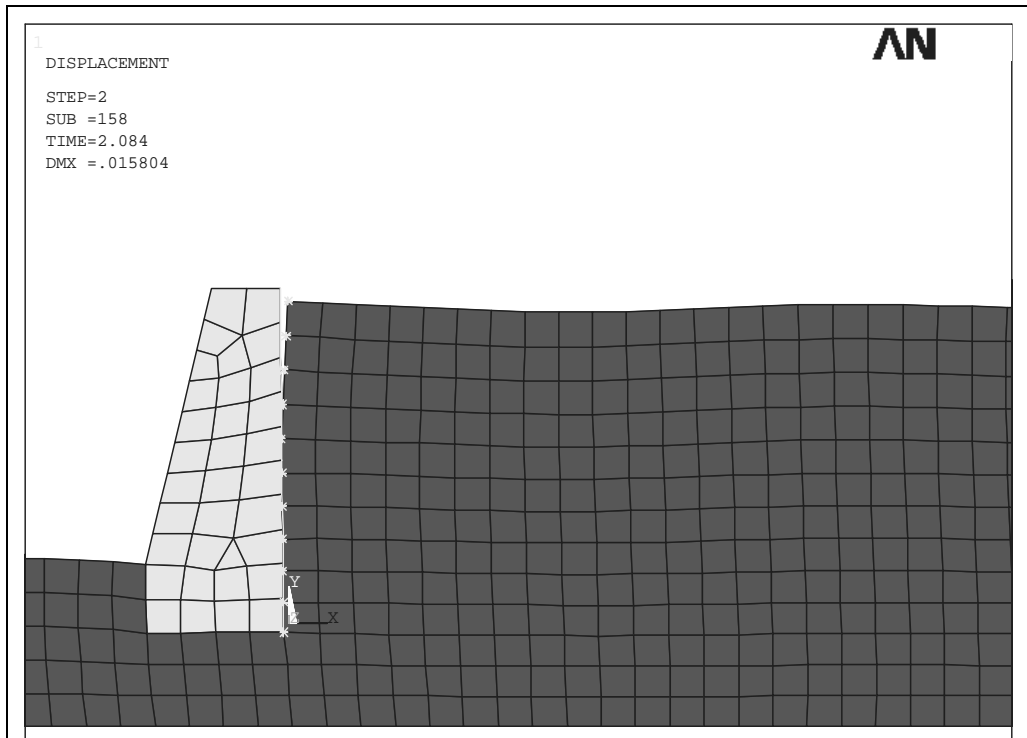


Figure 4.1.2.6 Deformed mesh for the gravity wall
(H=8m, L.E backfill, $\alpha=0.3$, $R_f = 3$, $t=2.084$ s.)

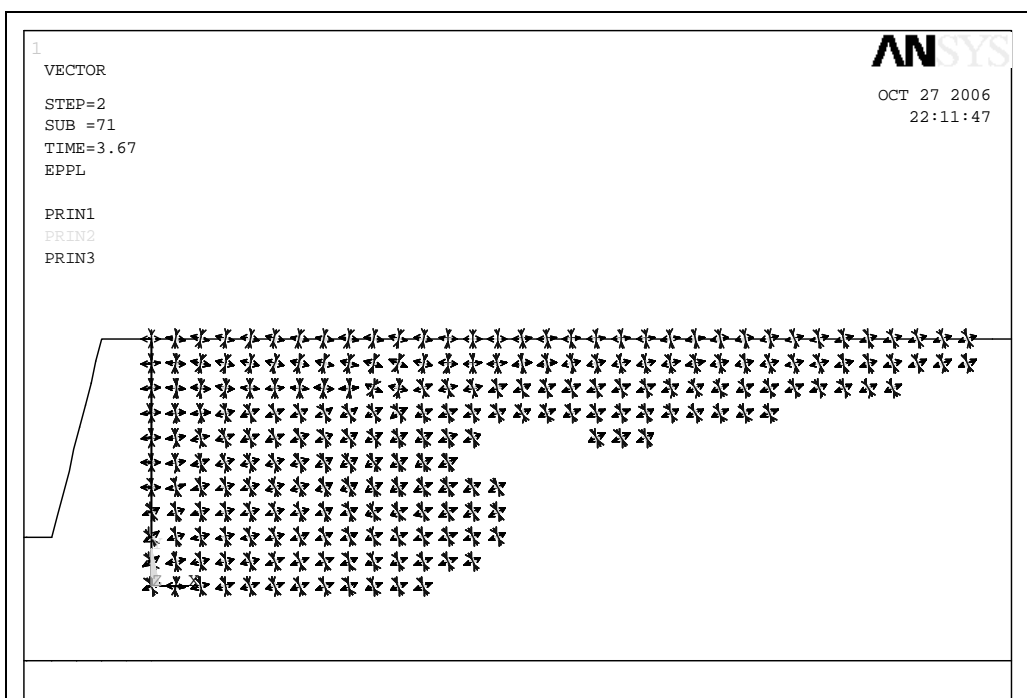


Figure 4.1.2.7 Plastic strain vectors for the gravity wall(H=8m, $\alpha=0.3$, $R_f = 0.5$)

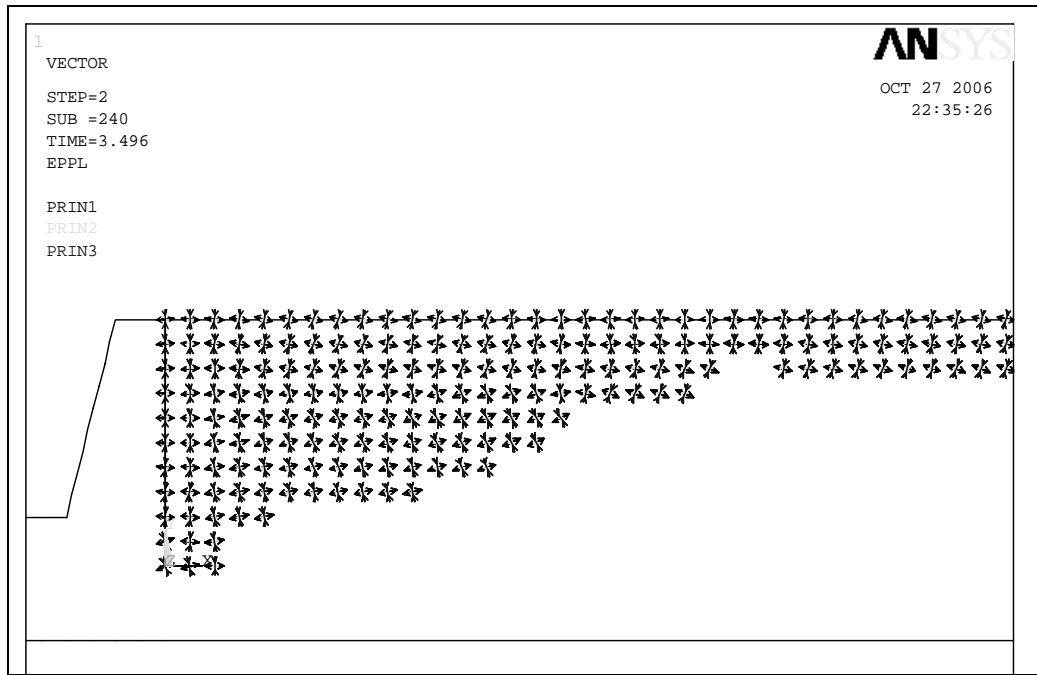


Figure 4.1.2.8 Plastic strain vectors for the gravity wall(H=8m, $\alpha=0.3$, $R_f=2$)

The total lateral force vs. frequency ratio is shown in Figure 4.1.2.9 in which the results of Mononobe-Okabe, Steedman and Zeng and Wood solutions are also included. In the graph, the total lateral force is expressed in non-dimensional form as:

$$F_{td} = \frac{F_t}{\gamma H^2} \quad (4.5)$$

where F_t is the maximum total lateral force, γ is the unit weight of the backfill and H is the height of the wall.

The amplification ratios of the surface acceleration to the base acceleration for the considered soil layer are shown in Figure 4.1.2.10 for different R_f values and 5% damping.

The significant effect of the frequency ratio can be seen from Figure 4.1.2.9. For low frequency motions ($f_g < f_n$), the lateral force increases as f_g increases and takes

the peak value at $f_g=f_n$. For high frequency motions ($f_g>f_n$), the lateral force decreases with increasing f_g .

Extremely high values of the total lateral thrust are obtained from the finite element (FE) analyses for the resonance case compared to the other frequency ratios. Such high values are mainly due to the great amplification in the backfill, resulting in a good agreement with Steedman and Zeng solution especially for the case of linear elastic backfill. On the other hand, for high frequency motions, the amplification ratio has no considerable influence on the lateral thrust as can be seen particularly from the results for $R_f = 3$.

Since there is a considerable rotation of the gravity wall as mentioned before, the results are reasonably agreeable with M-O solution except in the vicinity of $R_f = 1$.

Results of elasto-plastic analyses are similar to those of linear elastic analyses especially for high frequency motions.

The distance of points of application of the total lateral force from the wall base, normalized to the wall height; h_n vs. frequency ratio are given in Figure 4.1.2.11. Here, h_n is defined as:

$$h_n = h / H \quad (4.6)$$

where h is the distance of the application point to the base of the wall. The height of the application point is generally in good agreement with M-O method. Both total lateral thrust and location of application points found by elasto-plastic and linear elastic analyses are in good agreement.

Maximum total bending moments at the base of the wall vs. frequency ratios are presented on Figure 4.1.2.12. The moment is expressed in non-dimensional form as:

$$M_{td} = \frac{M_t}{\gamma H^3} \quad (4.7)$$

where M_t is the total bending moment at the base of the wall due to the lateral pressures acting on the wall. It can be observed that the moments are lower than those obtained by Wood solution, but in good agreement with M-O or Seed and Whitman methods depending on R_f , except for the resonance case.

The total lateral pressure distributions corresponding to the maximum lateral thrust are shown in Figures 4.1.2.13, 4.1.2.14 and 4.1.2.15. Here the non-dimensional lateral pressure q_{hd} is defined as:

$$q_{hd} = \frac{q_h}{\gamma H} \quad (4.8)$$

where q_h is the total lateral stress. It can be seen from the figures that the total lateral stress falls below the static lateral stress at some points. Additionally negative total lateral stresses are obtained at some points where static lateral stresses are positive. This makes it impracticable to consider the application point of the dynamic force separately.

Obtained results for the gravity wall of $H = 8$ m high are summarized in Table 4.1.2.1. The maximum dynamic lateral forces, obtained by subtracting the static lateral forces from the maximum total lateral forces are given in Table 4.1.2.2. The maximum dynamic lateral force is normalized to the peak base acceleration and expressed in non-dimensional form as:

$$F_{dd} = \frac{F_d}{\rho_s a_p H^2} \quad (4.9)$$

where F_d is the maximum dynamic lateral force and a_p is the peak acceleration of the base motion ($a_p = \alpha g$ for harmonic base motions).

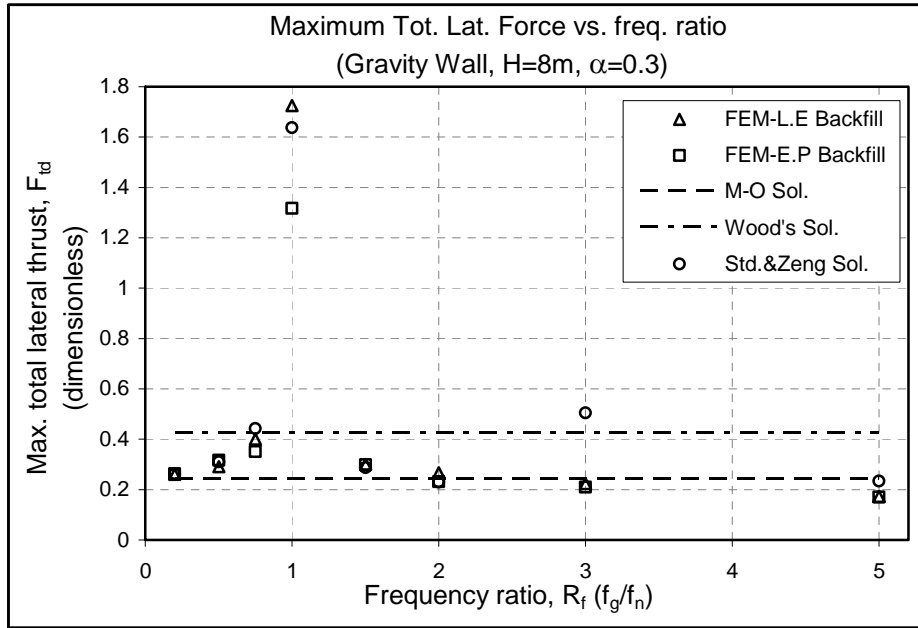


Figure 4.1.2.9 Maximum total lateral force vs. frequency ratio for gravity wall ($\alpha=0.3$)

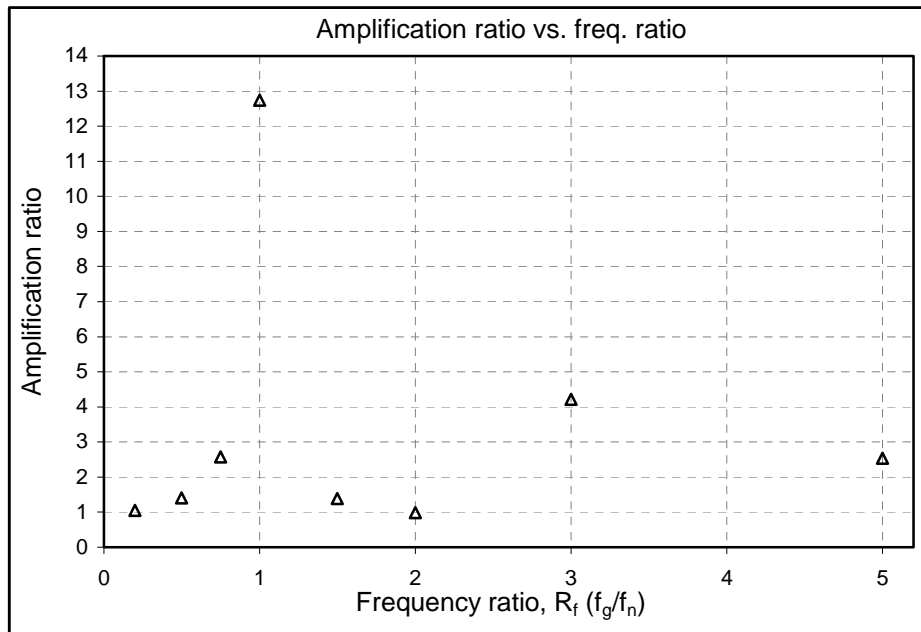


Figure 4.1.2.10 Amplification ratio vs. frequency ratio of the considered soil layer for 5% damping ratio.

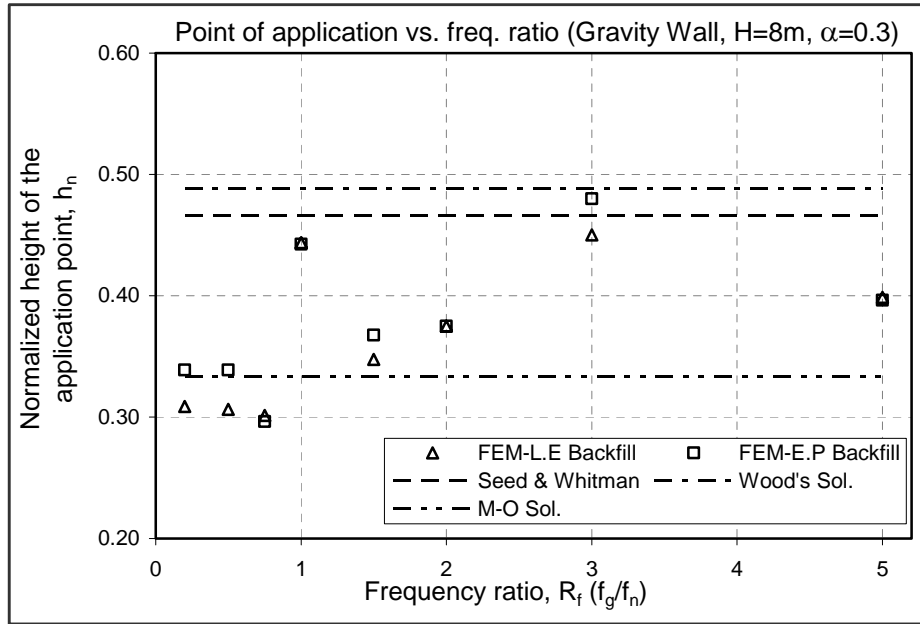


Figure 4.1.2.11 Distance of the point of application vs. frequency ratio for gravity wall ($\alpha=0.3$)

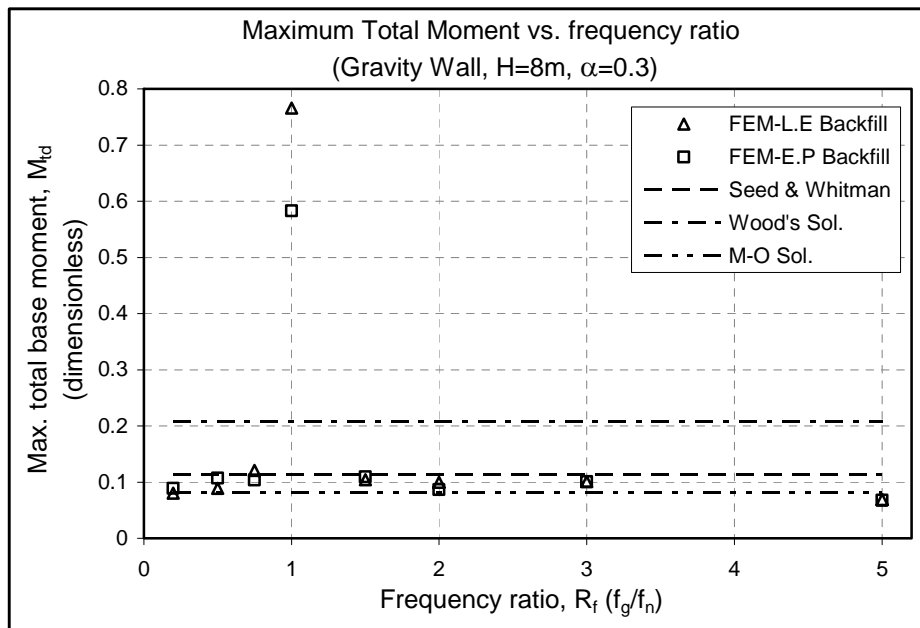


Figure 4.1.2.12 Maximum total moment force vs. frequency ratio for gravity wall ($\alpha=0.3$)

Table 4.1.2.1 Summary of the results for gravity wall

Freq. ratio (R_f)	Backfill material model	Total lat. force, F_t (kN)	Total base moment, M_t (kNm)	Height of application point, h	Non-dimensional total lat. force, F_{td}	Non-dimensional total base moment, M_{td}	Normalized height of app. point, h_n
0.2	L.E	295	729	2.47	0.261	0.081	0.31
0.2	E-P	297	805	2.71	0.263	0.089	0.34
0.5	L.E	329	806	2.45	0.291	0.089	0.31
0.5	E-P	357	967	2.71	0.316	0.107	0.34
0.75	L.E	453	1092	2.41	0.401	0.121	0.30
0.75	E-P	396	939	2.37	0.350	0.104	0.30
1	L.E	1950	6923	3.55	1.725	0.766	0.44
1	E-P	1489	5271	3.54	1.318	0.583	0.44
1.5	L.E	339	942	2.78	0.300	0.104	0.35
1.5	E-P	337	991	2.94	0.298	0.110	0.37
2	L.E	301	903	3	0.266	0.100	0.38
2	E-P	261	783	3	0.231	0.087	0.38
3	L.E	253	911	3.6	0.224	0.101	0.45
3	E-P	237	910	3.84	0.210	0.101	0.48
5	L.E	196	625	3.19	0.173	0.069	0.40
5	E-P	193	612	3.17	0.171	0.068	0.40

Table 4.1.2.2 Maximum dynamic lateral force results for gravity wall

Freq. ratio (R_f)	Backfill material model	Static lat. force, F_{sta} (kN)	Total lat. force, F_t (kN)	Dynamic lat. force, F_d (kN)	Non-dimensional dynamic lat. force, F_{dd}
0.2	L.E	171	295	124	0.37
0.2	E-P	174	297	123	0.36
0.5	L.E	171	329	158	0.47
0.5	E-P	174	357	183	0.54
0.75	L.E	171	453	282	0.83
0.75	E-P	174	396	222	0.65
1	L.E	171	1950	1779	5.25
1	E-P	174	1489	1315	3.88
1.5	L.E	171	339	168	0.50
1.5	E-P	174	337	163	0.48
2	L.E	171	301	130	0.38
2	E-P	174	261	87	0.26
3	L.E	171	253	82	0.24
3	E-P	174	237	63	0.19
5	L.E	171	196	25	0.07
5	E-P	174	193	19	0.06

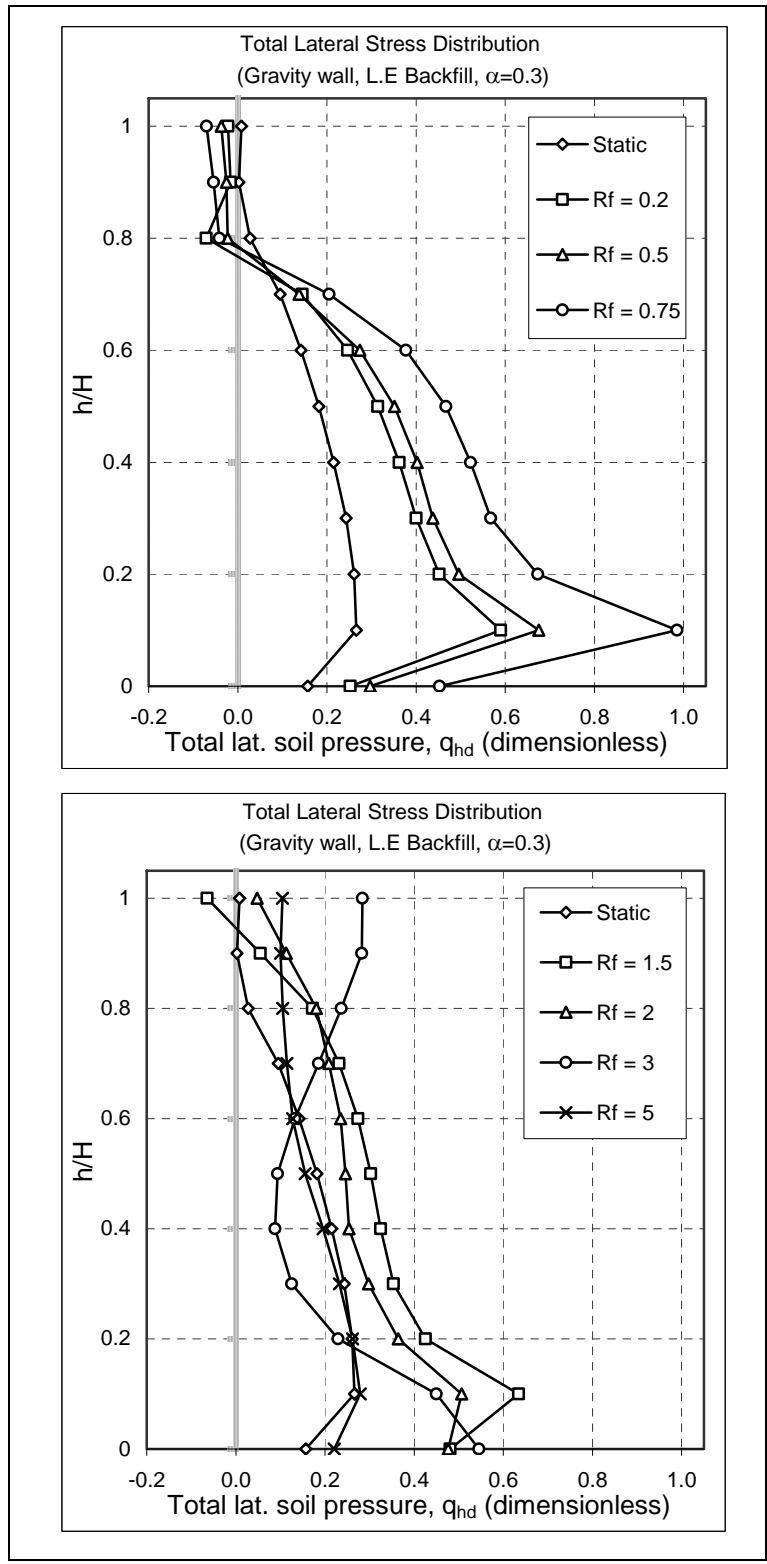


Figure 4.1.2.13 Total lateral stress distributions for max. thrust for various freq. ratios ($\alpha=0.3$, Gravity wall, $H=8m$)

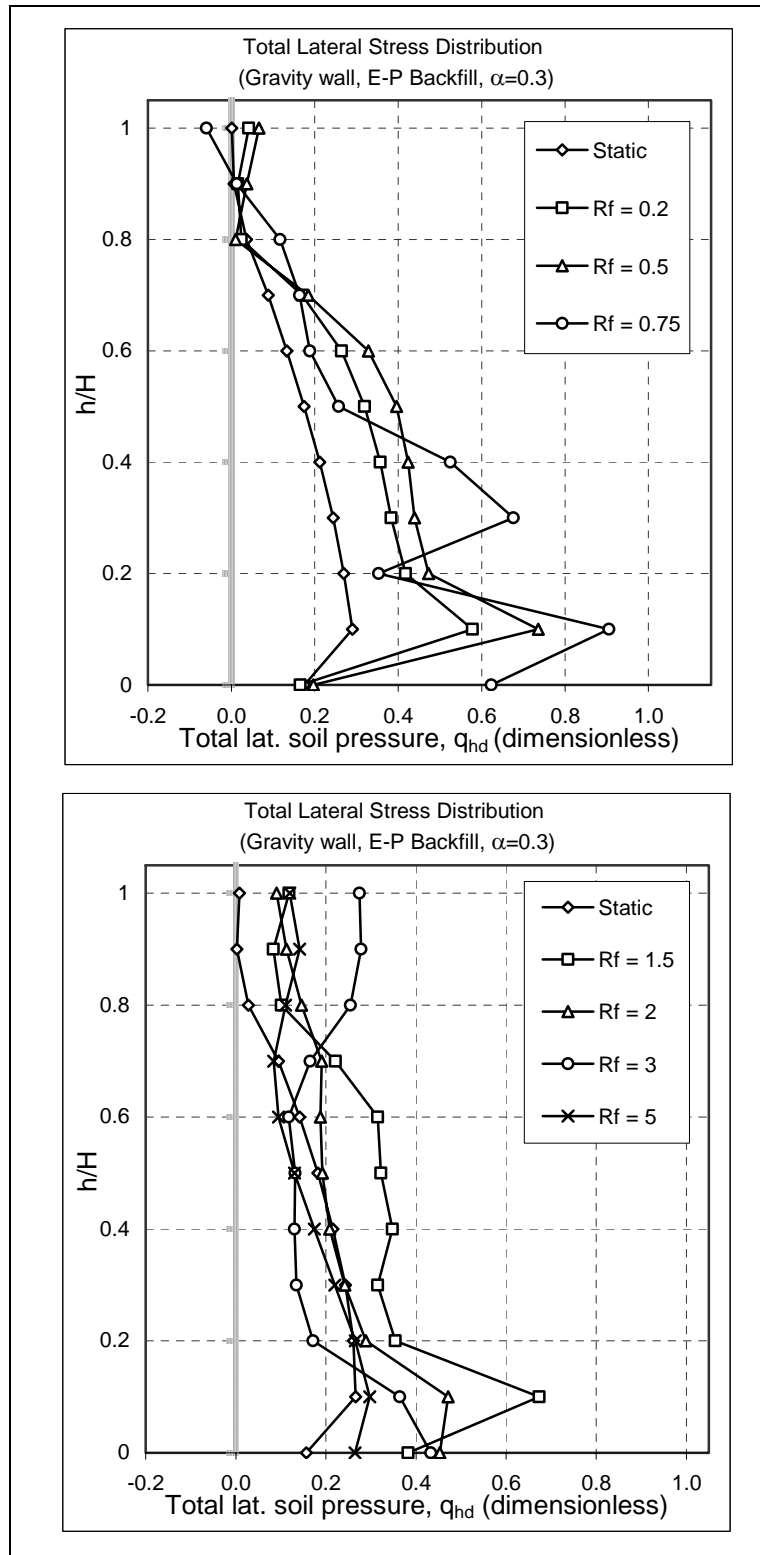


Figure 4.1.2.14 Total lateral stress distributions for max. thrust for various freq. ratios ($\alpha=0.3$, Gravity wall, $H=8\text{m}$)

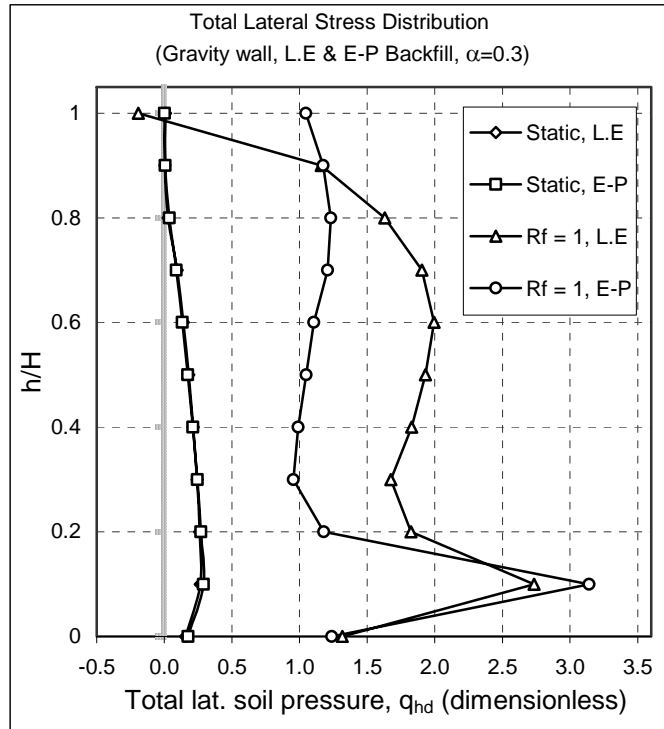


Figure 4.1.2.15 Total lateral stress distribution for max. thrust for the resonance case ($\alpha=0.3$, Gravity wall, $H=8\text{m}$)

4.2 Cantilever wall

The dynamic behaviour of a gravity wall has been presented in the previous section. In this section, a typical cantilever wall of same height with identical backfill and loading conditions are examined.

4.2.1 The model and the parameters

The typical model is shown in Figure 4.2.1.1. A foundation soil layer underlain by a rigid base is modelled beneath the base of the wall. The contact elements are defined between the vertical adjacent surfaces of the wall and backfill. Dashpots connecting the soil layers to the shear beams are utilized to simulate free-field conditions at the side boundaries.

The finite element mesh used in the analyses is shown in figure 4.2.1.2. 4 node quadrilateral plane strain elements are used to represent the wall and soil. Contact elements and dashpots are also used in the mesh. The dimensions and the material parameters are summarized in Table 4.2.1.1.

The same base motions used for the gravity wall analyses are used in this part of the study having frequency ratios of $R_f = 0.2, 0.5, 0.75, 1, 1.5, 2, 3$ and 5. The dynamic loading starts following the static solution that takes place between $t=0-1$ seconds as described in Section 4.1.1.

Similar to the case of gravity wall, the foundation soil layer and the retaining wall are assumed to be linear elastic, while linear elastic and elasto-plastic material models are used for backfill soil. The damping ratio is assumed as 5% and Rayleigh damping (explained in Section 3.2.2) is utilized in the analyses.

Table 4.2.1.1 Dimensions and material parameters considered in the typical cantilever wall analyses

Symbol	Description	Unit	Value
H	Height of the wall	m	8
D	Foundation layer thickness	m	2.4
T1	Wall dimensions	m	0.8
T2		m	0.8
B1		m	2.4
B2		m	5.6
ρ_s	Density of soil	t/m ³	1.8
E_s	Elasticity mod. of soil	kPa	47 880
ν_s	Poisson's ratio of soil	-	0.33
V_s	Shear wave velocity of soil	m/s	100
c	Drucker-Prager parameters (For E-P analysis)	kPa	0
ϕ		degree	33
ρ_w	Density of the wall	t/m ³	2.4
E_w	Elasticity mod. of the wall	kPa	25×10^6
ν_w	Poisson's ratio of the wall	-	0.2

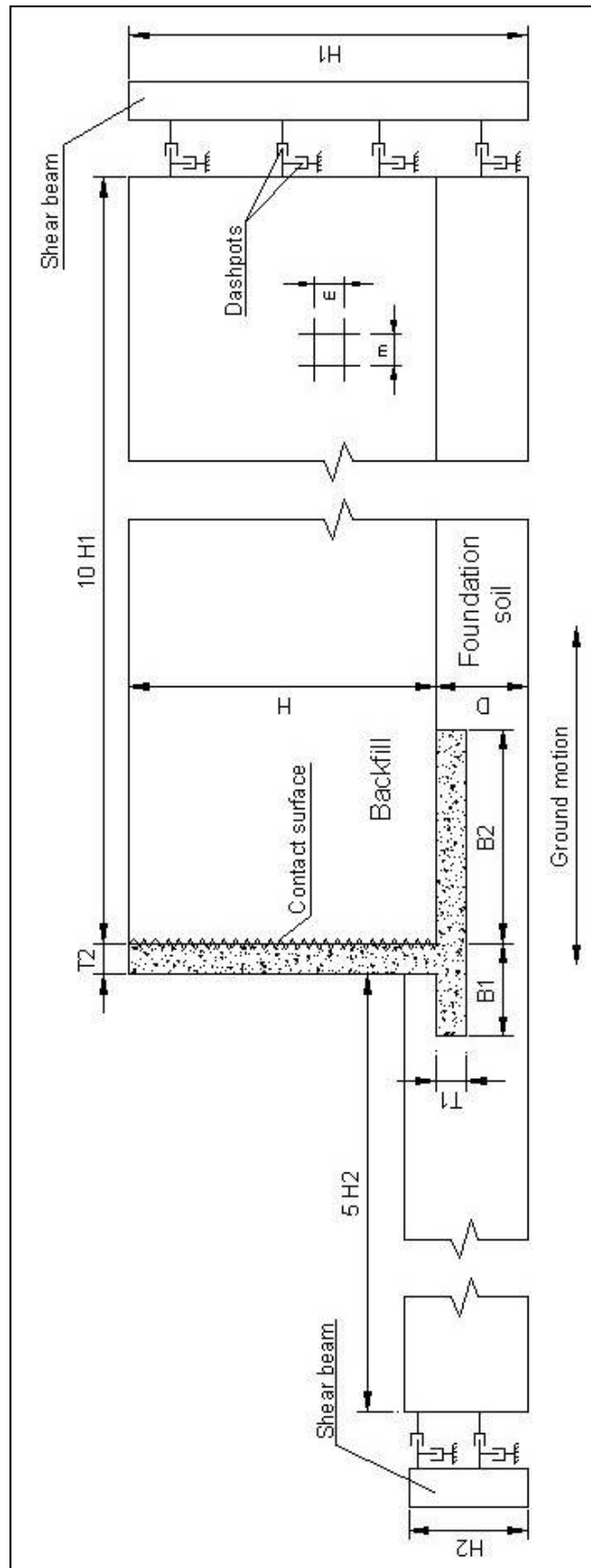


Figure 4.2.1.1 Typical model for the cantilever wall analyses

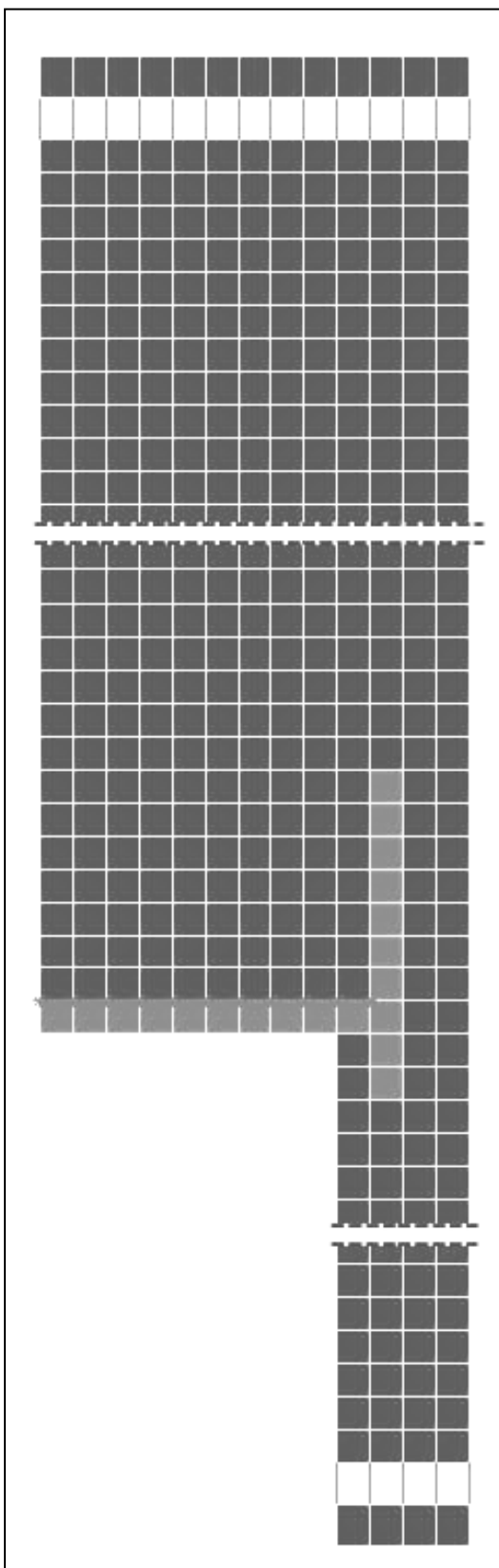


Figure 4.2.1.2 Typical finite element mesh for the cantilever wall analyses

4.2.2 The results and comparisons

The maximum total lateral thrust and its point of application are determined for each case. The variation of the total lateral force with time is presented in Figure 4.2.2.1 for the case of linear elastic backfill and $R_f = 2$ as an example of the results. Following the static solution completed at $t = 1$ seconds, the total lateral force variation is similar to the base motion as seen in the figure.

The deformed mesh plots (magnified by 50 times) at various instants are shown through Figures 4.2.2.2 to 4.2.2.5. The separation between the wall and backfill is clearly illustrated in Figures 4.2.2.3 and 4.2.2.4. The rotation of the wall is insignificant and the deflection of the wall, hence the flexibility of the wall mainly affects the lateral pressures.

For the cases of elasto-plastic backfill and R_f values of 0.75 and 1, the Drucker-Prager parameter, c is increased up to 20 kPa for some elements at the near bottom of the wall as indicated by “x” marks in Figure 4.2.2.2 to overcome convergence problems. Yielding of the backfill (full or partial) has taken place in all of the considered cases. The uniform plastic strain vectors for two cases are shown in Figures 4.2.2.6 and 4.2.2.7.

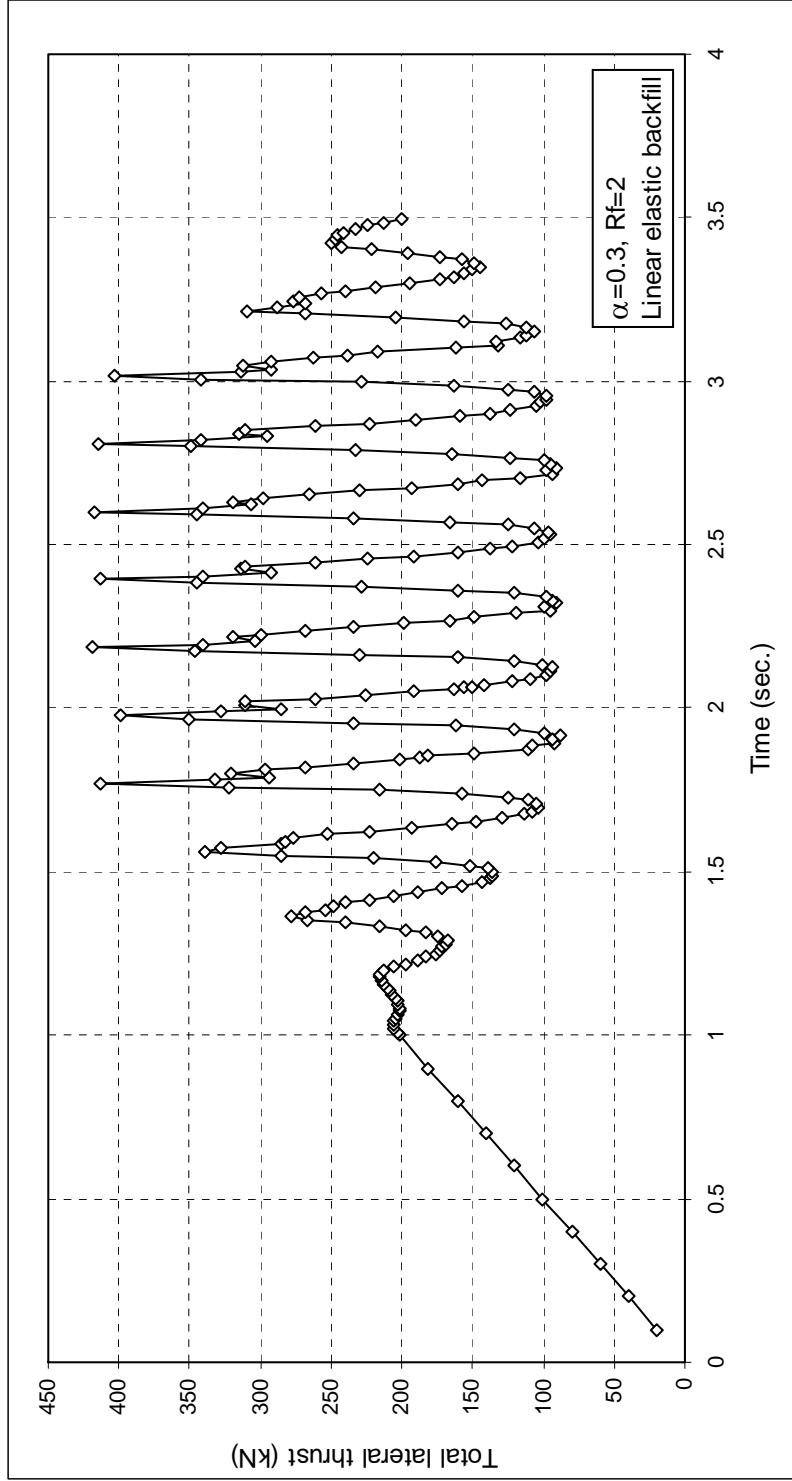


Figure 4.2.2.1 Sample variation of the total lateral force with time for cantilever wall

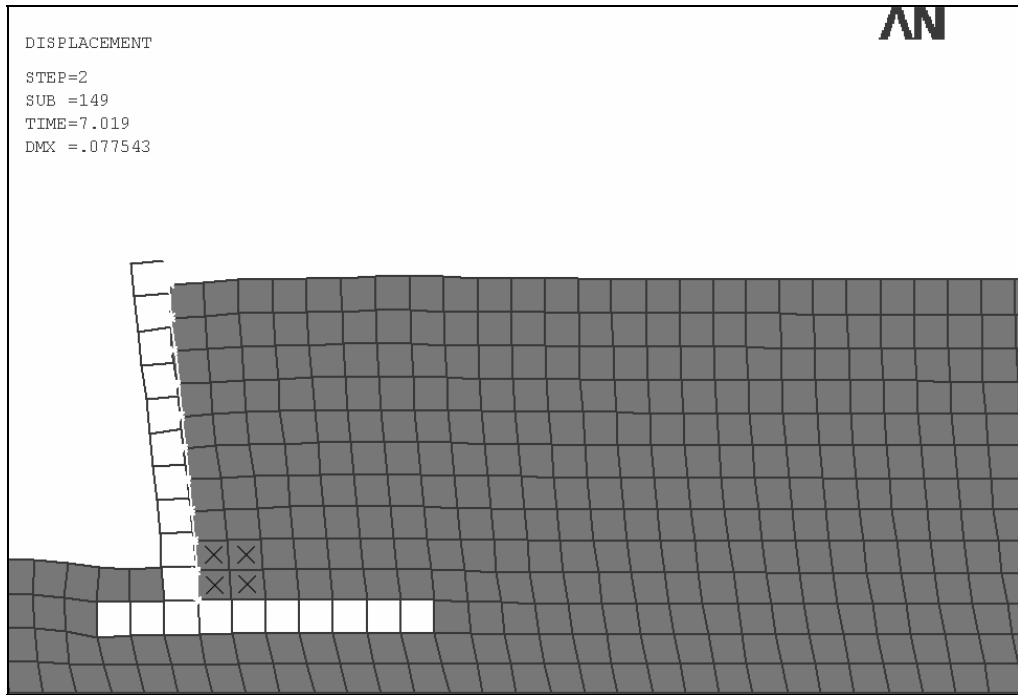


Figure 4.2.2.2 Deformed mesh for the cantilever wall
 (H=8m, L.E backfill, $\alpha=0.3$, $R_f=0.5$, $t=7.019$ s.)

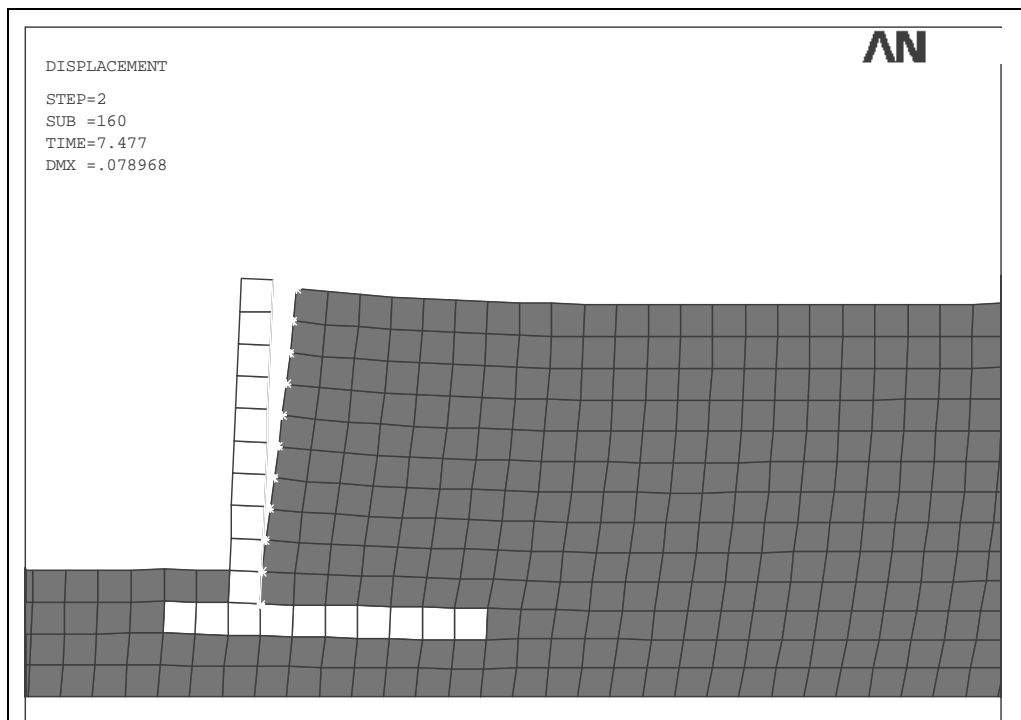


Figure 4.2.2.3 Deformed mesh for the cantilever wall
 (H=8m, L.E backfill, $\alpha=0.3$, $R_f=0.5$, $t=7.477$ s.)

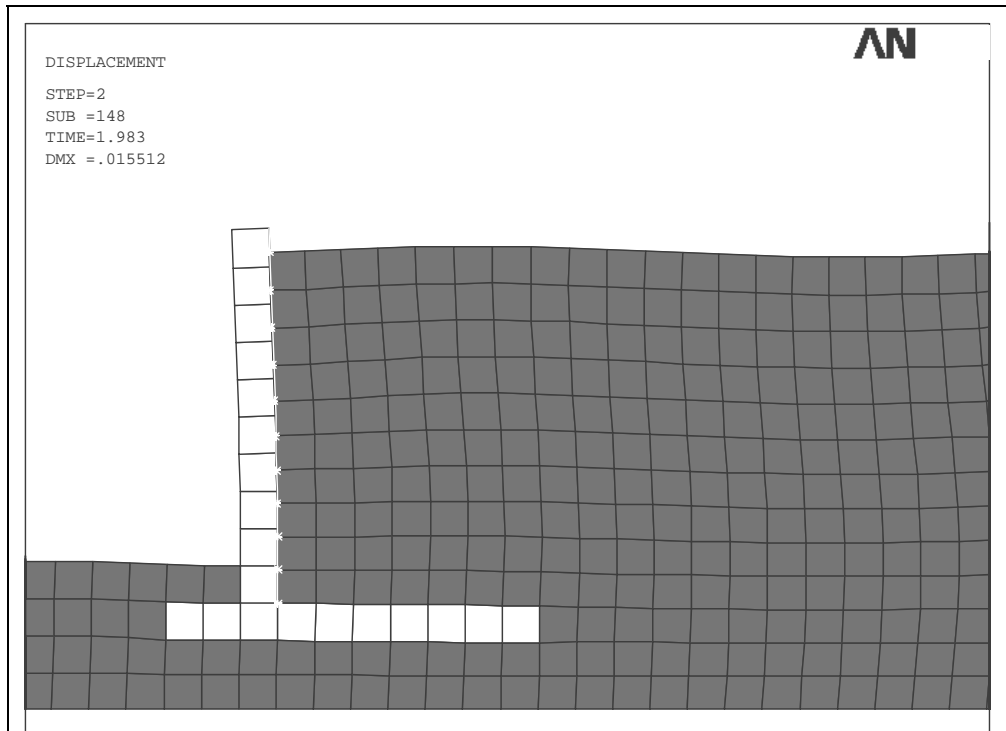


Figure 4.2.2.4 Deformed mesh for the cantilever wall
 (H=8m, L.E backfill, $\alpha=0.3$, $R_f=3$, $t=1.983$ s.)

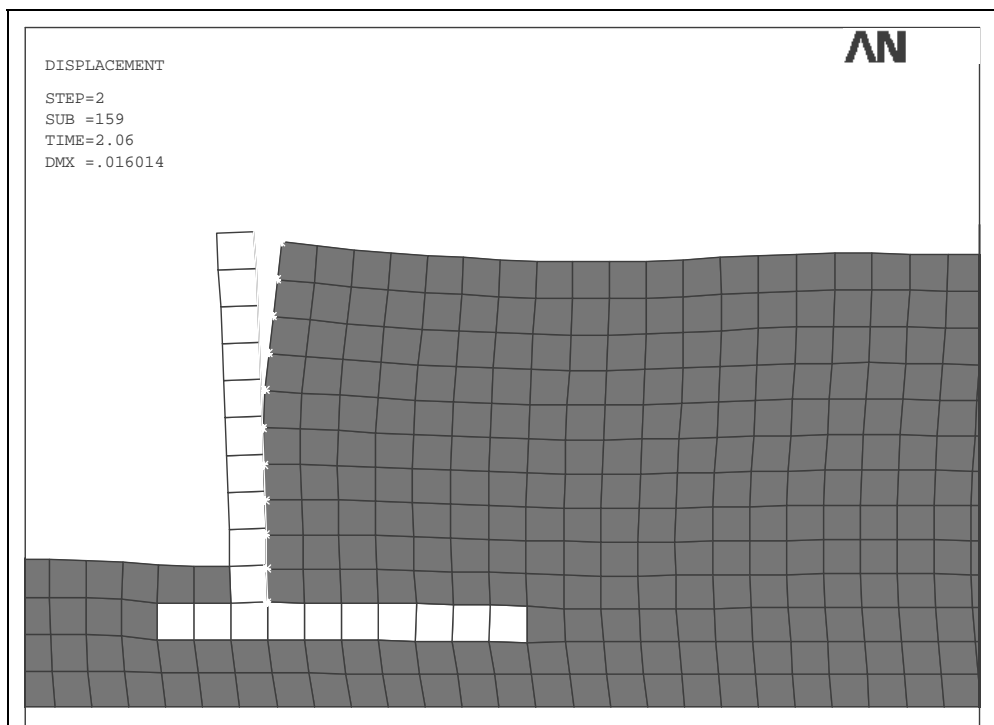


Figure 4.2.2.5 Deformed mesh for the cantilever wall
 (H=8m, L.E backfill, $\alpha=0.3$, $R_f=3$, $t=2.06$ s.)

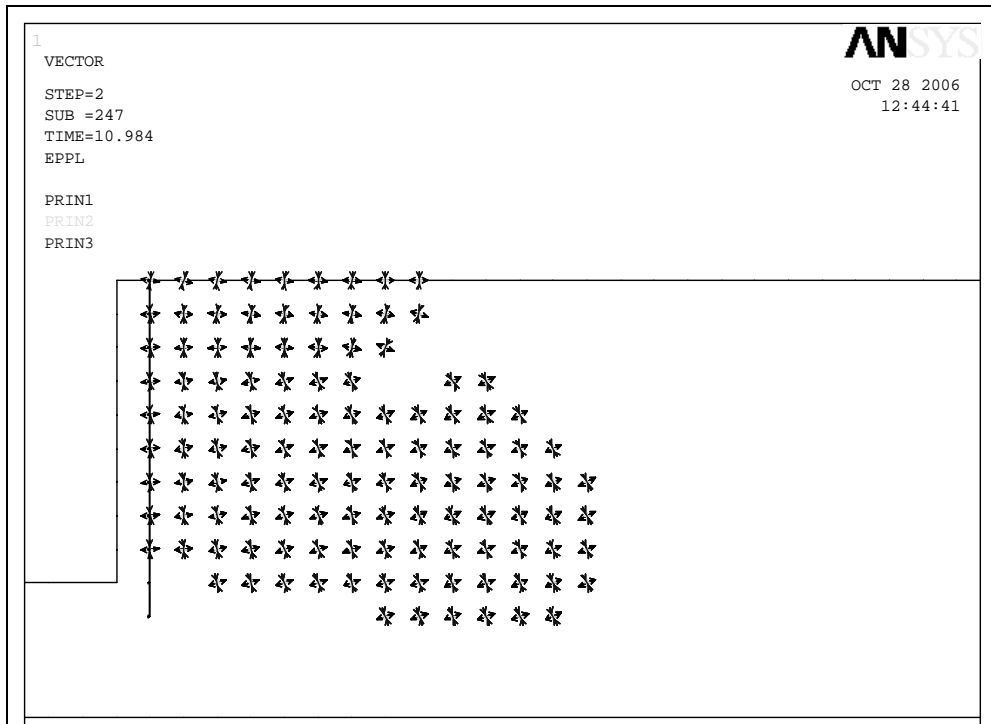


Figure 4.2.2.6 Plastic strain vectors for the cantilever wall($H=8\text{m}$, $\alpha=0.3$, $R_f=0.5$)

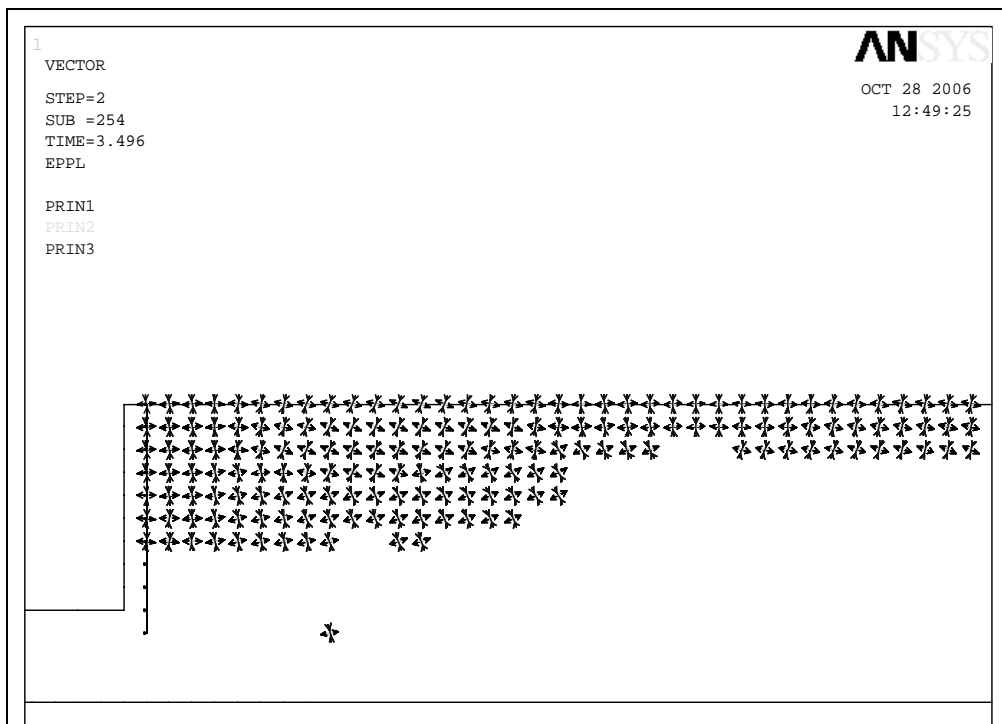


Figure 4.2.2.7 Plastic strain vectors for the cantilever wall($H=8\text{m}$, $\alpha=0.3$, $R_f=2$)

The non-dimensional maximum total lateral force, F_{td} ; distance of the point of application from the base of the wall, h_n and the maximum total bending moment at the base of the wall, M_{td} , are given in Figures 4.2.2.8, 4.2.2.9 and 4.2.2.10 respectively as a function of the frequency ratio, R_f .

The dynamic lateral force increases as the base motion frequency approaches the natural vibration frequency of the soil layer. F_{td} and M_{td} results for the resonance case are quite high as compared to other frequency ratios and to the results of M-O and Wood solutions. For the cantilever wall, finite element results are rather different from those obtained by Steedman and Zeng method that is directly affected by the amplification ratio (the lateral force increases with increasing amplification in the backfill in Steedman and Zeng method) at about resonance frequencies. FEM results of F_{td} are in good agreement with Wood solution at $R_f = 0.5$ and 1.5 and M-O solution at $R_f = 3$ and 5 .

The distances of application point to the base are smaller than those suggested by Seed and Whitman and Wood solutions resulting in relatively lower bending moments at the base.

There is reasonable similarity between the results obtained from analyses of linear elastic and elasto-plastic backfill except for the resonance case.

The total lateral stress distributions at the backfill corresponding to the maximum total lateral thrust are presented in Figures 4.2.2.11, 4.2.2.12 and 4.2.2.13. Similar to the gravity wall case, the total lateral stress falls below the static lateral stress at some points which makes it impracticable to separately examine the application point of the dynamic lateral thrust.

Maximum total lateral thrusts are summarized in Table 4.2.2.1. A summary of the maximum dynamic lateral thrusts are given in Table 4.2.2.2.

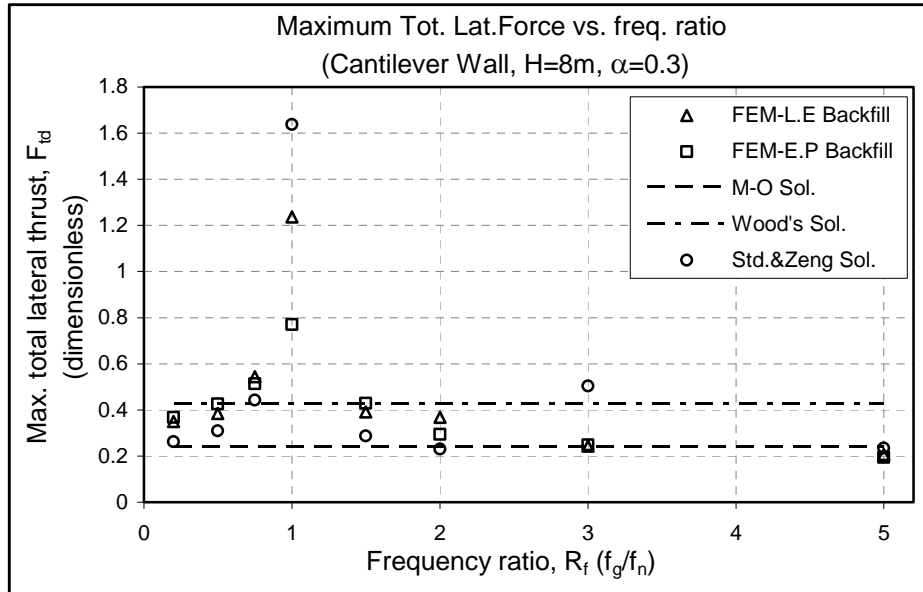


Figure 4.2.2.8 Maximum total lateral force vs. frequency ratio for cantilever wall (H=8m, $\alpha=0.3$)

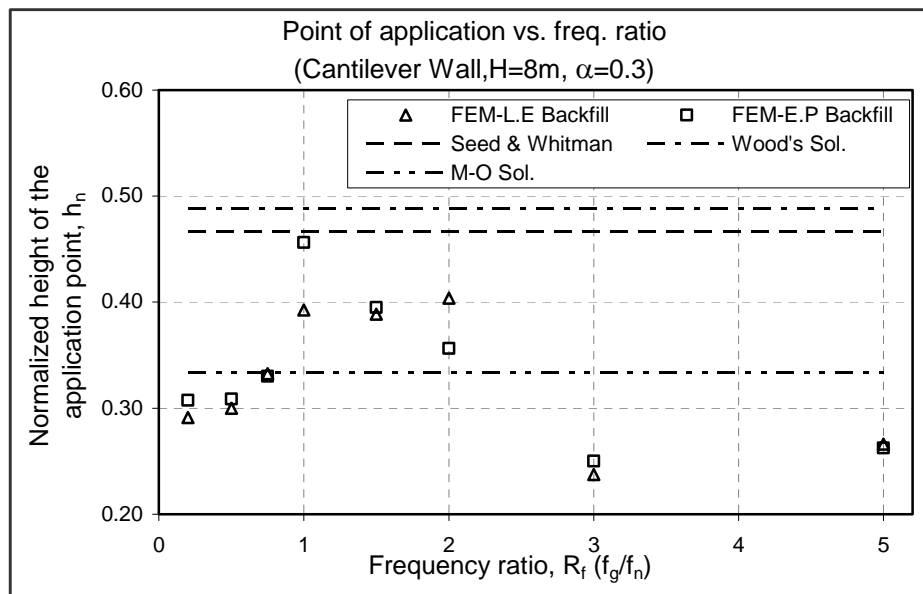


Figure 4.2.2.9 Distance of the point of application vs. frequency ratio for cantilever wall (H=8m, $\alpha=0.3$)

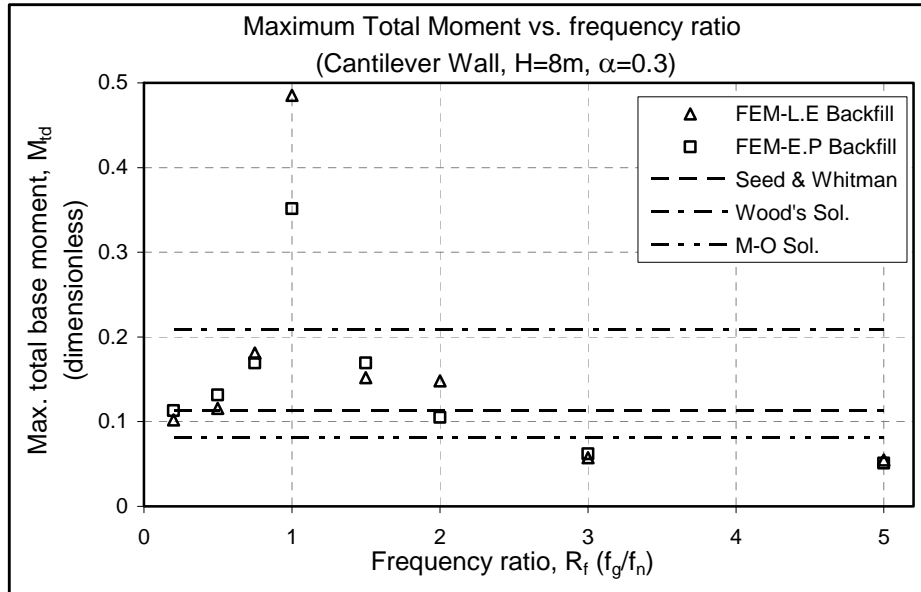


Figure 4.2.2.10 Maximum total moment vs. frequency ratio for cantilever wall ($H=8m$, $\alpha=0.3$)

Table 4.2.2.1 Summary of the results for cantilever wall

Freq. ratio (R_f)	Backfill material model	Total lat. force, F_t (kN)	Total base moment, M_t (kNm)	Height of application point, h	Non-dimensional total lat. force, F_{td}	Non-dimensional total base moment, M_{td}	Normalized height of app. point, h_n
0.2	L.E	396	923	2.33	0.350	0.102	0.29
0.2	E-P	415	1021	2.46	0.367	0.113	0.31
0.5	L.E	435	1044	2.4	0.385	0.115	0.30
0.5	E-P	481	1188	2.47	0.426	0.131	0.31
0.75	L.E	615	1636	2.66	0.544	0.181	0.33
0.75	E-P	580	1531	2.64	0.513	0.169	0.33
1	L.E	1397	4387	3.14	1.236	0.485	0.39
1	E-P	871	3179	3.65	0.771	0.352	0.46
1.5	L.E	442	1375	3.11	0.391	0.152	0.39
1.5	E-P	484	1529	3.16	0.428	0.169	0.40
2	L.E	415	1340	3.23	0.367	0.148	0.40
2	E-P	333	949	2.85	0.295	0.105	0.36
3	L.E	274	521	1.9	0.242	0.058	0.24
3	E-P	281	562	2	0.249	0.062	0.25
5	L.E	233	496	2.13	0.206	0.055	0.27
5	E-P	220	462	2.1	0.195	0.051	0.26

Table 4.2.2.2 Dynamic lateral force results for cantilever wall

Freq. ratio (R_f)	Backfill material model	Static lat. force, F_{sta} (kN)	Total lat. force, F_t (kN)	Dynamic lat. force, F_d (kN)	Non-dimensional dynamic lat. force, F_{dd}
0.2	L.E	201	396	195	0.58
0.2	E-P	206	415	209	0.62
0.5	L.E	201	435	234	0.69
0.5	E-P	206	481	275	0.81
0.75	L.E	201	615	414	1.22
0.75	E-P	206	580	374	1.10
1	L.E	201	1397	1196	3.53
1	E-P	206	871	665	1.96
1.5	L.E	201	442	241	0.71
1.5	E-P	206	484	278	0.82
2	L.E	201	415	214	0.63
2	E-P	206	333	127	0.37
3	L.E	201	274	73	0.22
3	E-P	206	281	75	0.22
5	L.E	201	233	32	0.09
5	E-P	206	220	14	0.04

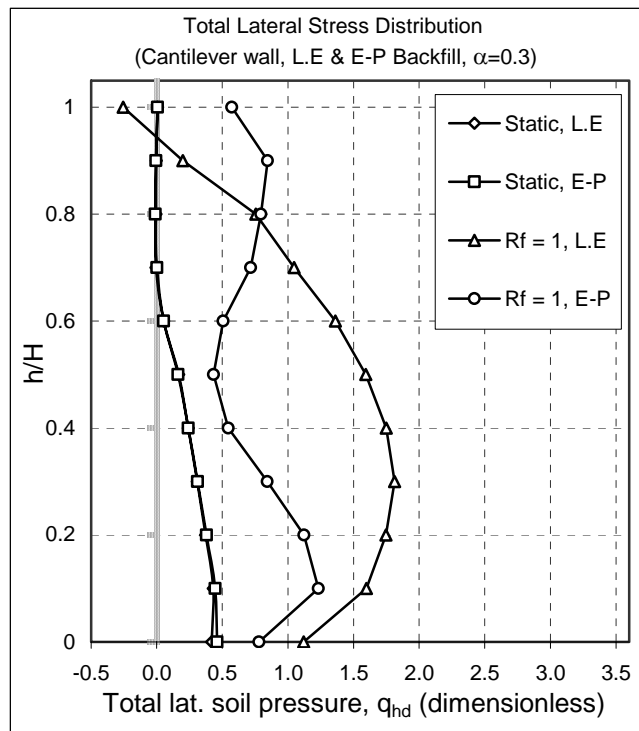


Figure 4.2.2.11 Total lateral stress distribution for max. thrust for the resonance case ($\alpha=0.3$, Cantilever wall, $H=8m$)

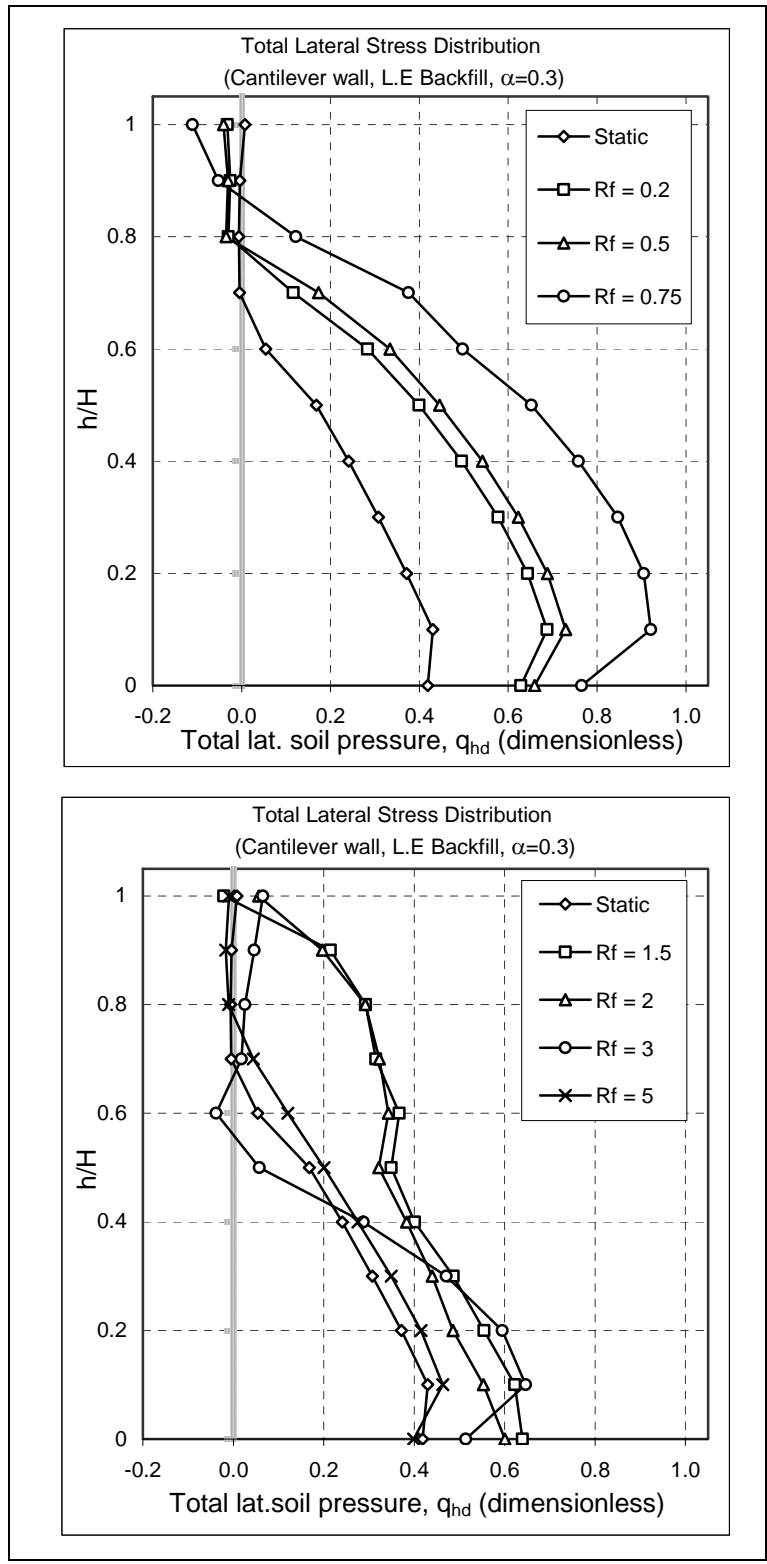


Figure 4.2.2.12 Total lateral stress distributions for max. thrust for various freq. ratios ($\alpha=0.3$, Cantilever wall, $H=8m$)

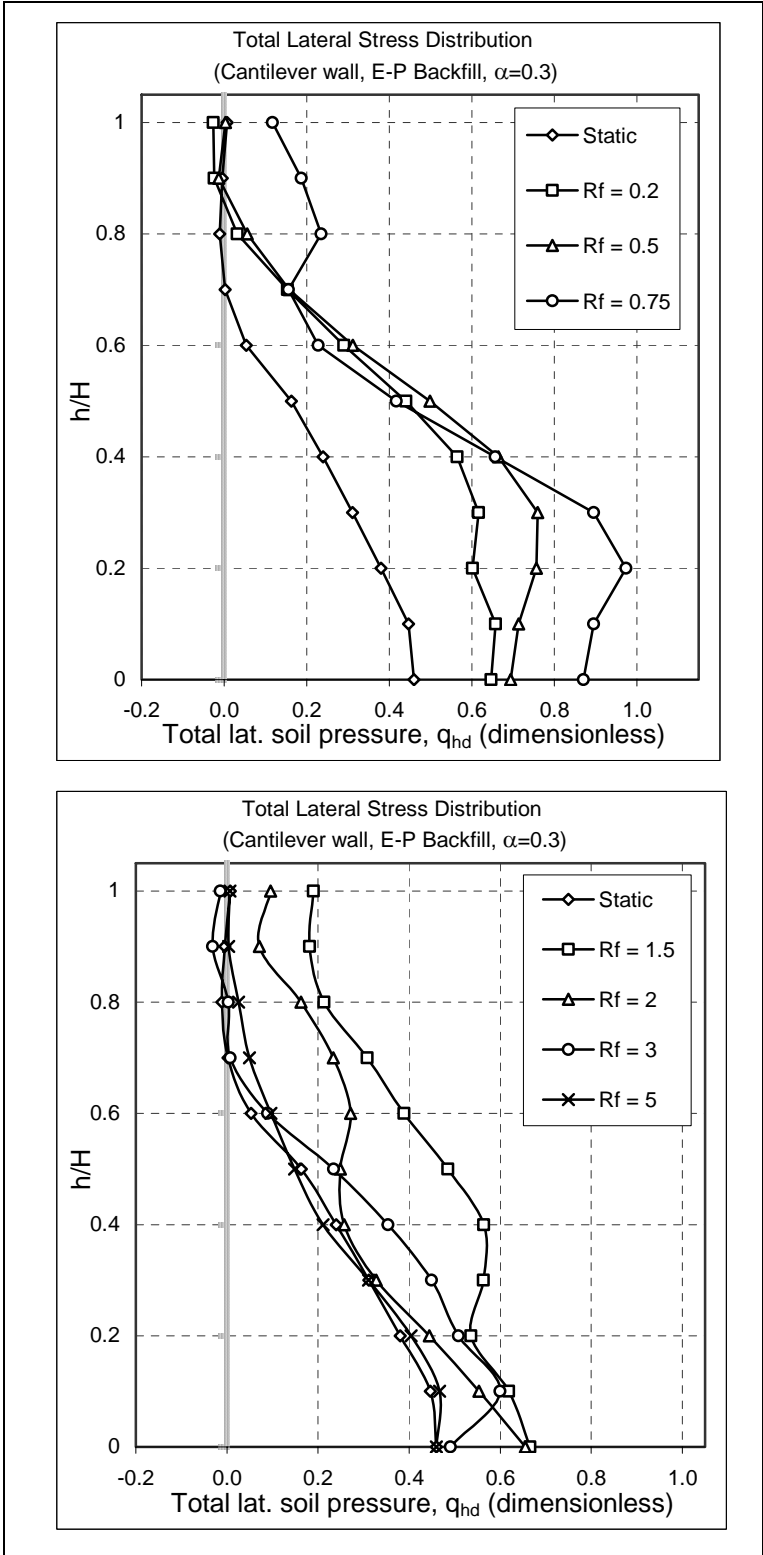


Figure 4.2.2.13 Total lateral stress distributions for max. thrust for various freq. ratios ($\alpha=0.3$, Cantilever wall, $H=8\text{m}$)

4.3 Analyses with real earthquake records

The dynamic response of a typical gravity and a cantilever wall subjected to harmonic base motions have been examined in Sections 4.2 and 4.3. In this section, the dynamic behaviour of the walls when subjected to actual earthquake motions are investigated. For this purpose, the same soil-wall systems are considered and real earthquake records are used as base motions in the analyses.

4 earthquake records with different frequency content and similar peak ground accelerations are considered. Information about the earthquake records and simplified frequency content parameters are given in Table 4.3.1. The simplified frequency content parameters examined are: the predominant frequency, f_p ; the smoothed spectral predominant frequency, f_0 ; and the mean frequency, f_m as suggested by Rathje et al (1998).

The predominant frequency, f_p is defined as the frequency corresponding to the peak spectral acceleration in the acceleration response spectrum.

The smoothed spectral predominant frequency, f_0 is given by:

$$f_0 = \frac{\sum_{i=1}^{nPer} \ln[S_a(T_i)] H[S_a(T_i) - 1.2MHA]}{\sum_{i=1}^{nPer} T_i \ln[S_a(T_i)] H[S_a(T_i) - 1.2MHA]} \quad (4.10)$$

where; $nPer$ = number of periods in the response spectrum,

T_i = discrete periods in the response spectrum,

$S_a(T_i)$ = spectral acceleration at period T_i ,

$H[x]$ = the Heaviside function (equals 1 when $x > 0$ and 0 for $x < 0$).

The mean frequency, f_m is defined as:

$$f_m = \frac{\sum C_i^2}{\sum C_i^2 \left(\frac{1}{f_i} \right)} \quad \text{for } 0.25 \text{ Hz} \leq f_i \leq 20 \text{ Hz} \quad (4.11)$$

where; C_i = Fourier amplitudes of the accelerogram,
 f_i = Discrete Fourier transform frequency.

The acceleration time histories and the acceleration response spectra of the earthquake motions are shown in Figure 4.3.1 and 4.3.2 respectively.

Using the whole earthquake record in the analysis leads to very large output data and time consumption. Since the goal is to examine the maximum lateral pressures, a part of these records are used which contain the maximum acceleration with a total duration of not less than 10 seconds.

Table 4.3.1 Summary of the earthquake records

Ground motion	EQ1	EQ2	EQ3	EQ4
Earthquake name	San Fernando 1971	Düzce 1999	Loma Prieta 1989	Loma Prieta 1989
Station	128 Lake Hughes #12	Düzce	Saratoga W Valley Coll.	1002 Apeel 2 Redwood City
Peak acc. (g)	0.27	0.3	0.33	0.27
Peak spectral acc. (g)	1.32	1.82	0.75	1.18
f_p (1/s)	4.17	2.5	3.84	0.91
f_0 (1/s)	6.23	3.15	4.33	1.57
f_m (1/s)	4.64	1.46	1.03	0.99
f_p / f_n	1.74	1.04	1.60	0.38
f_0 / f_n	2.60	1.31	1.80	0.65
f_m / f_n	1.93	0.61	0.43	0.41

The results obtained from the analyses of gravity and cantilever walls are summarized in Tables 4.3.2 to 4.3.5.

The variation of the total lateral thrust with time for different base motions are shown in Figures 4.3.3 and 4.3.4 for gravity and cantilever walls respectively.

Table 4.3.2 Summary of the results for real earthquake motions
(Gravity wall, H=8m)

Ground Motion	Backfill material model	Max. total lat. force, F_t (kN)	Max. total base moment, M_t (kNm)	Height of application point, h	Non-dimensional total lat. force, F_{td}	Non-dimensional total base moment, M_{td}	Normalized height of app. point, h_n
EQ1	L.E	330	858	2.6	0.292	0.095	0.33
EQ1	E-P	323	930	2.88	0.286	0.103	0.36
EQ2	L.E	1406	5413	3.85	1.244	0.599	0.48
EQ2	E-P	1333	5185	3.89	1.180	0.574	0.49
EQ3	L.E	404	1010	2.5	0.357	0.112	0.31
EQ3	E-P	374	1047	2.8	0.331	0.116	0.35
EQ4	L.E	327	818	2.5	0.289	0.090	0.31
EQ4	E-P	311	846	2.72	0.275	0.094	0.34

Table 4.3.3 Dynamic lateral force results for real earthquake motions
(Gravity wall, H=8m)

Ground Motion	Peak acc. (g)	Backfill material model	Static lat. force, F_{sta} (kN)	Total lat. force, F_t (kN)	Dynamic lat. force, F_d (kN)	Non-dimensional dynamic lat. force, F_{dd}
EQ1	0.27	L.E	171	330	159	0.52
EQ1	0.27	E-P	174	323	149	0.49
EQ2	0.3	L.E	171	1406	1235	3.64
EQ2	0.3	E-P	174	1333	1159	3.42
EQ3	0.33	L.E	171	404	233	0.62
EQ3	0.33	E-P	174	374	200	0.54
EQ4	0.27	L.E	171	327	156	0.51
EQ4	0.27	E-P	174	311	137	0.45

Table 4.3.4 Summary of the results for real earthquake motions
(Cantilever wall, H=8m)

Ground Motion	Backfill material model	Max. total lat. force, F_t (kN)	Max. total base moment, M_t (kNm)	Height of application point, h	Non-dimensional total lat. force, F_{td}	Non-dimensional total base moment, M_{td}	Normalized height of app. point, h_n
EQ1	L.E	439	1146	2.61	0.388	0.127	0.33
EQ1	E-P	455	1356	2.98	0.403	0.150	0.37
EQ2	L.E	975	2711	2.78	0.863	0.300	0.35
EQ2	E-P	897	3516	3.92	0.794	0.389	0.49
EQ3	L.E	530	1367	2.58	0.469	0.151	0.32
EQ3	E-P	543	1450	2.67	0.480	0.160	0.33
EQ4	L.E	438	1060	2.42	0.388	0.117	0.30
EQ4	E-P	448	1245	2.78	0.396	0.138	0.35

Table 4.3.5 Dynamic lateral force results for real earthquake motions
(Cantilever wall, H=8m)

Ground Motion	Peak acc. (g)	Backfill material model	Static lat. force, F_{sta} (kN)	Total lat. force, F_t (kN)	Dynamic lat. force, F_d (kN)	Non-dimensional dynamic lat. force, F_{dd}
EQ1	0.27	L.E	201	439	238	0.78
EQ1	0.27	E-P	206	455	249	0.82
EQ2	0.3	L.E	201	975	774	2.28
EQ2	0.3	E-P	206	897	691	2.04
EQ3	0.33	L.E	201	530	329	0.88
EQ3	0.33	E-P	206	543	337	0.90
EQ4	0.27	L.E	201	438	237	0.78
EQ4	0.27	E-P	206	448	242	0.79

Comparing the results of the analyses using real earthquake records (summarized in Tables 4.3.1 to 4.3.5) and harmonic motions (summarized in Tables 4.1.2.1, 4.1.2.2, 4.2.2.1 and 4.2.2.2) the following conclusions can be made:

- The total lateral thrusts and their application points obtained by using real earthquake records are close to those obtained by harmonic base motions.
- As far as the maximum total lateral forces acting on the wall are considered, it can be said that none of the proposed parameters to represent the frequency

content of the earthquake motions, f_p , f_0 or f_m can be used as the frequency of an equivalent harmonic motion with same peak acceleration to represent the earthquake alone.

- Examining the results for the maximum total lateral thrust and its point of application, it can be stated that the results of EQ1, EQ2 and EQ4 motions are in reasonably good agreement with those obtained by utilizing harmonic base motions with a frequency of f_p . For EQ3 motion, the results are in reasonably good agreement with those calculated by using harmonic base motion with a frequency of f_m .

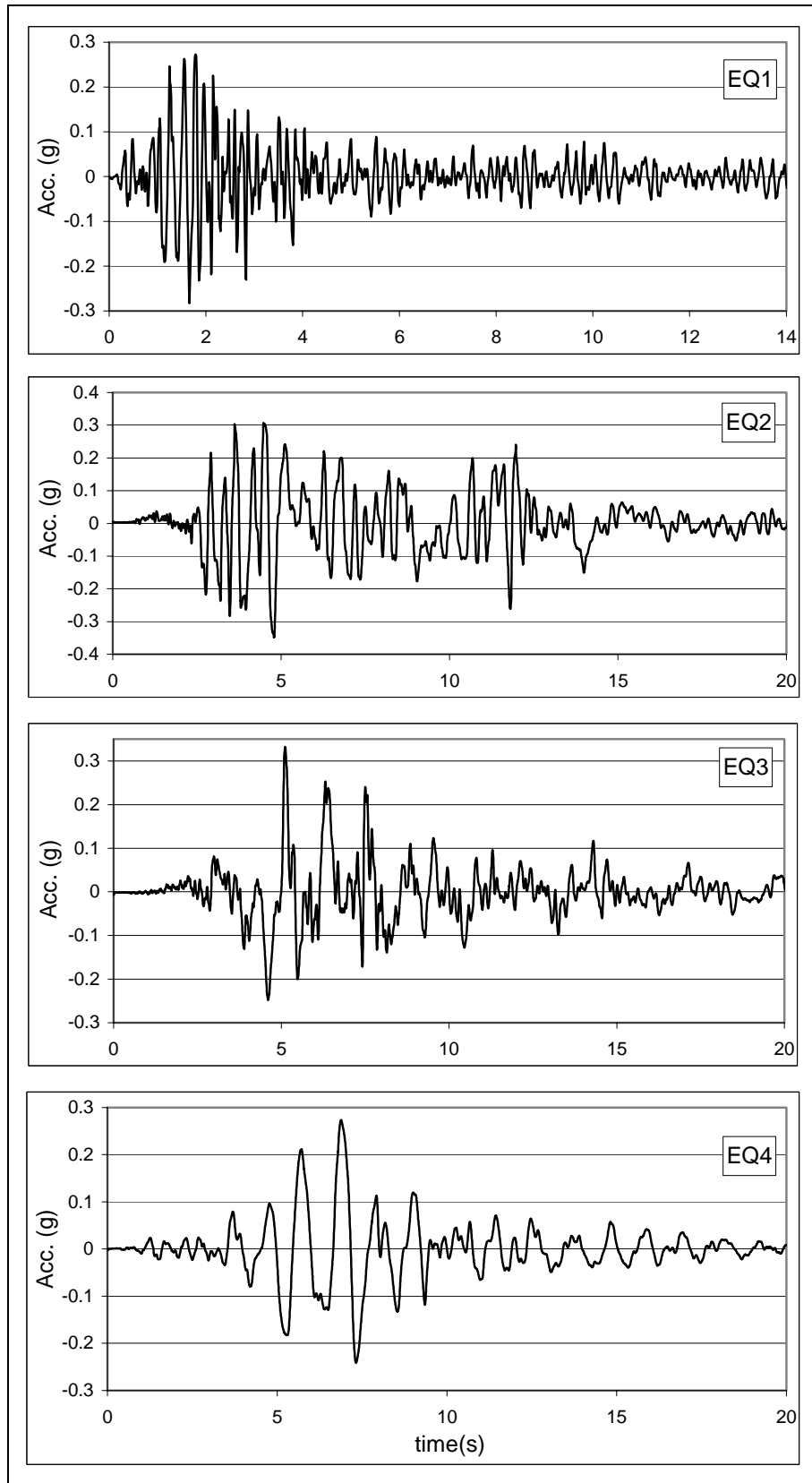


Figure 4.3.1 Time histories of the earthquake records used

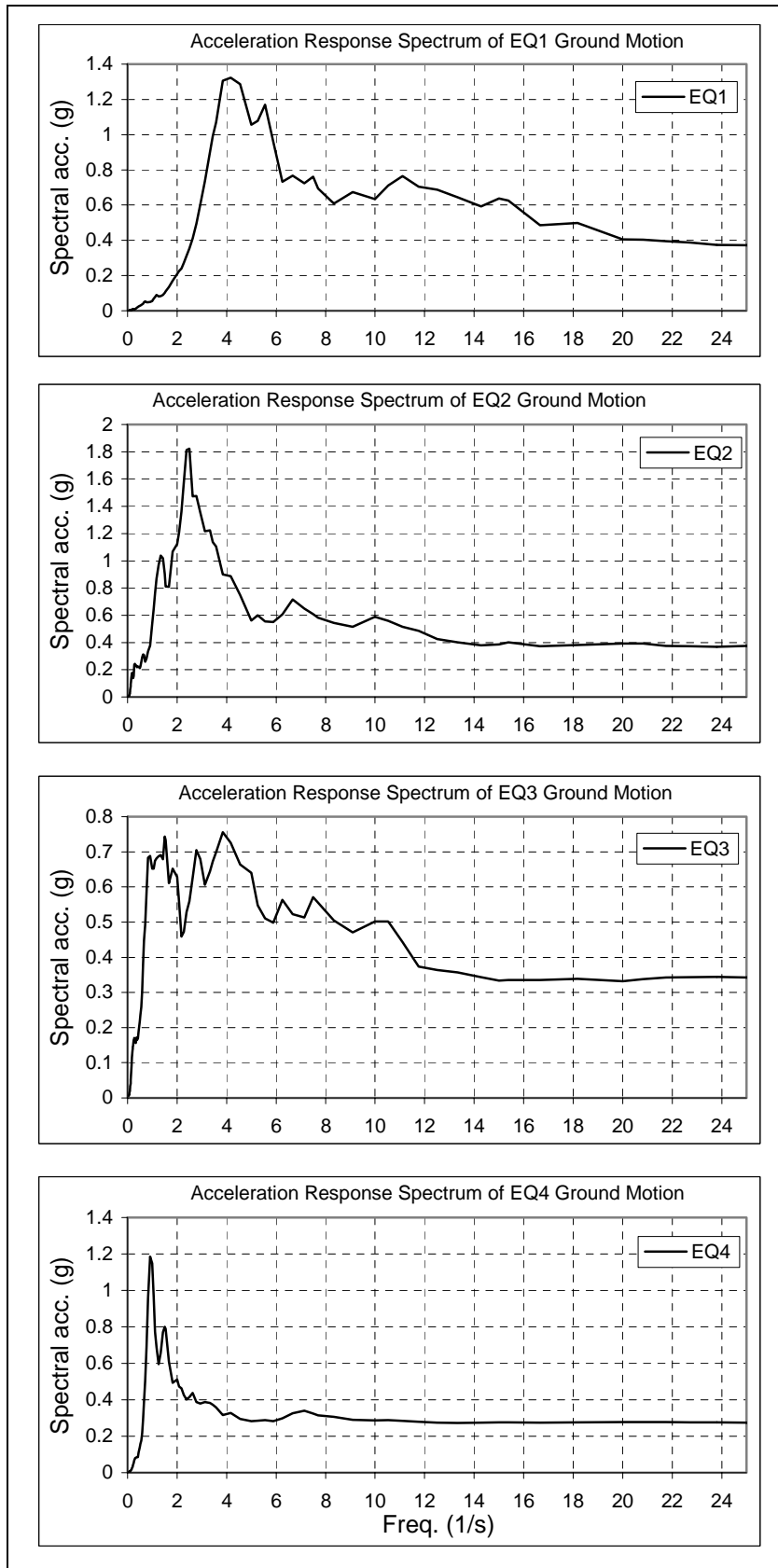


Figure 4.3.2 Acceleration response spectra of earthquake motions

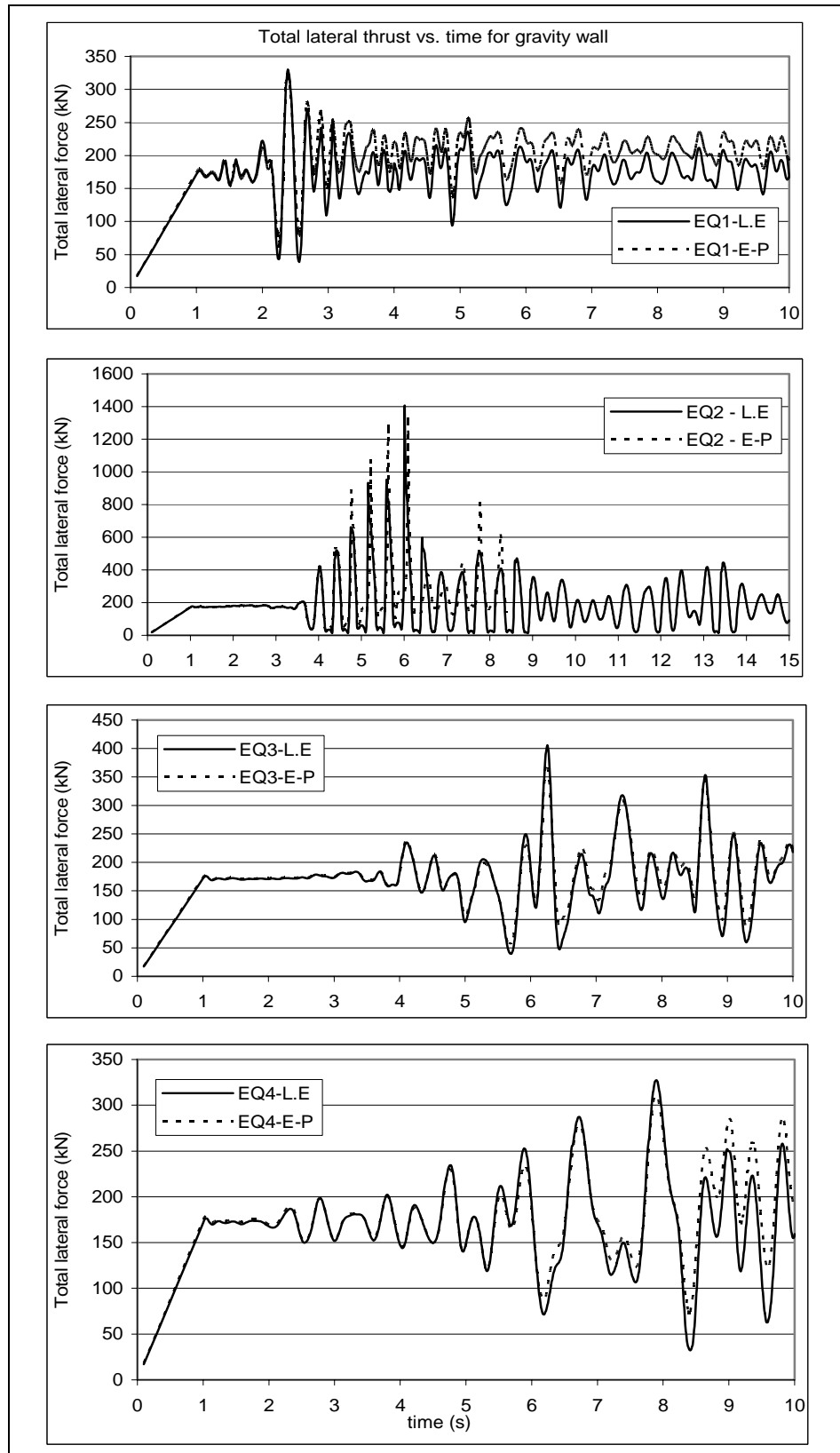


Figure 4.3.3 Total lateral force vs. time for real earthquake motions (Gravity wall, H=8m)

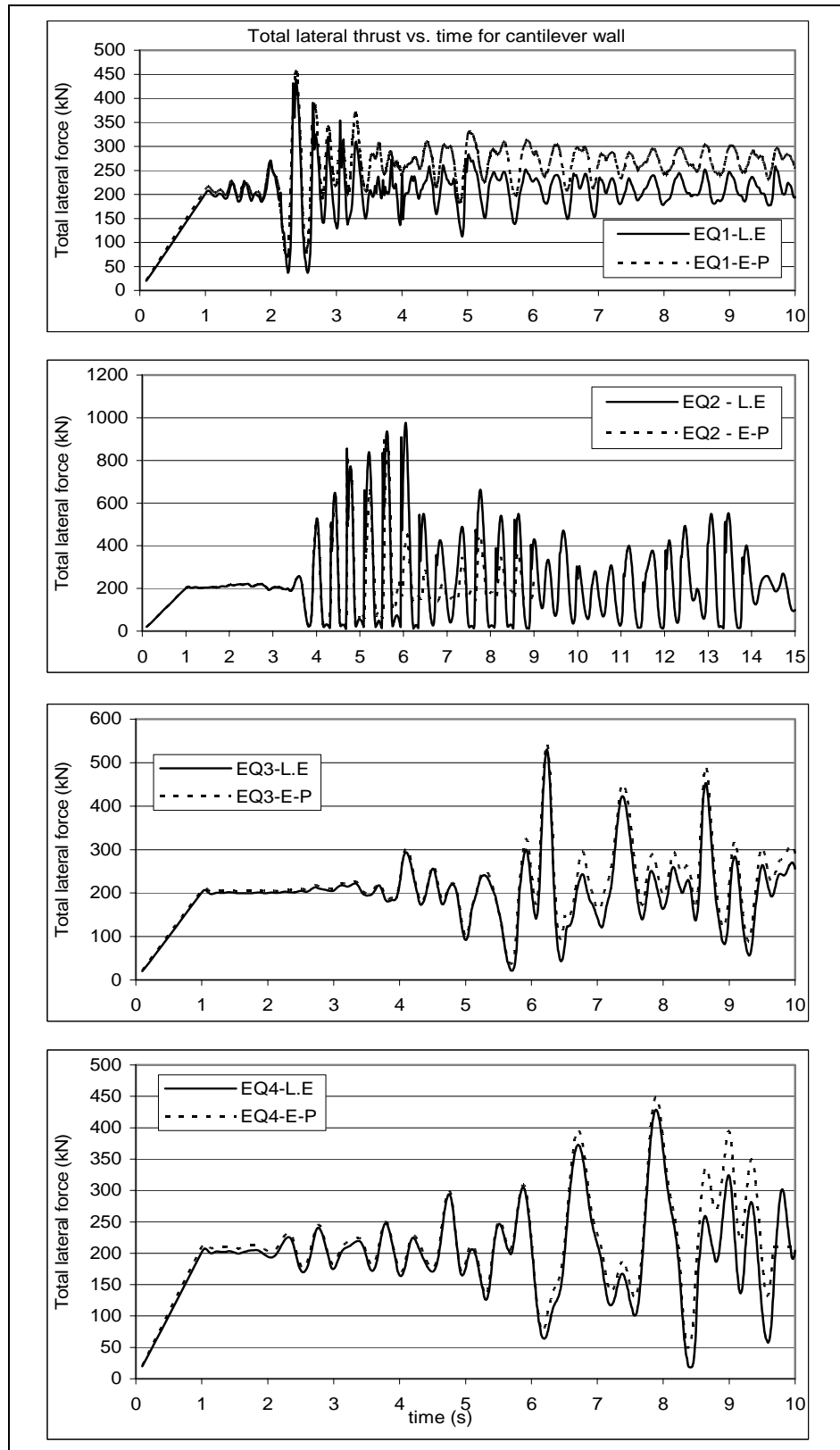


Figure 4.3.4 Total lateral force vs. time for real earthquake motions (Cantilever wall, H=8m)

CHAPTER 5

FINITE ELEMENT ANALYSES FOR 5 METER HIGH WALL RESTING ON ELASTO-PLASTIC FOUNDATION SOIL

Analyses and results of 8m high gravity and cantilever walls subjected to harmonic and real earthquake base motions have been presented in Chapter 4. Harmonic base motions of constant peak acceleration (0.3g) with different frequencies and strong motion acceleration time histories having similar peak acceleration values (0.27g-0.33g) with different frequency content are used in the analyses. The foundation soil is assumed as linear elastic and elasto-plastic material model is used for backfill.

In this chapter, typical gravity and cantilever walls of 5m high are considered. Dynamic response of the walls when subjected to harmonic and recorded real earthquake base motions with various peak accelerations and frequency content are examined. Both the foundation and backfill soil are assumed to be elasto-plastic material in the analyses.

The dimensions of the walls are assessed by Mononobe-Okabe method using the peak base accelerations. The factor of safety (F.S) values are assumed to be 1.5 and 2.0 for sliding and overturning respectively for static case. For dynamic cases, the factor of safety values are decreased to 75% of assumed for static case. Therefore the F.S values for dynamic loading are assumed to be 1.12 and 1.5 for sliding and overturning respectively.

5.1 Gravity wall

This section presents the analyses and results of a typical gravity retaining wall of 5m high subjected to harmonic base motions with varying magnitude and frequency.

5.1.1 The model and the parameters

The typical soil-wall system used in the analyses has been shown in Figure 4.1.1.1. The wall is resting on a foundation soil layer that is underlain by a rigid base which is fixed in the vertical direction and subjected to the base motion in the horizontal direction. Information about the model, boundary conditions and loading is given in Section 4.1.1.

An elastic-perfect plastic material model with Drucker-Prager yield criterion is used for both the foundation and backfill soil. The damping ratio of the system is assumed to be 5% and Rayleigh damping is utilized with appropriate damping parameters as explained in Section 3.2.2 for each loading case.

Harmonic base motions (defined by Equation 4.1) with varying peak accelerations of 0.1g, 0.2g, 0.3g and varying frequency ratios of: $R_f = 0.2, 0.5, 2, 5$ are used in the analyses. R_f is the ratio of the base motion frequency to the fundamental frequency of the soil layer defined by Equation 4.3 as:

$$R_f = f_g/f_n \quad (4.3)$$

The model dimensions and parameters are given in Table 5.1.1.1. As stated before, the wall dimensions are determined considering the sliding and overturning of the wall using Mononobe-Okabe method. The peak base acceleration of the soil-wall system (peak acceleration of the motion applied along the base of underlying soil beneath the foundation) is used to assess the seismic coefficient, k_h . The passive

resistance of the soil in front of the wall is neglected in the assessment of wall dimensions.

As explained in Section 4.1.1, the base motion, hence the dynamic loading starts at $t=1$ seconds, after the static stresses and deformations are reached.

Table 5.1.1.1 Dimensions and material parameters considered in the gravity wall analyses

Symbol	Description	Unit	Value
H	Height of the wall	m	5
D	Foundation layer thickness	m	5.5
D _w	Wall foundation depth	m	1
B1	Wall dimensions for peak base acc. of 0.1g	m	1
B2		m	2
B1	Wall dimensions for peak base acc. of 0.2g	m	1.5
B2		m	2.5
B1	Wall dimensions for peak base acc. of 0.3g	m	2
B2		m	3
ρ_s	Density of soil	t/m ³	1.8
E _s	Elasticity mod. of soil	kPa	80 000
ν_s	Poisson's ratio of soil	-	0.33
V _s	Shear wave velocity of soil	m/s	129
c	Drucker-Prager parameters (For E-P analysis)	kPa	0
ϕ		degree	33
ρ_w	Density of the wall	t/m ³	2.4
E _w	Elasticity mod. of the wall	kPa	25 x 10 ⁶
ν_w	Poisson's ratio of the wall	-	0.2

5.1.2 The results and comparisons

Acceleration amplitudes and frequency ratios utilized during the calculations has been presented in Section 5.1.1. For each time step, the total lateral thrust and base moment values are found by integrating the lateral stresses on the wall, and the

maximum total (static+dynamic) lateral thrust and its point of application are determined for each loading. Tensile stresses are not considered since the wall and backfill are separated at this stage and no force is exerted on the wall.

The dynamic behaviour of the gravity retaining wall is illustrated on the Figures 5.1.2.1 and 5.1.2.2 where the deformed mesh at different instants are shown. The deformations are magnified by 100 times in the figures. It is observed that the stiff wall rotates considerably lateral pressures decrease for the walls and soil configurations and range of frequency of the base excitations used in the calculations.

The Drucker-Prager parameters are selected to be $c=0$ and $\phi=33$ as given in Table 5.1.1.1. However, in the elasto-plastic analyses with peak base acceleration of 0.3g and frequency ratios of 0.5 and 2, due to the large accelerations and complex contact behaviour, convergence difficulties are encountered and the cohesion value is increased up to 20 kPa for some of the soil elements at the near-bottom of the wall as indicated by “x” marks in Figure 5.1.2.1 to achieve convergence.

The variation of maximum total lateral thrust with peak acceleration of the base motion is depicted in Figure 5.1.2.3. The static lateral force (corresponding to $\alpha=0$) is also shown in the figure. The increase in the maximum lateral thrust with the base acceleration amplitude is approximately linear as can be seen in this figure. There is a considerable difference between the static lateral force found by finite element method and Coulomb's Earth Pressure Theory for static loading, which contributes to the difference between the total lateral force results.

The height of the application point of the total lateral thrust are given in Figure 5.1.2.4. The results are generally between those suggested by M-O and Seed and Whitman (1970).

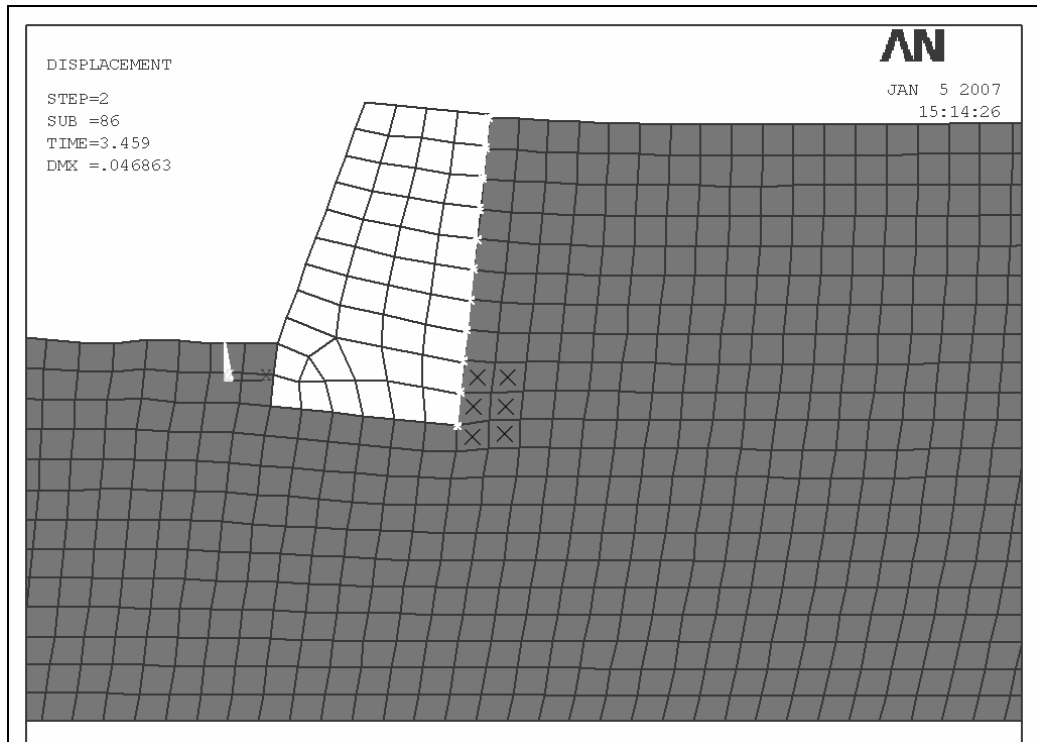


Figure 5.1.2.1 Deformed mesh for the gravity wall
 (H=5m, $\alpha=0.3$, $R_f=0.5$, t=3.459 s.)

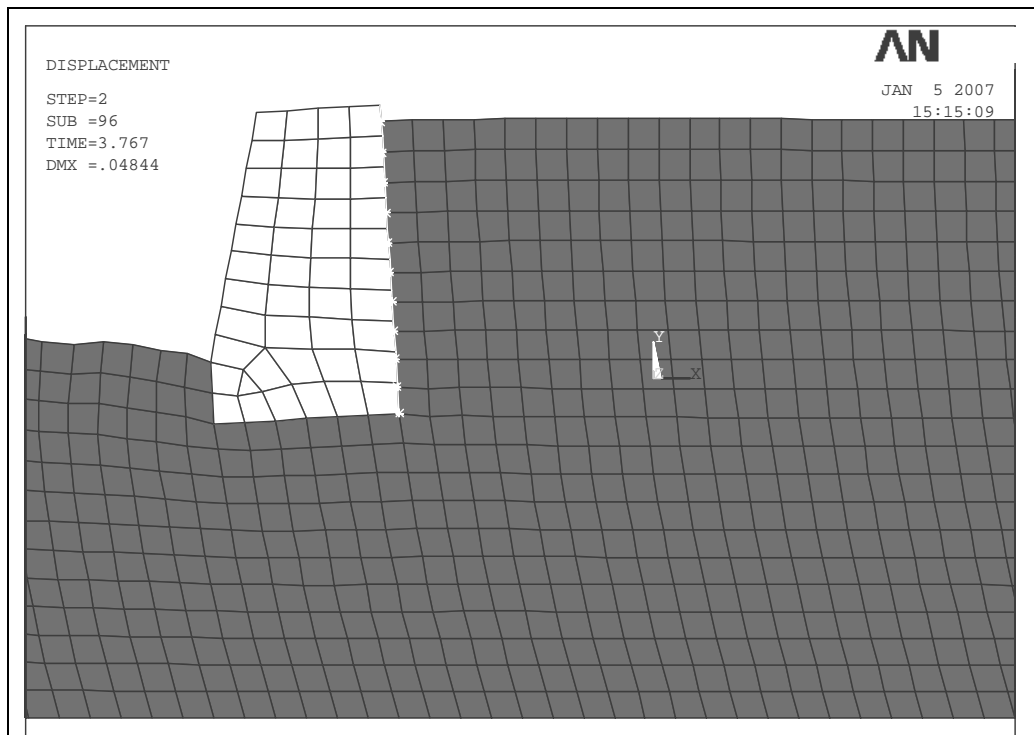


Figure 5.1.2.2 Deformed mesh for the gravity wall
 (H=5m, $\alpha=0.3$, $R_f=0.5$, t=3.767 s.)

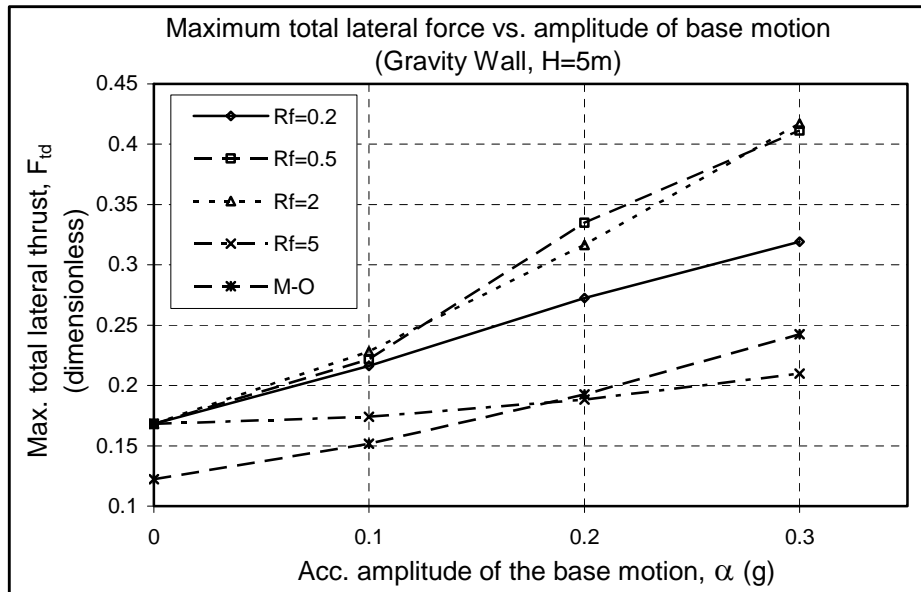


Figure 5.1.2.3 Maximum total lateral force vs. amplitude of base motion (Gravity wall, H=5m)

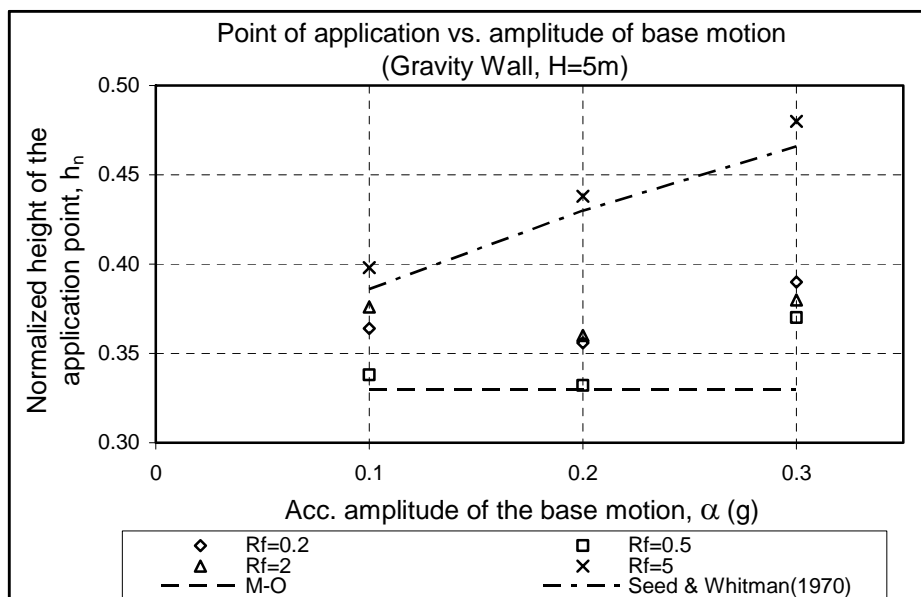


Figure 5.1.2.4 Height of the application point of the total lateral force vs. amplitude of base motion (Gravity wall, H=5m)

Figure 5.1.2.5 depicts the maximum total moments at the base versus base motion acceleration amplitudes. The finite element results are generally higher than M-O and Seed and Whitman (1970) methods. Nevertheless, it can be seen that the

difference is mainly due to the difference between static solution by finite element method and Coulomb's solution (on which M-O and Seed and Whitman methods are based).

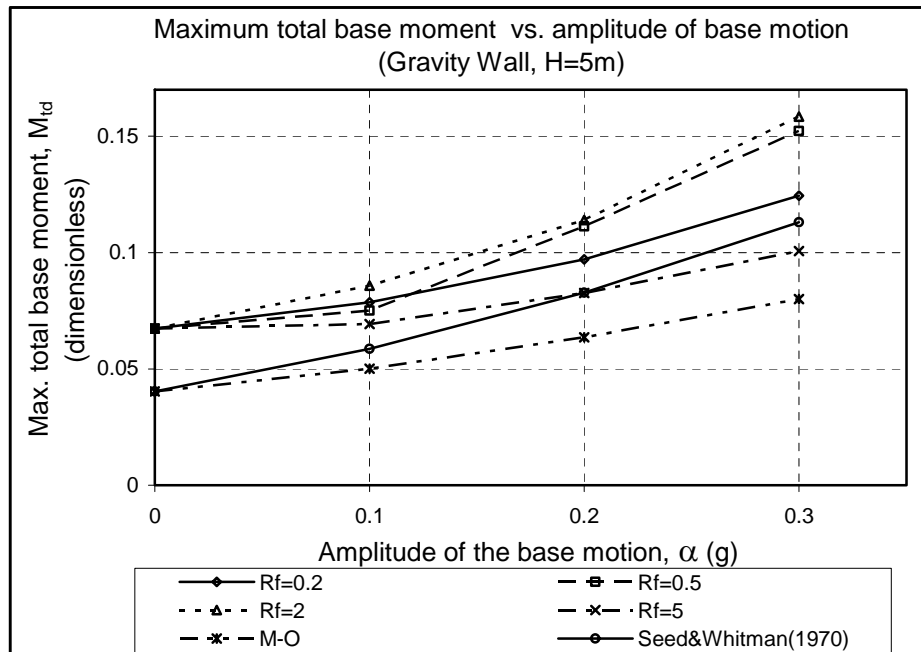


Figure 5.1.2.5 Maximum total base moment vs. amplitude of base motion (Gravity wall, H=5m)

The variation of the maximum thrust with frequency ratio are given through Figure 5.1.2.6 to 5.1.2.8 for different base motion amplitudes. Mononobe-Okabe, Steedman and Zeng and Wood solutions are also included in the figures. The finite element results seem to be between those suggested by M-O and Wood approaches. The maximum lateral thrust increases as the frequency of the base motion approaches the fundamental frequency of the soil layer.

In the calculations using Steedman and Zeng approach, the amplification of the accelerations between the base of the wall and the soil surface is assumed to be equal to the amplification between the base of the model and the soil surface. This is the main reason of the significant difference between finite element and Steedman and Zeng results.

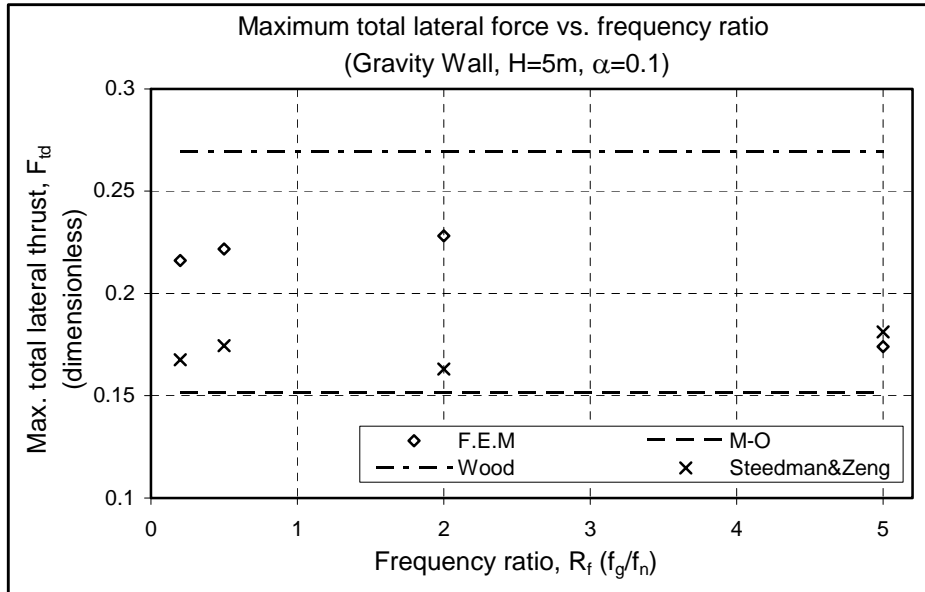


Figure 5.1.2.6 Maximum total lateral force vs. frequency ratio
(Gravity wall, H=5m, $\alpha = 0.1$)

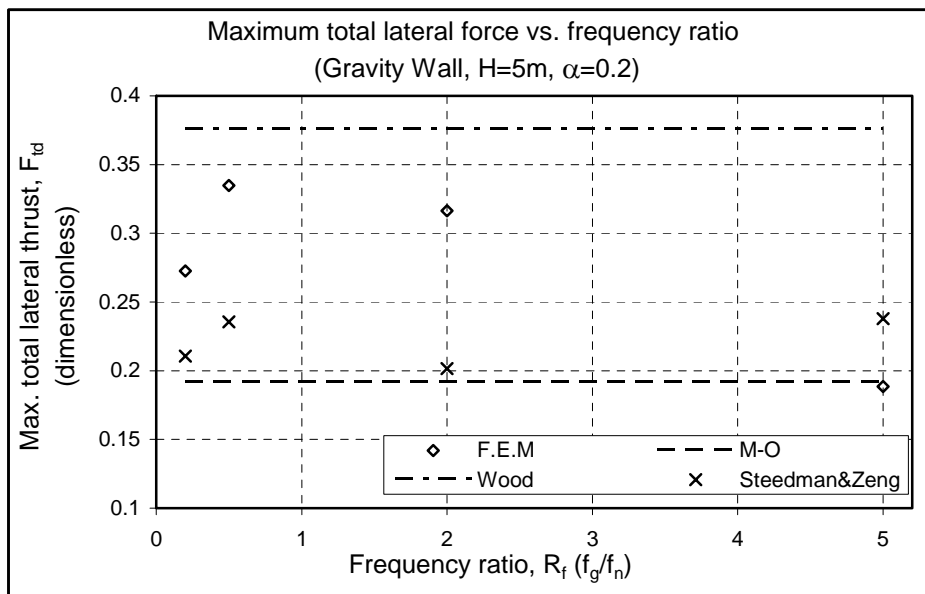


Figure 5.1.2.7 Maximum total lateral force vs. frequency ratio
(Gravity wall, H=5m, $\alpha = 0.2$)

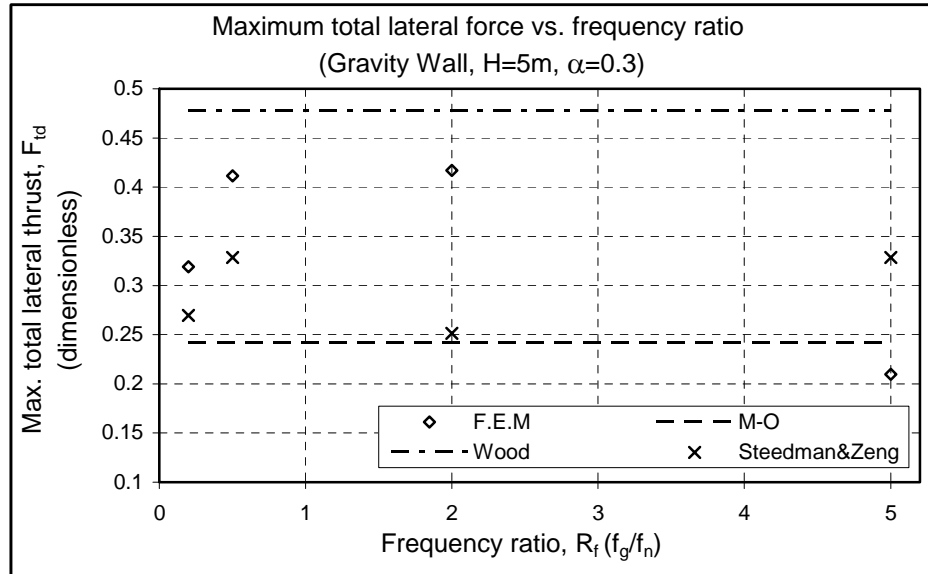


Figure 5.1.2.8 Maximum total lateral force vs. frequency ratio (Gravity wall, H=5m, $\alpha = 0.3$)

The result of the analyses for harmonic base motions are summarized in Tables 5.1.2.1 and 5.1.2.2. The non-dimensional parameters in the tables, F_{td} , h_n , M_{td} and F_{dd} defined by Equations 4.5, 4.6, 4.7 and 4.9 respectively in Section 4.1.2 are provided in the tables.

Table 5.1.2.1 Summary of the results for gravity wall

Acc. amplitude of base motion (g)	Freq. ratio (R_f)	Total lat. force, F_t (kN)	Total base moment, M_t (kNm)	Height of application point, h	Non-dimensional total lat. force, F_{td}	Non-dimensional total base moment, M_{td}	Normalized height of app. point, h_n
0.1	0.2	95	174	1.82	0.216	0.079	0.36
0.1	0.5	98	165	1.69	0.222	0.075	0.34
0.1	2	101	189	1.88	0.228	0.086	0.38
0.1	5	77	153	1.99	0.174	0.069	0.40
0.2	0.2	120	214	1.78	0.273	0.097	0.36
0.2	0.5	148	245	1.66	0.335	0.111	0.33
0.2	2	140	251	1.80	0.316	0.114	0.36
0.2	5	83	182	2.19	0.188	0.083	0.44
0.3	0.2	141	275	1.95	0.319	0.124	0.39
0.3	0.5	182	336	1.85	0.411	0.152	0.37
0.3	2	184	350	1.90	0.417	0.158	0.38
0.3	5	93	222	2.40	0.210	0.101	0.48
$F_{td} = F_t / (\gamma H^2)$			$M_{td} = M_t / (\gamma H^3)$		$h_n = h / H$		

Table 5.1.2.2 Maximum dynamic lateral force results for gravity wall

Acc. amplitude of base motion (g)	Freq. ratio (R_f)	Static lat. force, F_{sta} (kN)	Total lat. force, F_t (kN)	Dynamic lat. force, F_d (kN)	Non-dimensional dynamic lat. force, F_{dd}
0.1	0.2	74	95	21	0.48
0.1	0.5	74	98	24	0.54
0.1	2	74	101	27	0.60
0.1	5	74	77	3	0.06
0.2	0.2	76	120	44	0.50
0.2	0.5	76	148	72	0.81
0.2	2	76	140	64	0.72
0.2	5	76	83	7	0.08
0.3	0.2	76	141	65	0.49
0.3	0.5	76	182	106	0.80
0.3	2	76	184	108	0.82
0.3	5	76	93	17	0.13
$F_{dd} = F_d / (\rho_s a_p H^2)$					

Table 5.1.2.3 presents the dynamic lateral forces obtained by Mononobe-Okabe and Wood methods.

Table 5.1.2.3 Maximum dynamic lateral forces by M-O and Wood's solutions

Peak acc. (g)	Solution method	Dynamic lat. force, F_d (kN)	Non-dimensional dynamic lat. force, F_{dd}
0.1	M-O	13	0.29
0.2	M-O	31	0.35
0.3	M-O	53	0.40
0.4	M-O	85	0.48
0.5	M-O	133	0.60
all	Wood	all	1.00

The variation of the maximum dynamic lateral force with the amplitude of the base motion is shown in Figure 5.1.2.9. It can be seen that the finite element results are generally between those of M-O and Wood approaches as was the case for the total lateral force results.

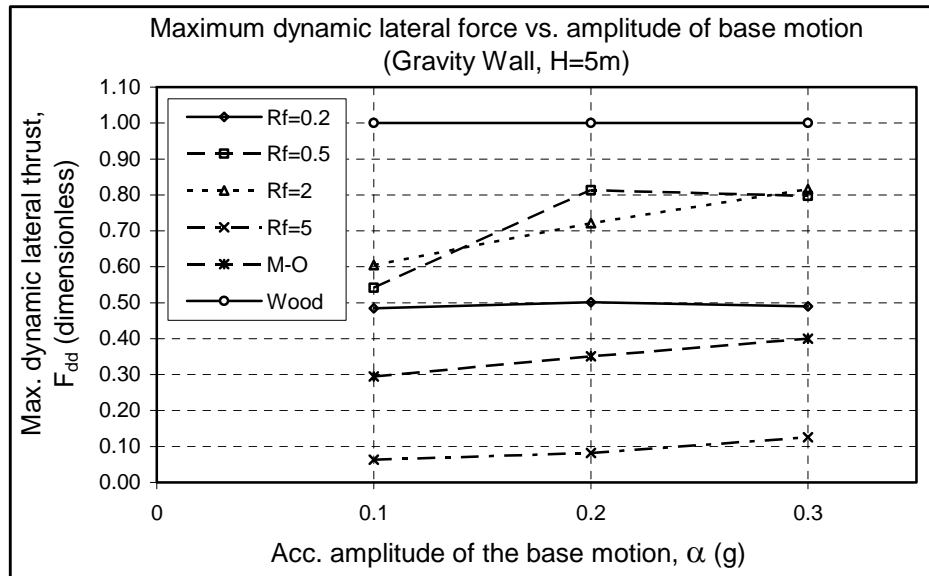


Figure 5.1.2.9 Maximum dynamic lateral force vs. amplitude of base motion (Gravity wall, H=5m)

5.2 Cantilever wall

In this section, dynamic response of gravity wall-soil systems subjected to dynamic loading at the base has been investigated in Section 5.1. In this section, the dynamic behaviour of a typical cantilever retaining wall having the same height and soil conditions is studied.

5.2.1 The model and the parameters

The typical geometry of the model and the finite element mesh used for cantilever wall-soil systems have been given in Figures 4.2.1.1 and 4.2.1.2 of the previous chapter. The wall rests on a foundation soil layer underlain by a rigid base at which the horizontal excitations are applied. The reader is referred to Section 4.2.1 for the detailed information about the model, boundary conditions and loading.

The foundation and backfill soil are assumed to consist of elastic-perfect plastic materials obeying Drucker-Prager yield criterion. The damping ratio of the system is taken as 5%.

Harmonic base motions having peak accelerations, $\alpha g = 0.1g, 0.3g, 0.5g$ and frequency ratios, $R_f = 0.2, 0.5, 2, 5$ are used (R_f has been defined by Equation 4.3).

The model dimensions and the parameters are presented in Table 5.2.1.1. As explained in Section 5.1.1, the wall dimensions are determined to satisfy the sliding and overturning resistance required by Mononobe-Okabe method. The peak base acceleration of base motion applied to the soil-wall system is used during the calculations with M-O method. The passive resistance of the soil in front of the wall is neglected in the assessment of the wall dimensions.

Table 5.2.1.1 Dimensions and material parameters considered in the typical cantilever wall analyses

Symbol	Description	Unit	Value
H	Height of the wall	m	5
D	Foundation layer thickness	m	5
T1	Wall dimensions	m	0.5
T2		m	0.5
B1	Wall dimensions for peak base acc. of 0.1 g	m	1
B2		m	1.5
B1	Wall dimensions for peak base acc. of 0.3 g	m	1
B2		m	3
B1	Wall dimensions for peak base acc. of 0.5 g	m	1.5
B2		m	5
ρ_s	Density of soil	t/m ³	1.8
E_s	Elasticity mod. of soil	kPa	80 000
ν_s	Poisson's ratio of soil	-	0.33
V_s	Shear wave velocity of soil	m/s	129
c	Drucker-Prager parameters (For E-P analysis)	kPa	0
ϕ		degree	33
ρ_w	Density of the wall	t/m ³	2.4
E_w	Elasticity mod. of the wall	kPa	25 x 10 ⁶
ν_w	Poisson's ratio of the wall	-	0.2

5.2.2 The results and comparisons

Figures 5.2.2.1 and 5.2.2.2 show the deformed mesh at different times. The displacements are magnified by 100 times in the figures. It may be said that the main mode of response consists of the deflection of the stem of the wall during dynamic loading.

The Drucker-Prager parameters are assumed to be $c=0$ and $\phi=33$ as given in Table 5.2.1.1. However, for base motions with greater acceleration amplitudes, due to the large accelerations and complex contact behaviour, convergence difficulties are encountered and the cohesion value is increased up to 30 kPa for some of the soil elements especially in the vicinity of the wall base as indicated by “x” marks in Figure 5.2.2.1 to achieve convergence.

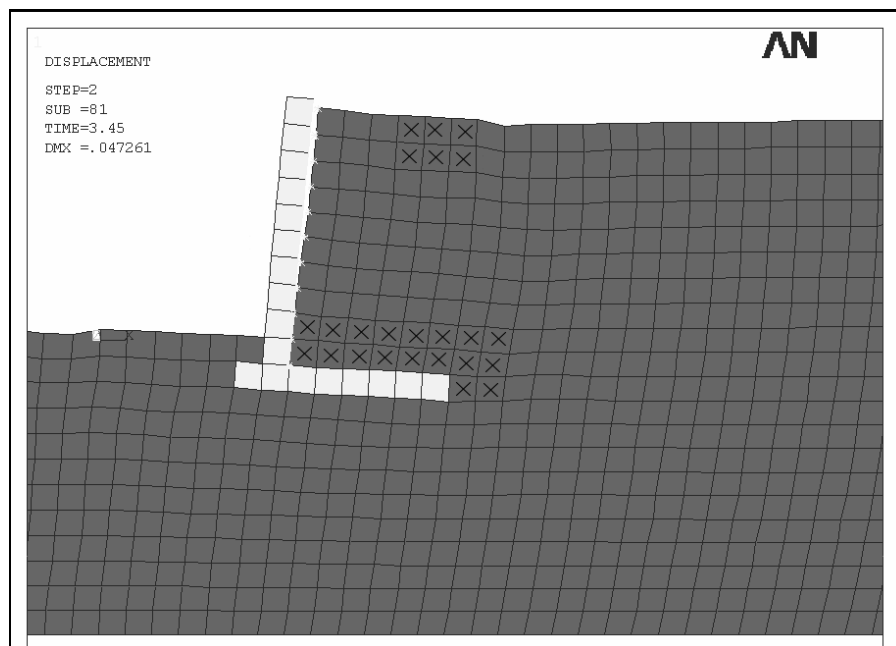


Figure 5.2.2.1 Deformed mesh for the cantilever wall
($H=5\text{m}$, $\alpha=0.3$, $R_f=0.5$, $t=3.45\text{ s.}$)

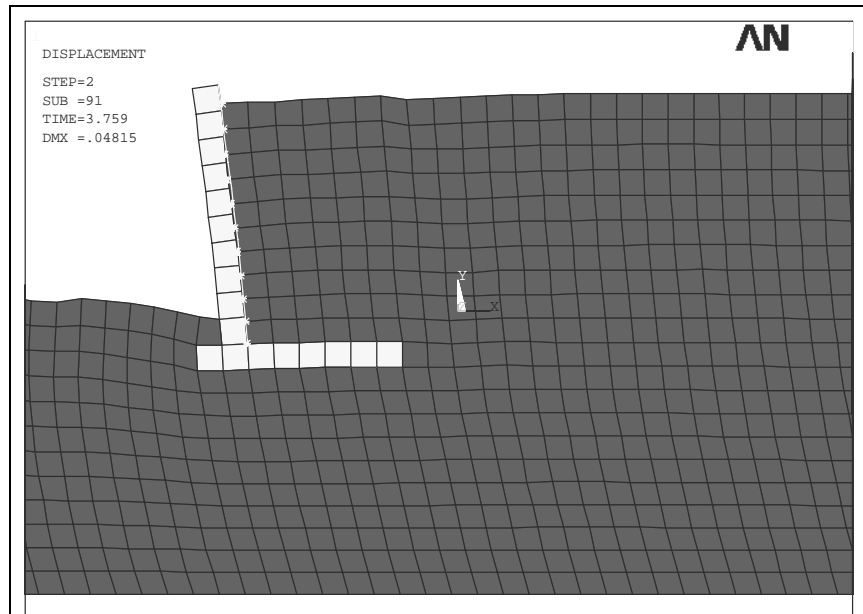


Figure 5.2.2.2 Deformed mesh for the cantilever wall
($H=5\text{m}$, $\alpha=0.3$, $R_f=0.5$, $t=3.759\text{ s.}$)

Maximum total lateral thrust vs. base motion amplitude is plotted in Figure 5.2.2.3. Similar to the results of gravity wall analyses, the increase of the total lateral force with base motion amplitude is approximately linear. The results of finite element analyses approach to M-O solution for higher peak acceleration values of the base motion.

Figure 5.2.2.4 shows the location of the application point of the total lateral thrust. The finite element analyses give lower application points as compared to M-O and Seed and Whitman methods as can be seen from the figure.

Maximum total base moment vs. base motion amplitude is presented in Figure 5.2.2.5. Although the total thrust values are greater as obtained by finite element analyses, due to the smaller moment arm, base moments are generally in good agreement with M-O method.

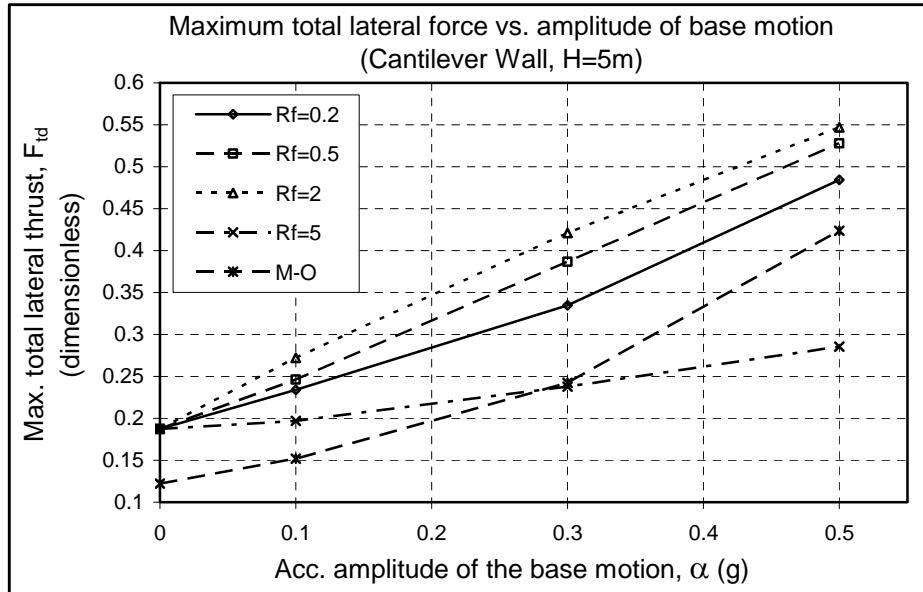


Figure 5.2.2.3 Maximum total lateral force vs. amplitude of the base motion (Cantilever wall, H=5m)

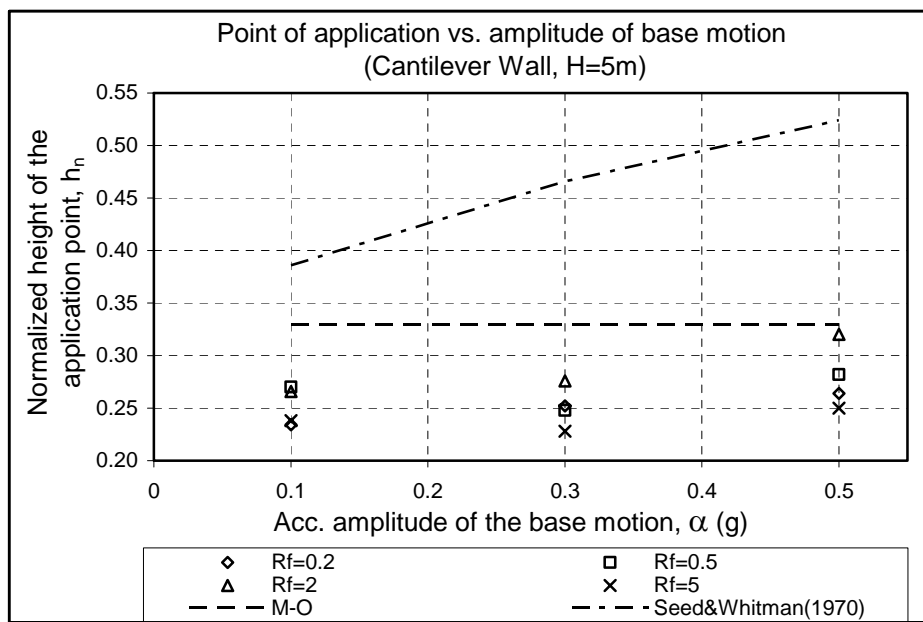


Figure 5.2.2.4 Height of the point of application of the total lateral force vs. amplitude of the base motion (Cantilever wall, H=5m)

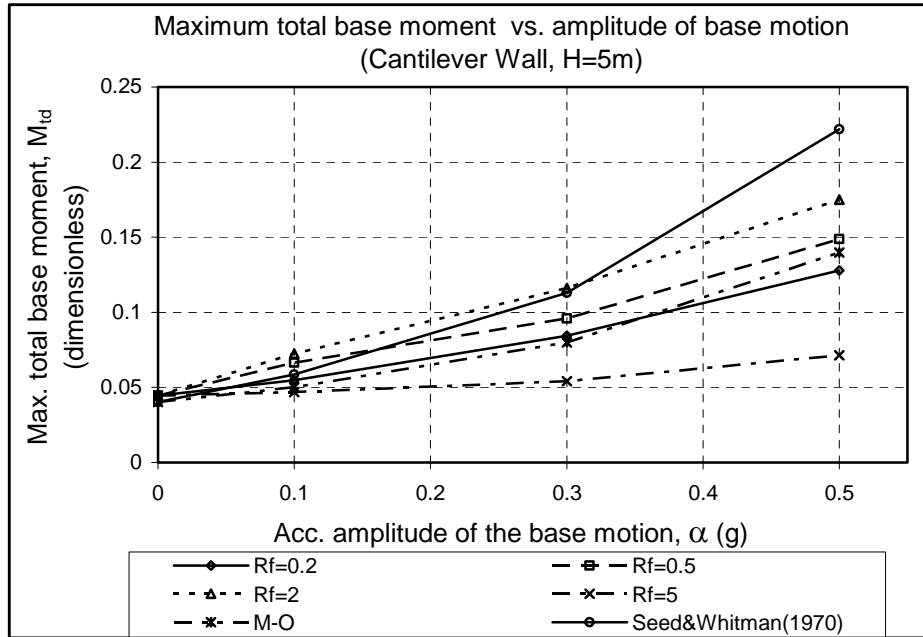


Figure 5.2.2.5 Maximum total base moment vs. amplitude of the base motion (Cantilever wall, H=5m)

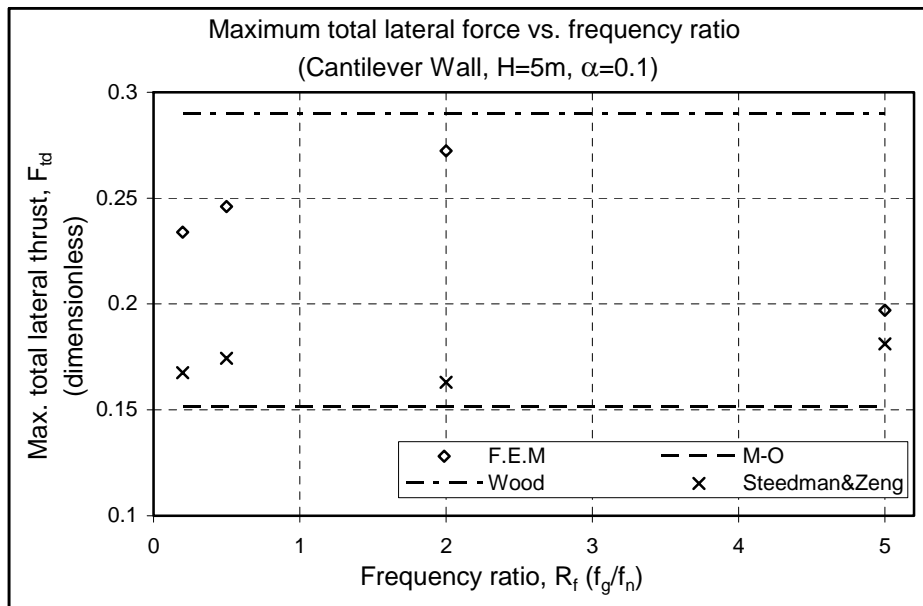


Figure 5.2.2.6 Maximum total lateral force vs. frequency ratio (Cantilever wall, H=5m, $\alpha = 0.1$)

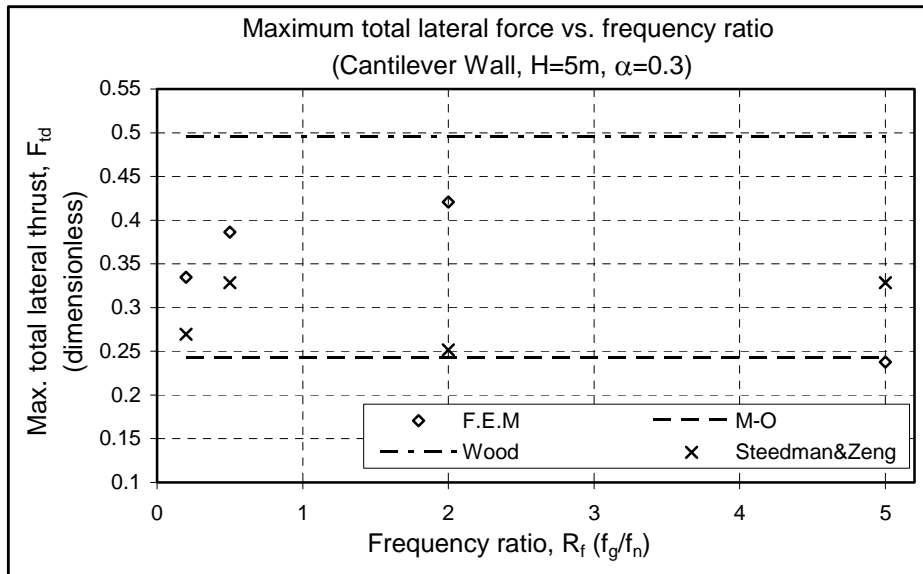


Figure 5.2.2.7 Maximum total lateral force vs. frequency ratio
(Cantilever wall, H=5m, $\alpha = 0.3$)

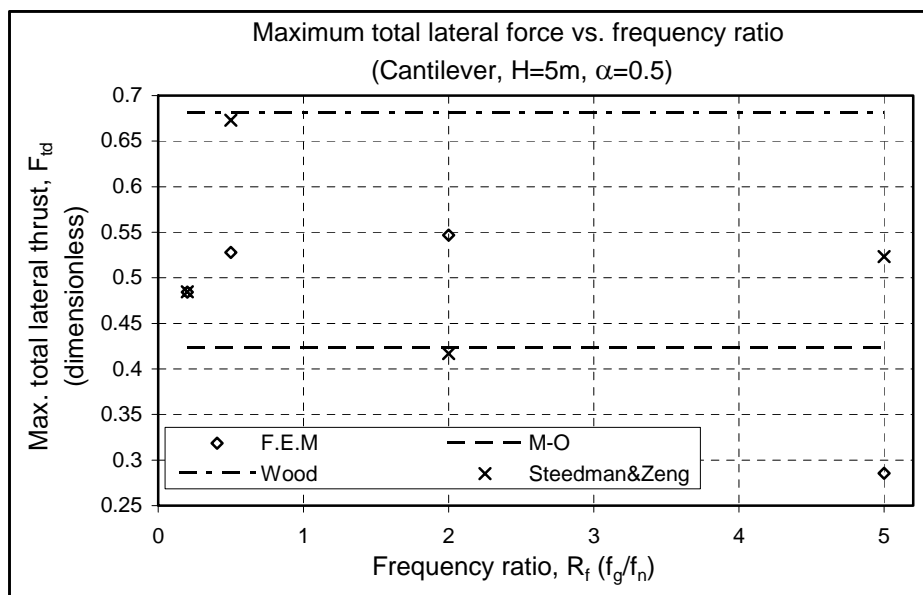


Figure 5.2.2.8 Maximum total lateral force vs. frequency ratio
(Cantilever wall, H=5m, $\alpha = 0.5$)

The variation of the maximum total thrust with frequency ratio is depicted in Figures 5.2.2.6 to 5.2.2.9 for different peak accelerations. It can be seen that the total lateral thrust is significantly affected by the frequency ratio and generally lies between the results of M-O and Wood solutions.

The result of the finite element analyses are summarized in Tables 5.2.2.1 and 5.2.2.2. The non-dimensional parameters in the tables, F_{td} , h_n , M_{td} and F_{dd} are defined by Equations 4.5, 4.6, 4.7 and 4.9 respectively in Section 4.1.2 and presented in the tables.

Table 5.2.2.1 Summary of the results for cantilever wall

Acc. amplitude of base motion (g)	Freq. ratio (R_f)	Total lat. force, F_t (kN)	Total base moment, M_t (kNm)	Height of application point, h	Non-dimensional total lat. force, F_{td}	Non-dimensional total base moment, M_{td}	Normalized height of app. point, h_n
0.1	0.2	103	121	1.17	0.234	0.055	0.23
0.1	0.5	109	147	1.35	0.246	0.066	0.27
0.1	2	120	160	1.33	0.272	0.072	0.27
0.1	5	87	104	1.19	0.197	0.047	0.24
0.3	0.2	148	186	1.26	0.335	0.084	0.25
0.3	0.5	171	212	1.24	0.386	0.096	0.25
0.3	2	186	256	1.38	0.421	0.116	0.28
0.3	5	105	120	1.14	0.238	0.054	0.23
0.5	0.2	214	282	1.32	0.484	0.128	0.26
0.5	0.5	233	329	1.41	0.528	0.149	0.28
0.5	2	241	386	1.60	0.547	0.175	0.32
0.5	5	126	158	1.25	0.285	0.071	0.25
$F_{td} = F_t / (\gamma H^2)$			$M_{td} = M_t / (\gamma H^3)$		$h_n = h / H$		

Table 5.2.2.2 Maximum dynamic lateral force results for gravity wall

Acc. amplitude of base motion (g)	Freq. ratio (R_f)	Static lat. force, F_{sta} (kN)	Total lat. force, F_t (kN)	Dynamic lat. force, F_d (kN)	Non-dimensional dynamic lat. force, F_{dd}
0.1	0.2	83	103	20	0.46
0.1	0.5	83	109	26	0.58
0.1	2	83	120	37	0.84
0.1	5	83	87	4	0.09
0.3	0.2	84	148	64	0.48
0.3	0.5	84	171	87	0.65
0.3	2	84	186	102	0.77
0.3	5	84	105	21	0.16
0.5	0.2	95	214	119	0.54
0.5	0.5	95	233	138	0.63
0.5	2	95	241	146	0.66
0.5	5	95	126	31	0.14
$F_{dd} = F_d / (\rho_s a_p \gamma H^2)$					

Maximum dynamic lateral thrust vs. amplitude of the base motion is shown in Figure 5.2.2.9. It can be seen that the difference between the finite element results and M-O solution decreases as the amplitude of the base motion increases in general.

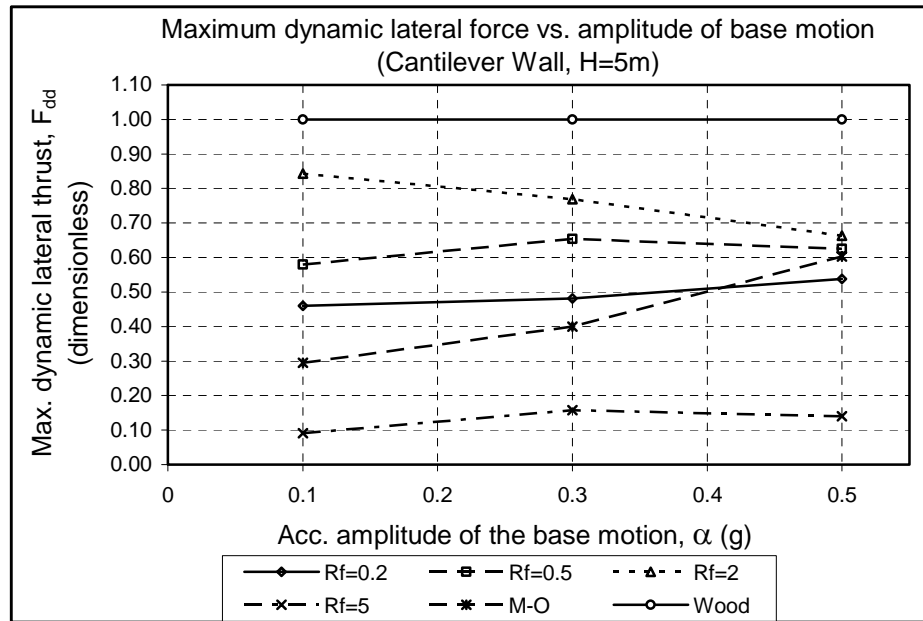


Figure 5.2.2.9 Maximum dynamic lateral force vs. amplitude of the base motion (Cantilever wall, H=5m)

5.3 Analyses with real earthquake records

The dynamic behaviour of soil-wall systems subjected to harmonic base motion has been presented in Sections 5.1 and 5.2. In this section, the results obtained by using real earthquake records with varying peak acceleration and frequency content are presented for identical soil-wall configurations.

Table 5.3.1 presents the earthquake motions used. EQ4 motion has been used in the analyses presented in Chapter 4.

Acceleration time histories and acceleration response spectra of the earthquake records are shown given Figures 5.3.1 and 5.3.2 respectively. During the finite

element analyses, a part of these records are used which contain the maximum acceleration, with a total duration of not less than 10 seconds, in order to decrease the long calculation time and very large output data.

EQ4, EQ5 and EQ6 motions with peak accelerations varying between 0.1g – 0.27g are used in the analysis of gravity wall-soil system. EQ4, EQ5, EQ6 and EQ7 motions are used in cantilever wall-soil models which have peak acceleration between 0.1g and 0.4g.

Table 5.3.1 Summary of the earthquake records

Ground motion	EQ4	EQ5	EQ6	EQ7
Earthquake name	Loma Prieta 1989	Landers 1992	Coalinga 1983	Imperial Valley 1979
Station	1002 Apeel 2 Redwood City	33083 Boron Fire Station	1608 Oil Fields Fire Station	942 El Centro Array #6
Peak acc. (g)	0.27	0.1	0.21	0.4
Peak spectral acc. (g)	1.18	0.43	0.74	1.23
f_p (1/s)	0.91	1.25	10.53	10
f_0 (1/s)	1.57	3.57	4.46	3.73
f_m (1/s)	0.99	1.59	2.7	1.1
f_p / f_n	0.30	0.41	3.43	3.26
f_0 / f_n	0.51	1.16	1.45	1.21
f_m / f_n	0.32	0.52	0.88	0.36

Table 5.3.2 Summary of the results for real earthquake motions
(Gravity wall, H=5m)

Peak acc. (g)	Ground motion	Total lat. force, F_t (kN)	Total base moment, M_t (kNm)	Height of application point, h	Non-dimensional total lat. force, F_{td}	Non-dimensional total base moment, M_{td}	Normalized height of app. point, h_n
0.1	EQ5	125	216	1.72	0.284	0.098	0.34
0.21	EQ6	152	258	1.70	0.343	0.117	0.34
0.27	EQ4	144	282	1.96	0.326	0.128	0.39

The finite element results of the total lateral thrust versus time are given in Figure 5.3.3 for the gravity wall, and in Figure 5.3.4 for the cantilever wall. The results are summarized in Tables 5.3.2 to 5.3.5.

Table 5.3.3 Dynamic lateral force results for real earthquake motions (Gravity wall, H=5m)

Peak acc. (g)	Ground motion	Static lat. force, F_{sta} (kN)	Total lat. force, F_t (kN)	Dynamic lat. force, F_d (kN)	Non-dimensional dynamic lat. force, F_{dd}
0.1	EQ5	74	125	51.3	1.16
0.21	EQ6	74	152	77.6	0.84
0.27	EQ4	76	144	68	0.57

Table 5.3.4 Summary of the results for real earthquake motions (Cantilever wall, H=5m)

Peak acc. (g)	Ground motion	Total lat. force, F_t (kN)	Total base moment, M_t (kNm)	Height of application point, h	Non-dimensional total lat. force, F_{td}	Non-dimensional total base moment, M_{td}	Normalized height of app. point, h_n
0.1	EQ5	126	175	1.39	0.285	0.079	0.28
0.21	EQ6	149	189	1.27	0.338	0.086	0.25
0.27	EQ4	150	192	1.28	0.339	0.087	0.26
0.4	EQ7	223	312	1.40	0.505	0.141	0.28

Table 5.3.5 Dynamic lateral force results for real earthquake motions (Cantilever wall, H=5m)

Peak acc. (g)	Ground motion	Static lat. force, F_{sta} (kN)	Total lat. force, F_t (kN)	Dynamic lat. force, F_d (kN)	Non-dimensional dynamic lat. force, F_{dd}
0.1	EQ5	83	126	43	0.97
0.21	EQ6	83	149	66	0.71
0.27	EQ4	84	150	66	0.55
0.4	EQ7	95	223	128	0.72

Comparison of the results of analyses using real earthquake records (summarized in Tables 5.3.1 to 5.3.5) and harmonic base motions (summarized in Tables 5.1.2.1, 5.1.2.2, 5.2.2.1 and 5.2.2.2) may lead to the following conclusions :

- The maximum total lateral thrusts and their application points obtained using real earthquake records close to those obtained by harmonic motions.

- Examining the results for the maximum total lateral thrust and its point of application, it can be observed that the results of all real EQ motions are in reasonably good agreement with those obtained by utilizing harmonic base motions with a frequency of f_0 of the earthquake. The lateral thrust and point of application calculated using EQ4 and EQ6 motions can also be assessed by using harmonic base motion with a frequency of f_m by reasonable accuracy.

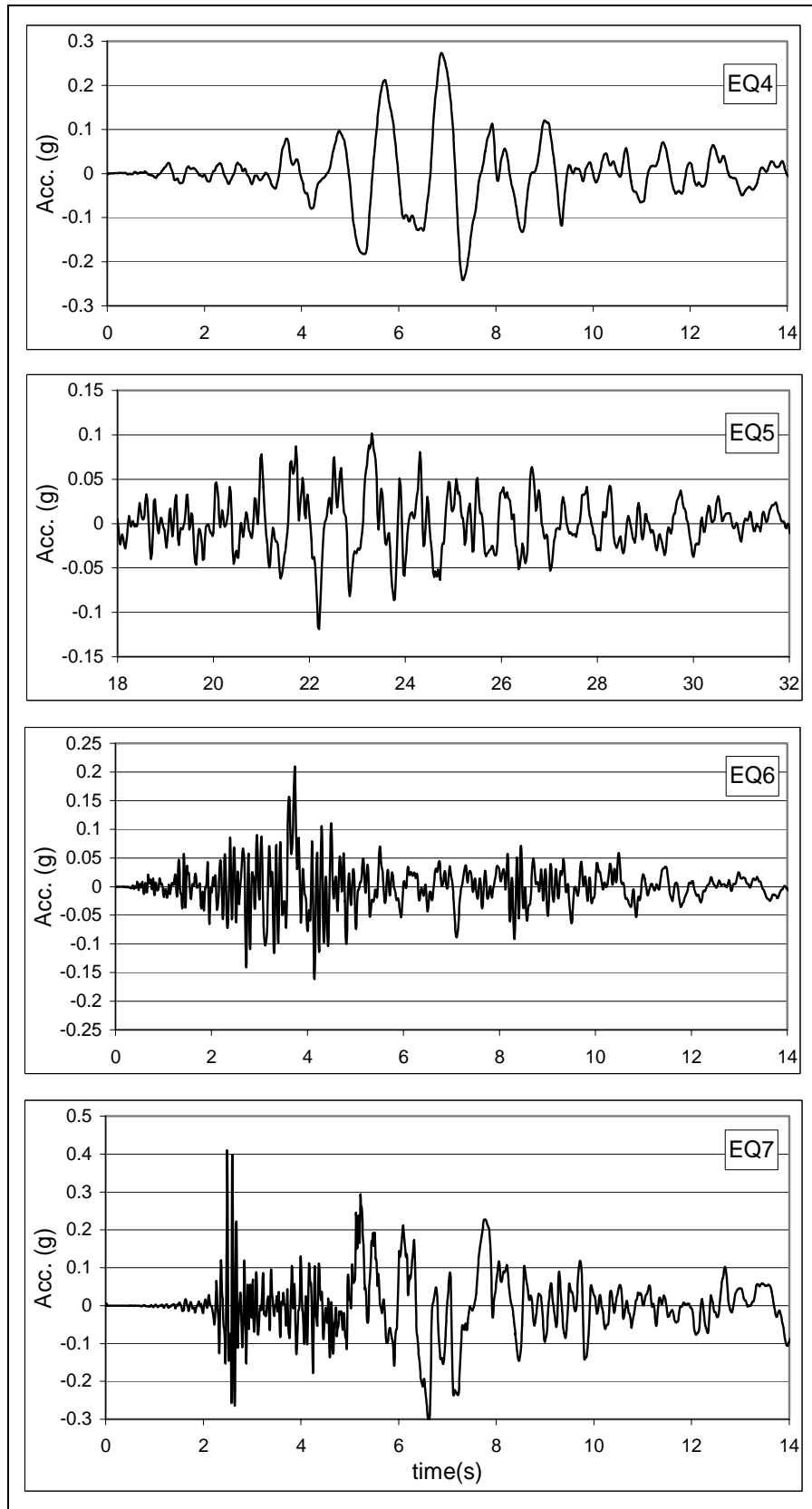


Figure 5.3.1 Acceleration time histories of the earthquake records used

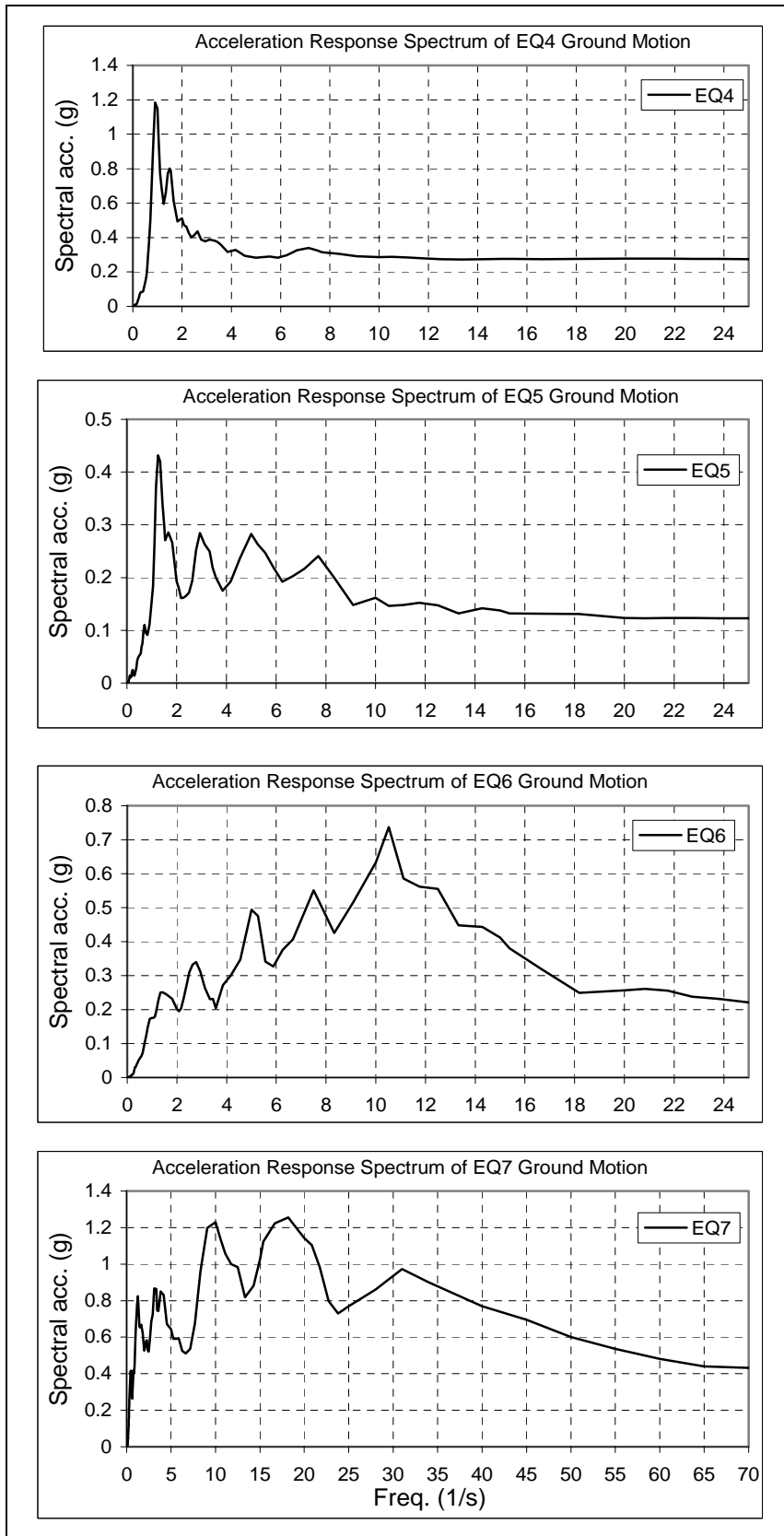


Figure 5.3.2 Acceleration response spectra of earthquake motions

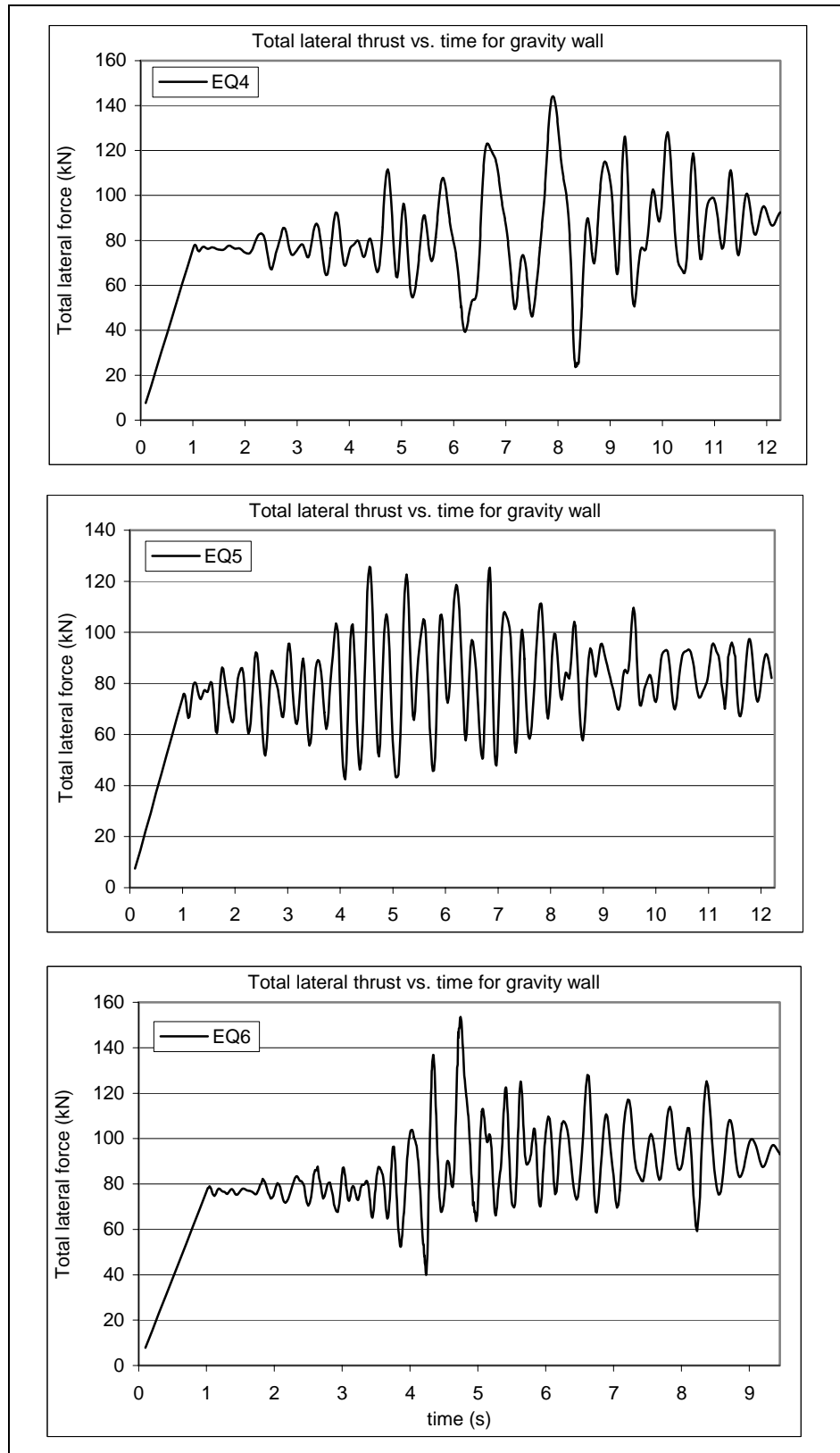


Figure 5.3.3 Total lateral force vs. time for real earthquake motions (Gravity wall, H=5m)

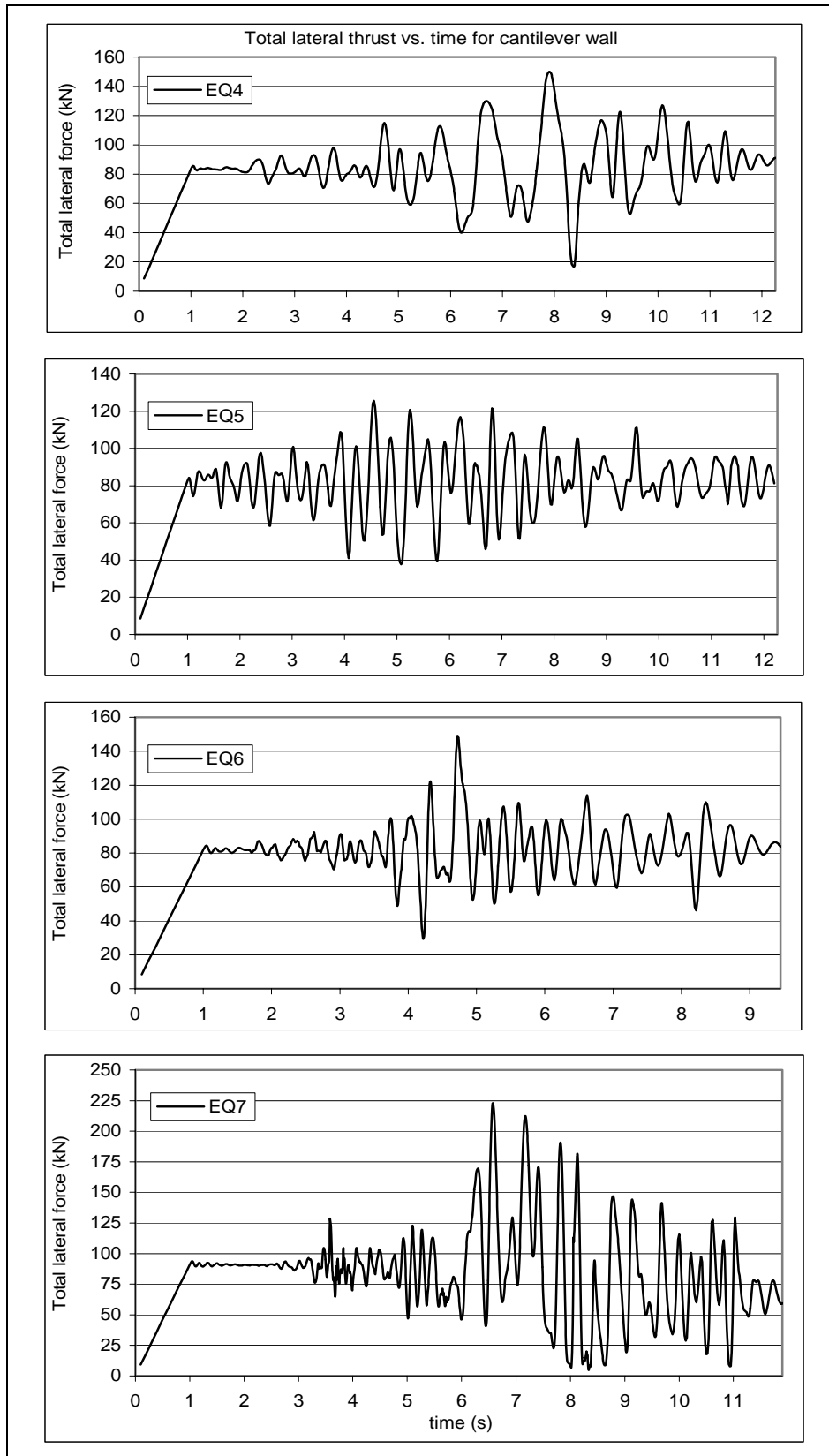


Figure 5.3.4 Total lateral force vs. time for real earthquake motions (Cantilever wall, H=5m)

5.4 On the effect of wall mass

In this section the effects of wall mass on the dynamic behaviour of soil-wall system and the dynamic lateral earth pressures acting on the wall are summarized.

In the finite element analyses carried out, mass of the wall is taken into account by assigning a density of 2.4 t/m^3 . Gravitational acceleration of 9.81 m/s^2 is applied to the mass to calculate the weight of the wall. In this way, effect of inertia of the wall is incorporated in the analyses.

In a second set of analyses, the mass of the wall is neglected in the calculations. Nevertheless, the weight of the wall is represented by a vertical force. So, the inertial forces induced by dynamic motion are neglected while the weight of the wall is considered in the analyses.

The results of two sets of analyses are summarized in Tables 5.4.1 and 5.4.2.

Table 5.4.1 Summary of the results for gravity wall

Acc. amplitude of base motion (g)	Freq. ratio (R_f)	Wall inertia	Total lat. force, F_t (kN)	Total base moment, M_t (kNm)	Height of application point, h	Peak outward rotation of the wall (rad.)	Normalized height of app. point, h_n
0.1	0.5	considered	98	165	1.69	0.000178	0.34
0.1	0.5	ignored	112	212	1.89	0.000078	0.38
0.3	0.5	considered	182	336	1.85	0.000600	0.37
0.3	0.5	ignored	231	494	2.14	0.000234	0.43
0.3	2	considered	184	350	1.90	0.000560	0.38
0.3	2	ignored	207	414	2.00	0.000023	0.40

Table 5.4.2 Summary of the results for cantilever wall

Acc. amplitude of base motion (g)	Freq. ratio (R_f)	Wall inertia	Total lat. force, Ft (kN)	Total base moment, Mt (kNm)	Height of application point, h	Normalized height of app. point, h_n
0.3	0.5	considered	170	211	1.24	0.25
0.3	0.5	ignored	195	252	1.29	0.26
0.3	2	considered	186	257	1.38	0.28
0.3	2	ignored	209	274	1.31	0.26

Figure 5.4.1 shows the the total lateral force variation with time found by using different harmonic base motions. It can be seen that the inertia of the wall significantly effects the dynamic lateral earth pressures where larger dynamic lateral forces act on the wall when the mass of the wall is neglected. Figure 5.4.2 shows the rotation of the wall vs. time plots. For gravity walls, it can be sen that when the inertia of the wall is neglected, rotation of the wall is significantly smaller as compared to the wall rotation when wall inertia is not neglected. On the other hand, lateral thrust acting on the wall gets smaller in case of wall inertia is taken into account.

Examining Table 5.4.2 and Figures 5.4.3 and 5.4.4 where the results of cantilever wall analyses are given, it is seen that the mass of the wall does not significantly affect the seismic lateral earth pressures or the deformations for cantilever walls.

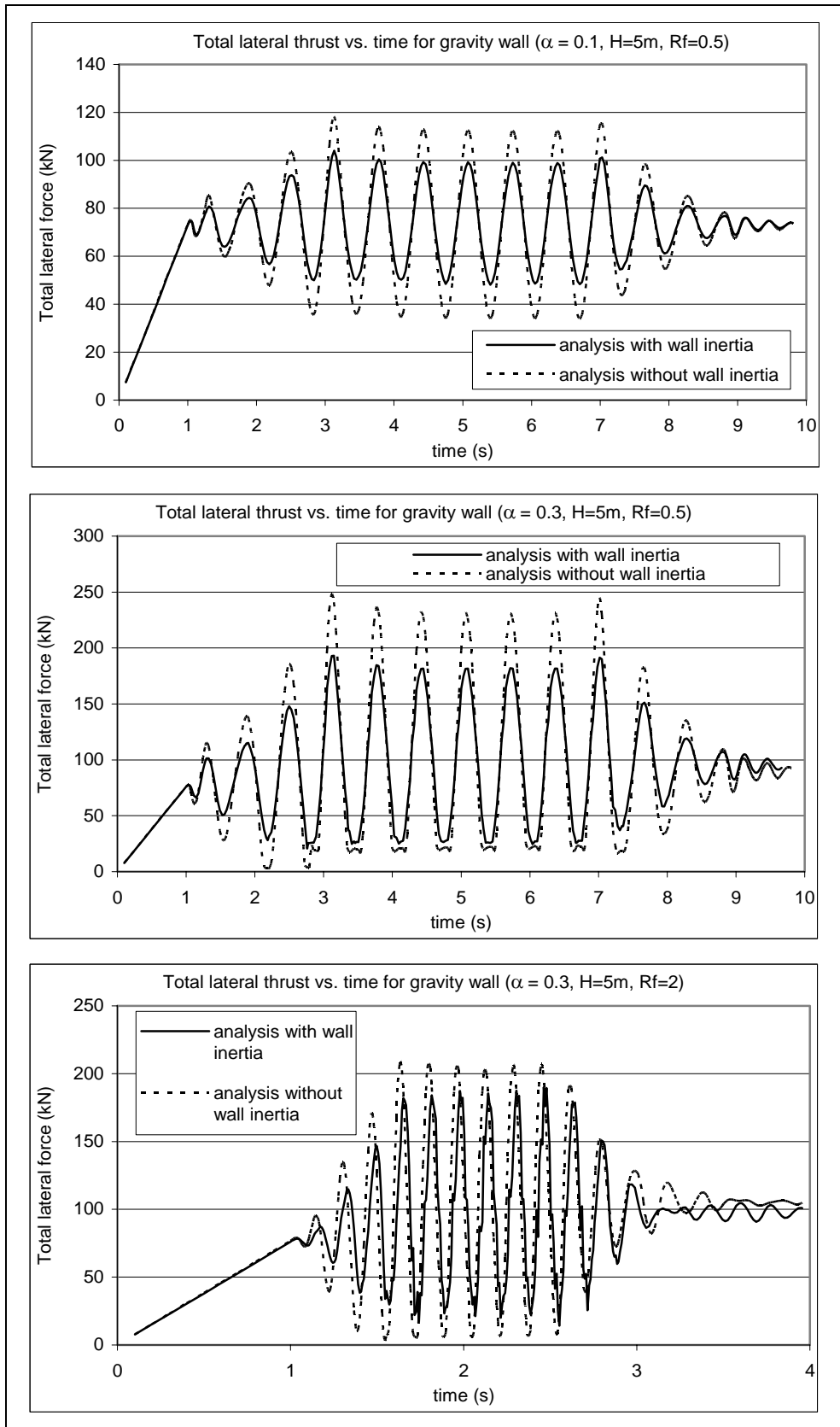


Figure 5.4.1 Total lateral thrust variation with time for gravity wall

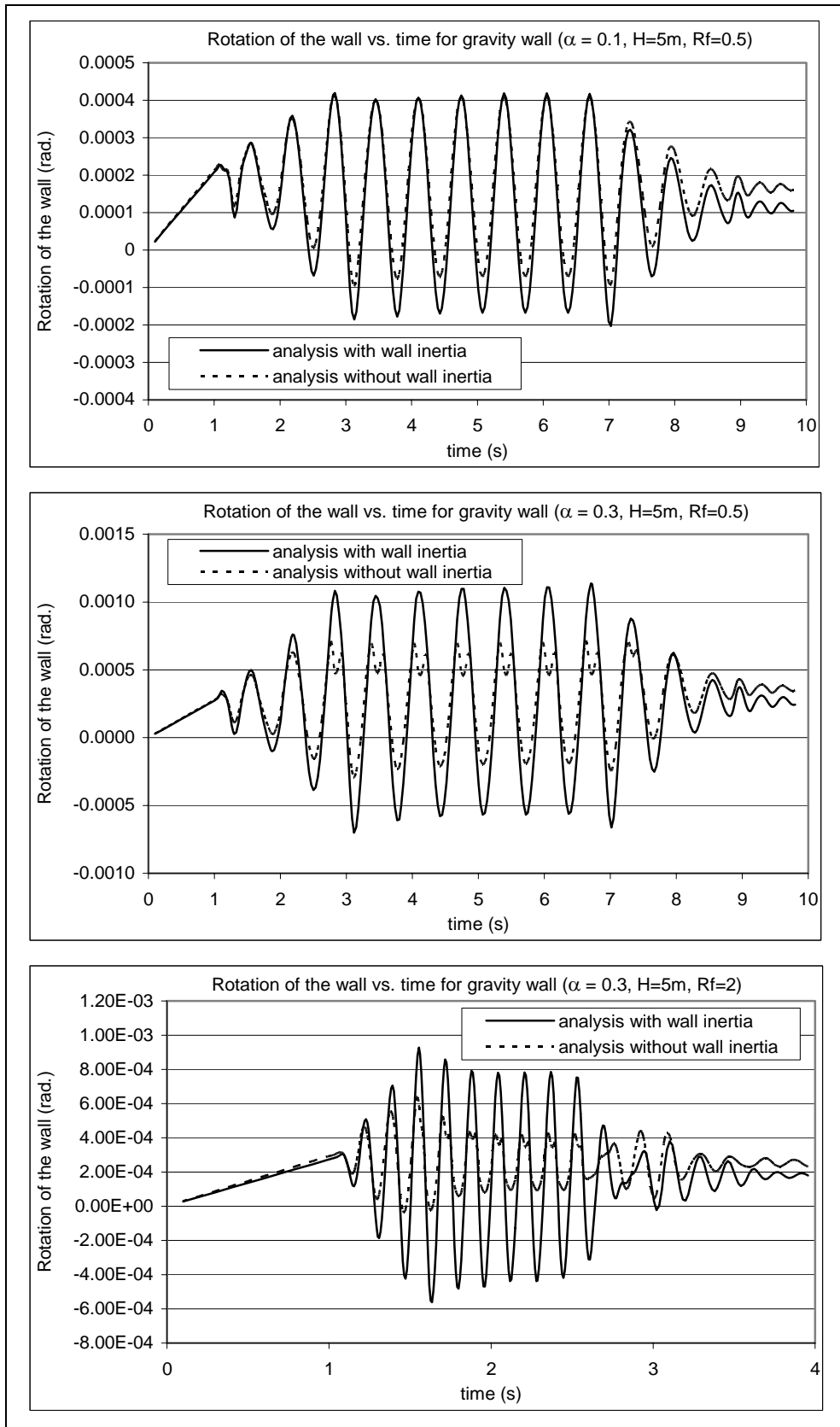


Figure 5.4.2 Rotation of the wall vs. time for gravity wall

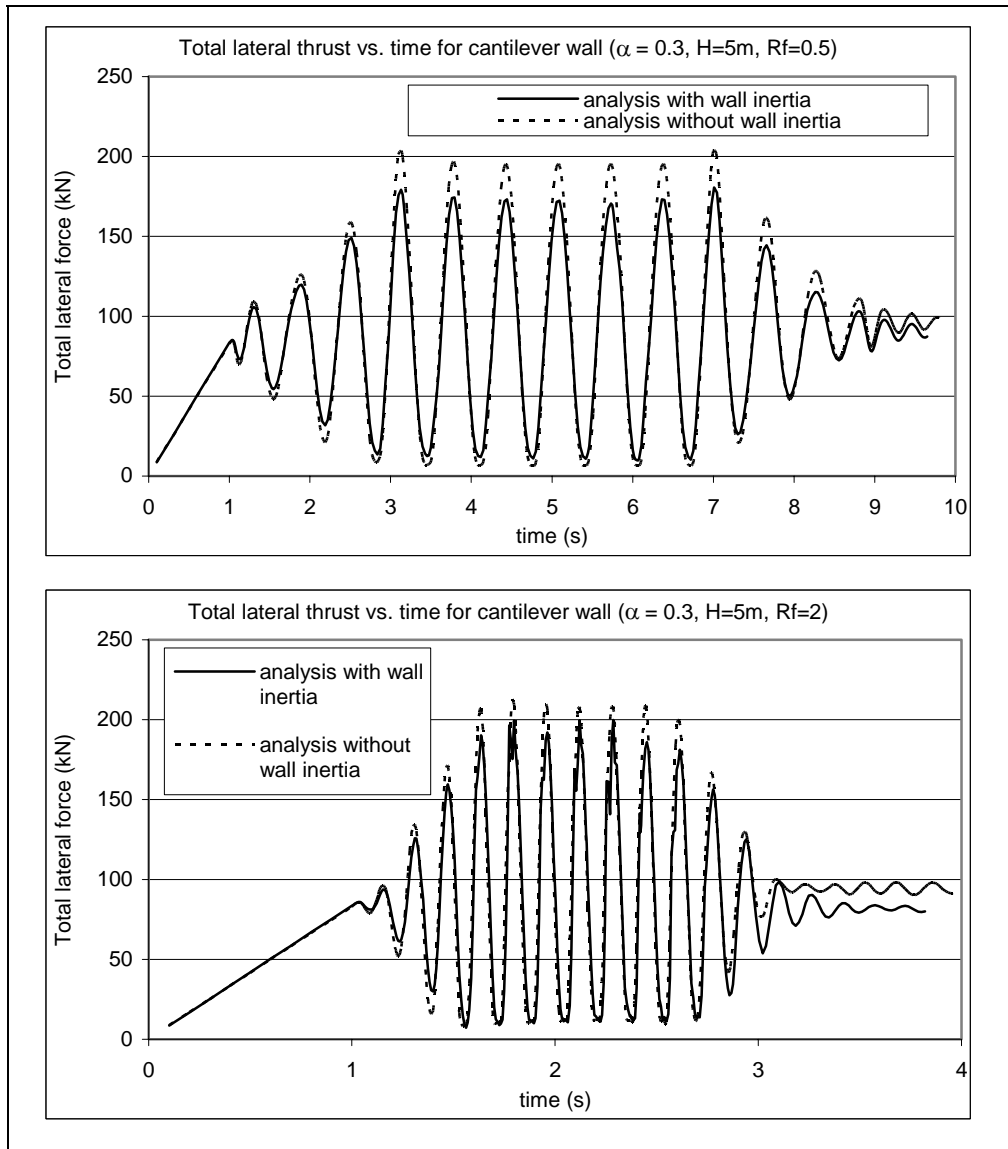


Figure 5.4.3 Total lateral thrust variation with time for cantilever wall

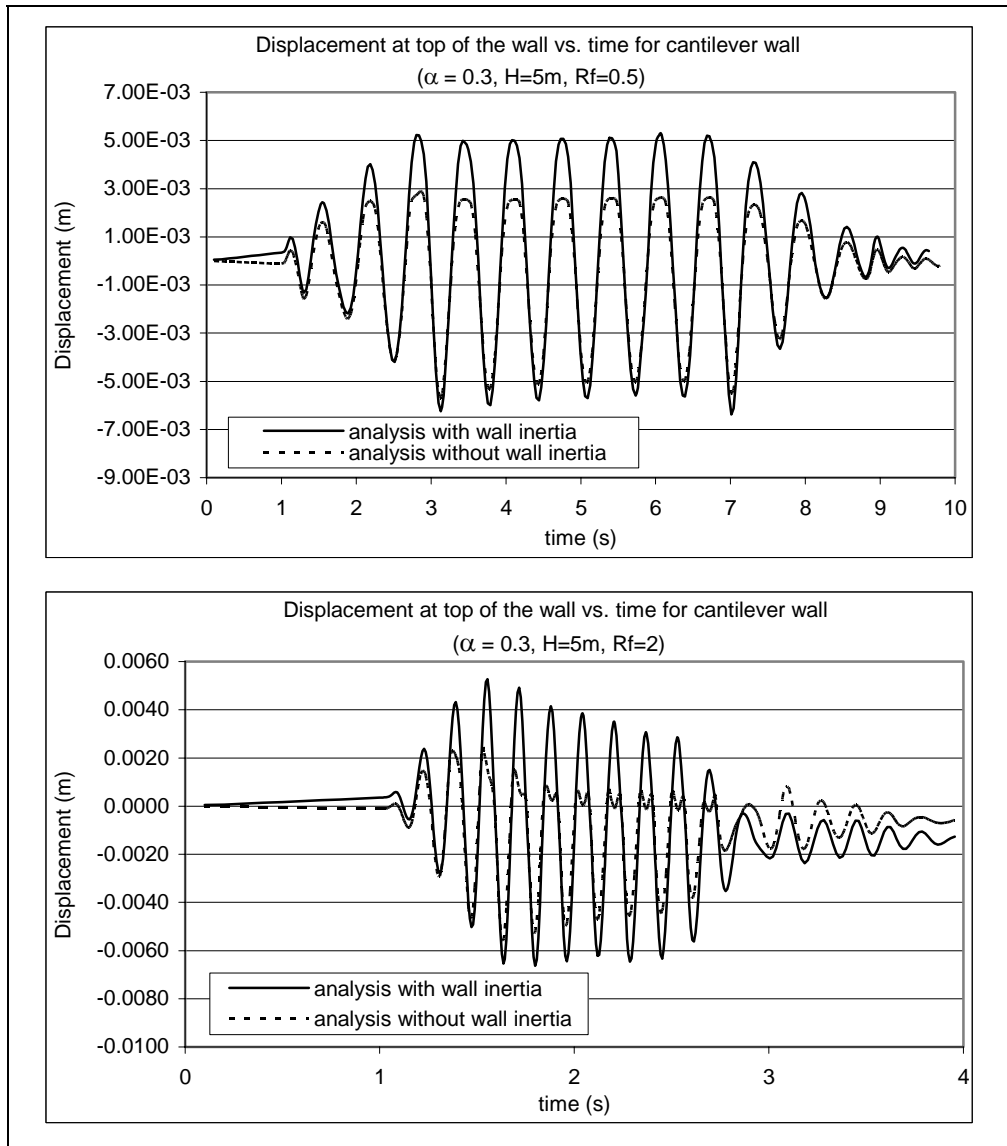


Figure 5.4.4 Displacement at the top of the wall vs. time for cantilever wall

CHAPTER 6

COMPARISON WITH EXPERIMENTAL STUDIES

In Chapters 4 and 5, results of analyses made for soil-wall systems subjected to base motions and the maximum dynamic lateral forces and application points of these forces are given. The obtained results are compared with commonly used design methods.

In this chapter, a comparison of finite element analyses results with the experimental findings is presented.

6.1 Gravity wall

Shake table tests conducted by Ichihara & Matsuzawa (1973), Sherif et al (1982) and Ishibashi & Fang (1987) are of most important studies about the dynamic response of rigid, displacing retaining walls. Sherif et al (1982) considered rigid walls making translational movement (denoted by T in Figures 6.1.1 and 6.1.2), Ishibashi & Fang (1987) considered rigid walls rotating about base only (denoted by RB in Figures 6.1.1 and 6.1.2) and Ichihara & Matsuzawa (1973) conducted experiments on rigid walls making both translational and rotational movement (denoted by RB+T in Figures 6.1.1 and 6.1.2).

Dry sand is used as backfill material in the aforementioned studies. The frequency of the harmonic base motion is 3.3 Hz in the experiments by Ichihara & Matsuzawa, and 3.5 Hz in the other two studies.

Information about the fundamental period of the soil-wall systems is not given in the papers. However, considering the small heights of the model walls (0.75m and 1m) and soil conditions, it can be stated that the base motion frequencies are considerably smaller than the fundamental frequencies of the models.

As discussed in Chapter 4 and 5, the results of finite element analyses carried out indicate that the dynamic lateral forces are significantly affected by the frequency of the base motion. Since the base motion frequencies of experiments are smaller than the fundamental frequencies of the models, finite element results for low frequency ratio ($R_f=0.2$) are considered for comparison of the lateral thrusts.

Figure 6.1.1 shows experimental values of the maximum total lateral thrusts reported and those obtained by numerical analyses. It can be seen that the finite element results are considerably higher than the experimental ones. Recalling that the movement of the wall is controlled independently from the forces acting on the wall during the experiments, it is probable that this may result in smaller lateral soil pressures. As a matter of fact, it is shown in Section 5.4 that the movements caused by the inertial effect of the wall result in a considerable decrease on the lateral pressures acting on the wall.

Location of application point found by finite element approach and experiments are given together in Figure 6.1.2. It can be seen that pure translational (T) and pure rotational (RB) modes of movement give the lower and upper boundaries respectively as found by experimental work. The results of both translational and rotational movement (RB+T) are generally between those of T and RB modes.

In the finite element models, the wall is allowed to make both translational and rotational displacements as mentioned before. It can be observed from the same figure that the finite element method yields point of application between those corresponding to pure translational and pure rotational wall movements, and generally agreeable with the experimental results of both translational and rotational movement.

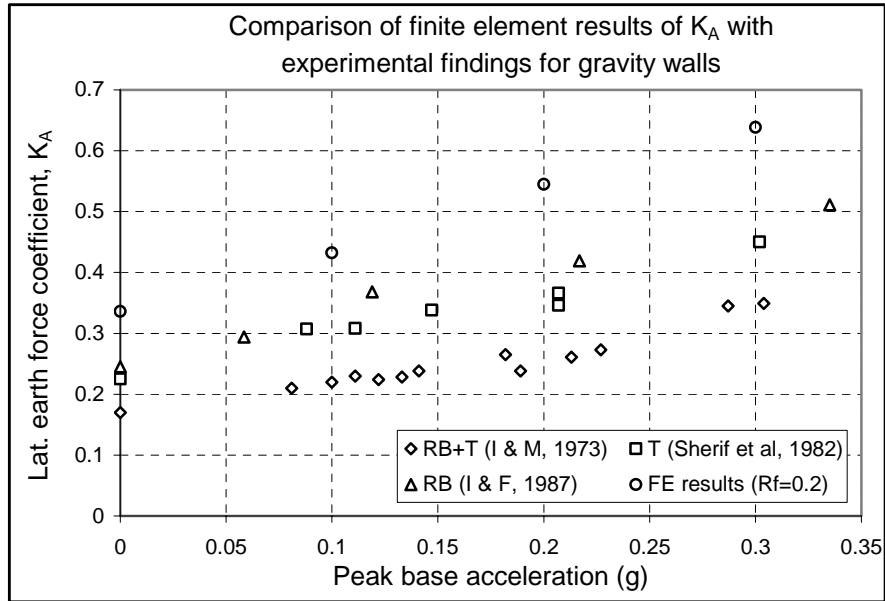


Figure 6.1.1 Comparison of the total lateral force coefficient (K_A) by experimental studies and numerical solution

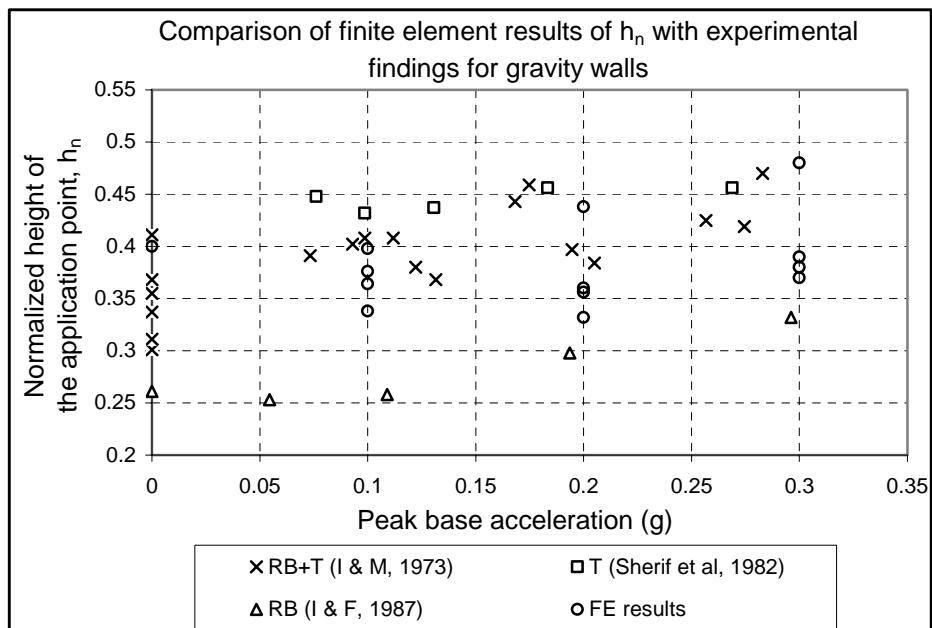


Figure 6.1.2 Comparison of the application point of the maximum total lateral force by experimental studies and numerical solution

6.2 Cantilever wall

Ortiz (1982) conducted centrifuge model tests to investigate the seismic behaviour of cantilever retaining walls. The lateral earth pressure distributions along the height of the wall for two of the tests with zero backfill slope and medium dense sand are reproduced in Figure 6.2.1

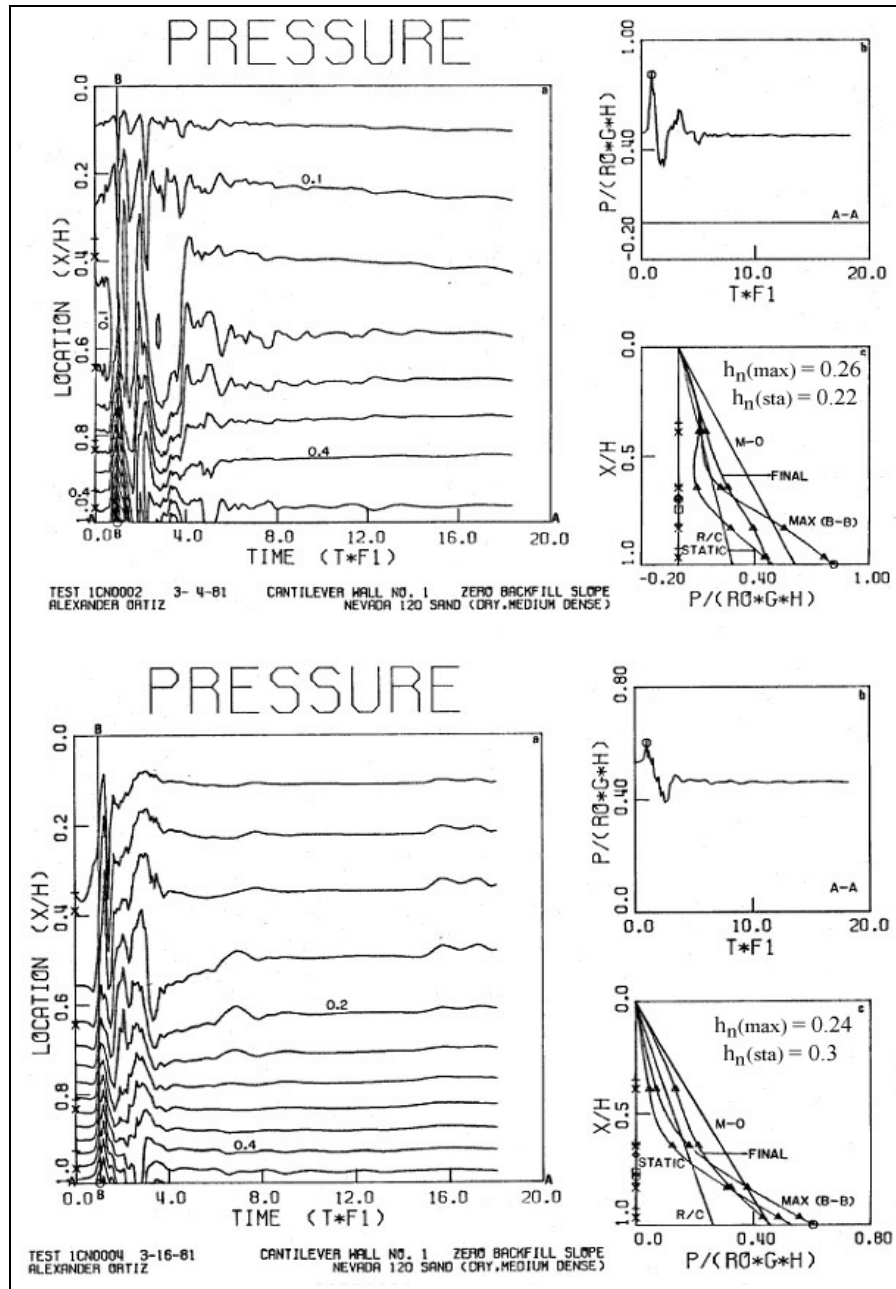


Figure 6.2.1 Earth pressure distributions on model cantilever walls by Ortiz (1982)

It can be seen from this figure that the maximum lateral pressure magnitudes are in good agreement with Mononobe-Okabe solution. However the pressure distribution is not linear as assumed by M-O method.

Finite element results of this study give the maximum lateral thrust values higher than the experimental results given by Ortiz which are similar to those calculated by Mononobe-Okabe method. Comparison of the total lateral thrusts calculated by finite element analyses and Mononobe-Okabe method has been presented in Figure 5.2.2.3.

On the other hand, as shown in Figure 6.2.2, experimental and finite element results for the location of application point of the maximum lateral thrust are almost similar.

Similar to the results for gravity walls, although the magnitude of the total lateral thrust is higher in the finite element analyses, the location of the application point is in good agreement with the experimental findings for the cantilever walls.

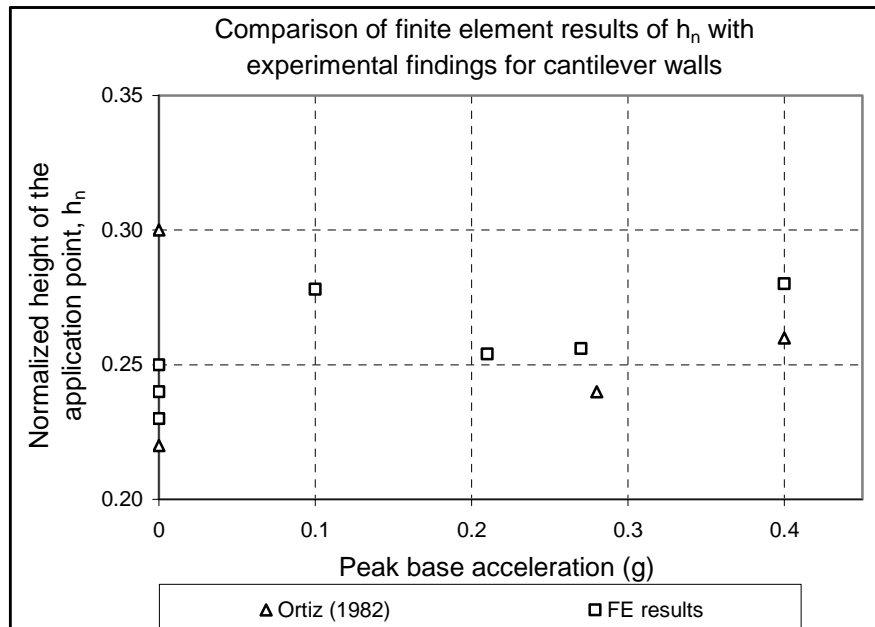


Figure 6.2.2 Comparison of the application point of the maximum total lateral force by experimental studies and numerical solution

CHAPTER 7

CONCLUSIONS

The purpose of this study was to investigate the dynamic response of gravity and cantilever retaining walls and determine the magnitude and distribution of the seismic soil pressures acting on the walls.

A two dimensional finite element model was developed for the analyses wherein the soil and the wall are represented by plane strain elements. The backfill and the foundation soil were assumed as dry granular material. The nonlinear stress-strain relationship of soil and the relative movement (sliding and gap) between the wall and soil were taken into account.

Harmonic motions and real earthquake records with different amplitude and frequency content were used as base motions in the analyses. Since the deformation mode of the wall is of concern in the dynamic behaviour of the wall, the wall is modelled to rest on a soil layer allowing both translational and rotational displacements.

On the basis of the analyses results, the following conclusions can be made:

- 1- In soil-wall systems subjected to harmonic base motions, the frequency of the motion has a significant effect on the dynamic response of the wall. The maximum dynamic lateral force on the wall considerably increases as the frequency of the base motion approaches the natural vibration frequency of the soil layer. However, the variation of the dynamic lateral force can not be related directly to the amplification in the soil due to the fact that smaller total thrust

values are obtained for high frequency motions corresponding to greater amplification ratios. The results indicate that relatively small dynamic forces act on the wall when high frequency base excitations are applied.

- 2- For harmonic base motions, the effect of the frequency ratio (defined as the ratio of the base motion to the fundamental frequency of the soil layer) on the lateral pressure distribution hence the location of the application point of the maximum total dynamic thrust is relatively small.
- 3- The finite element method yields higher static lateral forces than Coulomb's Earth Pressure Theory. This contributes to the difference between the maximum total (static + dynamic) lateral forces between the numerical results and Mononobe-Okabe method.
- 4- The maximum dynamic forces are generally between those suggested by Mononobe-Okabe and Wood (1973) solutions depending on the frequency ratio. Considerably smaller lateral forces than Mononobe-Okabe method are obtained for high frequency motions while higher forces than Wood solution are found for resonance case.
- 5- For gravity walls, location of the application point of the maximum total lateral thrust is found to be slightly higher than Mononobe-Okabe method when high frequency motions which result in significantly smaller lateral forces are neglected. The distance of the application point to the base of the wall varies between $0.33H$ and $0.39H$ which is well below the distance as suggested by Wood (1973) and Seed and Whitman (1970). Good agreement is obtained with the results of experimental studies for dynamic earth pressures acting on rigid, displacing walls.
- 6- Similar to the results for gravity walls, the location of the application point of the maximum total lateral force is in good agreement with experimental results for cantilever walls.

- 7- For real earthquake motions, the maximum lateral thrust and its point of application are found to be close to those obtained by harmonic base motions. In order to represent the real earthquake motion by a harmonic function, the frequency of the harmonic function can be chosen as the one closest to the fundamental frequency of the soil layer, among the frequencies f_p , f_0 and f_m where f_p is the predominant frequency, f_0 is the smoothed spectral predominant frequency and f_m is the mean frequency of the earthquake motion.
- 8- For gravity walls, tilting of the wall is found to be the dominant mode of deformation during dynamic loading. Sliding of the wall, on the other hand, is relatively small for the soil-wall models studied.
- 9- For cantilever retaining walls, deflection of the stem is the dominant mode of deformation during the dynamic loading. Rotation and sliding of the wall are relatively small for the soil-wall models examined.
- 10- It is observed that the inertia of the wall mass significantly affects the deformations and dynamic lateral earth pressures for gravity walls. The rotation and sliding of the wall is found to be mainly induced by the inertia of the wall mass. Considerably higher lateral pressures are obtained when the inertia of the wall is neglected. The inertial effects of the wall are found to be negligible for cantilever retaining walls.
- 11- No considerable permanent displacements or residual soil pressures are obtained in the analyses of the considered soil-wall systems, since the separation of the wall and foundation soil is not taken into account.

Recommendations for future work

In the conducted analyses, the damping of the system and the stiffness of the soil are taken constant. In the future, the variation in the damping and the stiffness of

the soil associated with strains may be considered and the effects on the dynamic response may be investigated.

The dynamic response of other types of retaining structures such as anchored or strutted retaining walls may be of concern in future studies.

The material model used to represent soil was an elastic-perfect plastic model without hardening. It is suggested to use a soil model which considers the shear and volumetric hardening in order to reach more realistic results as far as the displacements are concerned in the future.

REFERENCES

1. Al-Homoud, A. S., Whitman, R. V., “Seismic Analysis and Design of Rigid Bridge Abutments Considering Rotation and Sliding Incorporating Non-linear Soil Behaviour”, *Soil Dynamics and Earthquake Engineering*, 1999, pp. 247-277.
2. ANSYS ver. 8.0 Theory Reference, ANSYS Inc.
3. Bakeer, R. M., Bhatia, S. K., Ishibashi, I., “Dynamic Earth Pressure With Various Gravit Wall Movements”, *Design and Performance of Earth Retaining Structures*, ASCE, Geotechnical Special Public., 1990, No. 25, pp. 887-898.
4. Bathe, K. J., “Finite Element Procedures”, Prentice Hall, 1996.
5. Britto, A. M., Gunn, M.J., “Critical State Soil Mechanics Via Finite Elements”, Ellis Horwood, Chichester, 1987.
6. Clough, R. W., Penzien, J., “Dynamics of Structures”, McGraw-Hill, 1993.
7. Chen, W. F., Mizuno, E., “Nonlinear Analysis in Soil Mechanics”, Elsevier, Amsterdam, 1990.
8. Cook, R. D., Malkus, D. S., Plesha, M. E., “Concepts and Applications of Finite Element Analysis”, John Wiley, Third Edition, New York, 1989.
9. Çalışan, O., “A Model Study on the Seismic Behaviour of Gravity Retaining Walls”, Ph. D. Thesis, Middle East Technical University, Ankara, Turkey, January 1999.
10. Das, B. M., Puri, V. K., “Static and Dynamic Active Earth Pressure”, *Technical Note, Geotechnical and Geological Engineering*, 1996, 14, pp. 353-366.

11. Dimarogona, P. D., "Distribution of Lateral Earthquake Pressure on a Retaining Wall", *Soils and Foundations*, Japanese Society of Soil Mechanics and Foundation Engineering, 1983, 23(4), pp. 1-10.
12. FLAC ver. 4.0 User Manual, Itasca Inc.
13. Fukuoka, M., Imamura, Y., "Researches on Retaining Walls During Earthquakes", *Proceedings of the Eighth World Conference on Earthquake Engineering*, San Francisco, 1984, pp. 509-515.
14. Gazetas, G., Psarropoulos, P. N., Anastasopoulos, I., Gerolymos, N., "Seismic Behaviour of Flexible Retaining Systems Subjected to Short-duration Moderately-strong Excitation", *Soil Dynamics and Earthquake Engineering*, 2004, 24, pp. 537-550.
15. Ichihara, M., Matsuzawa, H., "Earth Pressure During Earthquake", *Soils and Foundations*, Japanese Society of Soil Mechanics and Foundation Engineering, 1973, 13(4), pp. 75-86.
16. Idriss, I. M., Sun, J. I., "SHAKE91: A Computer Program for Conducting Equivalent Linear Seismic Response Analyses of Horizontally Layered Deposits", University of California, Davis, 1992.
17. Ishibashi, I., Fang, Y. S., "Dynamic Earth Pressures with Different Wall Movement Modes", *Soils and Foundations*, Japanese Society of Soil Mechanics and Foundation Engineering, 1987, 27(4), pp. 11-22.
18. Kramer, S., "Geotechnical Earthquake Engineering", Prentice Hall, 1996.
19. Lysmer, J., Kuhlemeyer, R. L., "Finite Dynamic Model for Infinite Media", *Journal of Engineering Mechanics Division*, ASCE, 1969, 95, pp. 859-877.
20. Madabhushi, S. P. G., Zeng, X. "Seismic Response of Gravity Quay Walls II: Numerical Modeling", *Journal of Geotech. And Geoenvironmental Engineering*, ASCE, 1998, 124, pp. 418-427.

21. Matsuo, H., Ohara, S., "Lateral Earth Pressure and Stability of Quay Walls During Earthquakes", Proceedings of Second World Conference on Earthquake Engineering, Tokyo, Japan, 1960, Vol. 2, pp. 165-181.
22. Mononobe, N., "Earthquake-Proof Construction of Masonry Dams", Proceedings, World Engineering Conference, 1929, Vol. 9, page 176.
23. Mononobe, N., Matsuo, H., "On the Determination of Earth Pressures During Earthquakes", Proceedings, World Engineering Conference, 1929, Vol. 9, page 275.
24. Nadim, F., Whitman, R. V., "Seismically Induced Movement of Retaining Walls", Journal of Geotechnical Engineering, ASCE, 1983, 109(7), pp. 915-931.
25. Nadim, F., Whitman, R. V., "Coupled Sliding and Tilting of Gravity Walls During Earthquakes", Proceedings of the Eighth World Conference on Earthquake Engineering, San Francisco, 1984, pp. 477-484.
26. Nazarian, H. N., Hadjian, A. H., "Earthquake-induced Lateral Soil Pressures on Structures", Journal of the Geotechnical Engineering Division, ASCE, 1979, 105, pp. 1049-1066.
27. Newmark, N. M., "A Method of Computation for Structural Dynamics", ASCE Journal of Engineering Mechanics Division, 1959, Vol. 85, pp. 67-94.
28. Okabe, S., "General Theory of Earth Pressure", Journal, Japanese Society of Civil Engineers, 1926, Vol.12, No. 1.
29. Ortiz, L. A., "Dynamic Centrifuge Testing of Cantilever Retaining Walls", Ph. D. Thesis, California Institute of Technology, 1982.
30. Ortiz, L. A., Scott, R. F., Lee, J., "Dynamic Centrifuge Testing of a Cantilever Retaining Wall", Earthquake Engineering and Structural Dynamics, 1983, 11, pp. 251-268.

31. Ostadan, F., "Seismic Soil Pressure for Building Walls: An Updated Approach", *Soil Dynamics and Earthquake Engineering*, 2005, 25, pp. 785-793.
32. Prakash, S., Saran, S., "Static and Dynamic Earth Pressures Behind Retaining Walls", *Proceedings on the Third Symposium on Earthquake Engineering*, Roorkee, India, 1966, Vol. 1, pp. 277-288.
33. Psarropoulos, P. N., Klonaris, G., Gazetas, G., "Seismic Earth Pressures on Rigid and Flexible Retaining Walls", *Soil Dynamics and Earthquake Engineering*, 2005, 25, pp. 795-809.
34. Rathje, E. M., Abrahamson, N. A., Bray, J. D., "Simplified Frequency Content Estimates of Earthquake Ground Motions", *Journal of Geotechnical and Geoenvironmental Engineering*, ASCE, 1998, 124, pp.150-159.
35. Richards, R., Elms, D. G., "Seismic Behaviour of Gravity Retaining Walls", *Journal of Geotechnical Engineering Division*, ASCE, 1979, 105, pp. 449-464.
36. Richards, R. Jr., Huang, C., Fishman, K. L., "Seismic Earth Pressure on Retaining Structures", *Journal of Geotech. And Geoenv. Engineering*, 1999, 125(9), pp. 771-778.
37. Seed, H., B., Whitman, R., V., "Design of Earth Retaining Structures for Dynamic Loads", *Proceedings of the Speciality Conference on Lateral Stresses in the Ground and Design of Earth Retaining Structures*, ASCE, 1970, pp. 103-147.
38. Sherif, M. A., Ishibashi, I., Lee, C. D., "Earth Pressures Against Rigid Retaining Walls", *Journal of Geotechnical Engineering Division*, ASCE, 1982, 108(5), pp. 679-695.
39. Siddharthan, R., Maragakis, E. M., "Performance of Flexible Retaining Walls Supporting Dry Cohesionless Soils Under Cyclic Loads", *International Journal for Numerical and Analytical Methods in Geomechanics*, 1989, 13, pp. 309-326.

40. Sommers, S. A., Wolfe, W. E., "Earthquake Induced Responses of Model Retaining Walls", Proceedings of the Eighth World Conference on Earthquake Engineering, San Francisco, 1984, pp. 517-524.
41. Steedman, R. S., Zeng, X., "The Influence of Phase on the Calculation of Pseudo-static Earth Pressure on a Retaining Wall", Geotechnique, 1990, 40(1), pp. 103-112.
42. Veletsos, A. S., Younan, A. H., "Dynamic Soil Pressures on Rigid Vertical Walls", Earthquake Engineering and Structural Dynamics, 1994, 23, pp. 275-301.
43. Veletsos, A. S., Younan, A. H., "Dynamic Response of Cantilever Retaining Walls", Journal of Geotech. and Geoenv. Engineering, ASCE, 1997, 123, pp.161-172.
44. Whitman, R. V., Liao, S., "Seismic Design of Gravity Retaining Walls", Proceedings of the Eighth World Conference on Earthquake Engineering, San Francisco, 1984, pp. 533-540.
45. Wood, J. H., "Earthquake Induced Soil Pressures on Structures", report No. EERL 73-05, Earthquake Engineering Research Laboratory, California Institute of Technology, Pasadena, California, 1973.
46. Woodward, P. K., Griffiths, D. V., "Comparison of the Pseudo-Static and Dynamic Behaviour of Gravity Retaining Walls", Geotechnical and Geological Engineering, 1996, 14, pp. 269-290.
47. Wu, G., Finn, W. D. L., "Seismic Lateral Pressures for Design of Rigid Walls", Canadian Geotechnical Journal, 1999, 36, pp. 509-522.
48. Wu, Y., Prakash, S., "Prediction of Seismic Displacements of Rigid Retaining Wall", Proceedings of the Fifteenth International Conference on Soil Mechanics and Geotechnical Engineering, ICSMGE, İstanbul, 2001, Vol. 2, pp. 1281-1284.

49. Younan, A. H., Veletsos, A. S., “Dynamic Response of Flexible Retaining Walls”, *Earthquake Engineering and Structural Dynamics*, 2000, 29, pp. 1815-1844.
50. Yunatçı, A. A., “A Model Study on the Seismic Behaviour of Laterally Braced Sheet Pile Walls”, M. Sc. Thesis, Middle East Technical University, Ankara, Turkey, January 2003.
51. Zeng, X., “Seismic Response of Gravity Quay Walls I: Centrifuge Modeling”, *Journal of Geotech. And Geoenv. Engineering*, ASCE, 1998, 124(5), pp.406-417.
52. Zhang, J. M., Shamoto, Y., Tokimatsu, K., “Seismic Earth Pressure Theory For Retaining Walls Under Any Lateral Displacement”, *Soils and Foundations*, Japanese Geotechnical Society, 1998, 38(2), pp. 143-163.
53. Zienkiewicz, O. C., “The Finite Element Method”, McGraw-Hill, 1977.

CURRICULUM VITAE

Personal Information

Surname, Name : Yıldız, Ersan
Nationality : Turkish
Date, Place of Birth : 1 July 1979, Ankara
Marital Status : Single
E-mail : ersanyildiz@gmail.com, civil182@yahoo.com

Education

<u>Degree</u>	<u>Institution</u>	<u>Year of Graduate</u>
M.S.	METU, Civil Engineering	2003
B.S.	Gazi Univ. Civil Eng.	2001
High Sch.	Ankara Atatürk Anatolian High School	1997

Work Experience

<u>Year</u>	<u>Place</u>	<u>Enrollment</u>
2003-Present	Yüksel Domaniç Eng. Ltd.	Design Engineer

Foreign Languages

English